NASA TECHNICAL NOTE

NASA TN D-7800

NASA TN D-7800

# SHOCK SHAPES ON BLUNT BODIES IN HYPERSONIC-HYPERVELOCITY HELIUM, AIR, AND $CO_2$ FLOWS, AND CALIBRATION RESULTS IN LANGLEY 6-INCH EXPANSION TUBE

*Charles G. Miller III*

*Langley Research Center*
*Hampton, Va. 23665*



NATIONAL AERONAUTICS AND SPACE ADMINISTRATION • WASHINGTON, D. C. • FEBRUARY 1975

| 1. Report No. | 2. Government Accession No. | 3. Recipient's Catalog No. |
|---|---|---|
| NASA TN D-7800 | | |

| 4. Title and Subtitle | 5. Report Date |
|---|---|
| SHOCK SHAPES ON BLUNT BODIES IN HYPERSONIC-HYPERVELOCITY HELIUM, AIR, AND $CO_2$ FLOWS, AND CALIBRATION RESULTS IN LANGLEY 6-INCH EXPANSION TUBE | February 1975 |
| | 6. Performing Organization Code |
| 7. Author(s) | 8. Performing Organization Report No. |
| Charles G. Miller III | L-9775 |
| | 10. Work Unit No. |
| 9. Performing Organization Name and Address | 502-27-01-02 |
| NASA Langley Research Center<br>Hampton, Va. 23665 | 11. Contract or Grant No. |
| | 13. Type of Report and Period Covered |
| 12. Sponsoring Agency Name and Address | Technical Note |
| National Aeronautics and Space Administration<br>Washington, D.C. 20546 | 14. Sponsoring Agency Code |

15. Supplementary Notes

16. Abstract

This report presents shock shape results for flat-faced cylinders, spheres, and spherically blunted cones in various test gases, along with preliminary results from a calibration study performed in the Langley 6-inch expansion tube. Free-stream velocities from 5 to 7 km/sec are generated at hypersonic conditions with helium, air, and $CO_2$, resulting in normal shock density ratios from 4 to 19. Ideal-gas shock shape predictions, in which an effective ratio of specific heats is used as input, are compared with the measured results. The effect of model diameter is examined to provide insight to the thermochemical state of the flow in the shock layer. The regime for which equilibrium exists in the shock layer for the present air and $CO_2$ test conditions is defined. Test core flow quality, test repeatability, and comparison of measured and predicted expansion-tube flow quantities are discussed.

| 17. Key Words (Suggested by Author(s)) | 18. Distribution Statement |
|---|---|
| Expansion tube<br>Hypersonic<br>Hypervelocity<br>Shock shapes<br>Real gas | Unclassified – Unlimited<br><br>STAR Category 12 |

| 19. Security Classif. (of this report) | 20. Security Classif. (of this page) | 21. No. of Pages | 22. Price* |
|---|---|---|---|
| Unclassified | Unclassified | 86 | $4.75 |

*For sale by the National Technical Information Service, Springfield, Virginia 22151

# SHOCK SHAPES ON BLUNT BODIES IN HYPERSONIC-HYPERVELOCITY HELIUM, AIR, AND $CO_2$ FLOWS, AND CALIBRATION RESULTS IN LANGLEY 6-INCH EXPANSION TUBE

By Charles G. Miller III
Langley Research Center

## SUMMARY

This report presents shock shape results on flat-faced cylinders, spheres, and spherically blunted cones in various test gases, along with preliminary results from a calibration study performed in the Langley 6-inch expansion tube. Free-stream velocities from 5 to 7 km/sec are generated at hypersonic conditions with helium, air, and $CO_2$, resulting in normal shock density ratios from 4 to 19.

Measured shock shapes on a flat-faced cylinder model in the test gases were in good agreement with ideal-gas predictions based on an effective ratio of specific heats. Variation of the flat-faced cylinder diameter by a factor of 4 did not produce a significant effect on shock shape or normalized standoff distance, even for diameters as large as the test core diameter. A pronounced effect of diameter was observed for sphere models in air and $CO_2$, with normalized standoff distance increasing with decreasing diameter. Since viscous effects are negligible for the present conditions, this variation is attributed to nonequilibrium flow in the shock layer. Differences between measured and predicted shock detachment distance for a sphere increased with increasing distance from the stagnation region, indicating the possible existence of nonuniform free-stream flow properties for all three test gases. For the present air and $CO_2$ test conditions, the product of free-stream density and shock standoff distance should be greater than approximately $10^{-5}$ kg/m$^2$ to avoid nonequilibrium effects in the shock layer. Free-stream nonequilibrium in expansion-tube flow was shown to have a small effect on shock standoff distance for air, but an appreciable effect for $CO_2$. Comparison of measured standoff distance for a flat-faced cylinder to predicted values, obtained by using a program for predicting expansion-tube flow conditions in conjunction with a program for predicting flow past blunt bodies, indicated the $CO_2$ free-stream flow was near thermochemical equilibrium.

The preliminary investigation to determine flow characteristics of these test gases in the Langley 6-inch expansion tube showed test core flow quality, as inferred from

pitot-pressure profiles, and test repeatability were relatively good. Comparison of predicted and measured helium flow quantities indicated the existence of a totally reflected shock at the secondary diaphragm. For air and $CO_2$ test gases, the incident shock velocity in the acceleration section, hence free-stream velocity, was observed to decrease in traversing the acceleration section. Inclusion of this attenuation in the prediction was found to improve agreement with the experiment, and indicated the flow expansion was close to thermochemical equilibrium. The incident shock velocity was essentially constant along the acceleration section for helium.

## INTRODUCTION

The bow shock detachment distance has frequently been used for comparison of various theories for flow about blunt bodies at supersonic and hypersonic conditions and comparison of these theories with experimental results. The detachment distance is of practical importance in radiative heat transfer studies, since it determines the volume of gas available to radiate, and in the analyses of aerodynamic interference and aerodynamic heating. It has been recognized for nearly two decades that the primary factor governing the shock detachment distance of blunt bodies at hypersonic speeds is the normal shock density ratio. (For example, see refs. 1 to 9.) For hypervelocity entry of blunt vehicles into planetary atmospheres with equilibrium flow conditions, density ratios 3 to 4 times the values obtained in hypersonic ideal-air wind tunnels are encountered. For example, entry of an aeroshell into the atmosphere of Mars or Venus will produce density ratios as high as 20 to 25. These high values of density ratio are the result of excitation of vibration, dissociation, and ionization energy modes (commonly referred to as real-gas effects) of the atmospheric gas passing through the bow shock. As dissociation is initiated and driven towards completion, the density ratio increases; from mass conservation considerations, the corresponding shock detachment distance decreases (ref. 6).

The majority of shock detachment distance data demonstrating real-gas effects are analytical. Lack of experimental data at high free-stream velocities and density ratios is due, in part, to development and hardware problems associated with high-enthalpy facilities capable of generating hypersonic, real-gas flows. An alternate means of studying real-gas effects is to generate high density ratios at low enthalpies by using test gases characterized by low ratios of specific heats (refs. 10 to 12). A density ratio of approximately 12 has been obtained with $CF_4$ as the test gas in a conventional-type wind tunnel (refs. 12 and 13). However, this ratio of 12 falls short of the maximum values expected for planetary entry. The use of other gases in hypersonic wind tunnels which may yield higher density ratios without dissociation is presently under investigation (ref. 14).

An operational facility having the capability of generating a range of hypersonic-hypervelocity flow quantities in arbitrary test gases about stationary test models is the expansion tube. With this facility, real-gas effects on the flow field of models represent-

ative of entry vehicles may be studied in gas or gas mixtures corresponding to the proposed planetary atmosphere. Such an investigation was recently undertaken in the Langley 6-inch expansion tube. Shock detachment distances were measured for various blunt configurations in helium, air, and $CO_2$ test gases. These test gases were chosen since $CO_2$ is the primary constituent of Mars and Venus atmospheres; air is, of course, Earth's atmosphere; and helium exhibits ideal-gas behavior over a wide range of conditions. The corresponding range of normal shock density ratio for these test gases at the hypersonic-hypervelocity conditions of this investigation was 4 to 19. The upper value of density ratio, which corresponds to $CO_2$ test gas, is nearer to the maximum value expected for Martian or Venusian entry than previously published experimental data.

In conjunction with the shock shape measurements, presented herein are results from a calibration study performed in the Langley 6-inch expansion tube. The purposes for this calibration study were (1) to examine flow quality and test repeatability in various test gases and determine if satisfactory for model testing, and (2) to compare expansion-tube performance with predicted performance. Calibration and shock shape results are presented together in this report for several reasons. First, there are no published calibration results for the Langley 6-inch expansion tube. Second, the expansion tube is an extremely versatile facility and must be continually calibrated as flow conditions are varied and different test gases used. The sensitivity of flow properties to variation in running conditions requires studies of flow characteristics about test models to be preceded by a calibration with the same test gas and at the same running conditions. Last, the shock shape results are coupled to facility calibration. In a high enthalpy impulse facility such as the expansion tube, shock shapes may supply information on the thermochemical state of the free-stream flow and flow in the shock layer of a test model, as well as on the uniformity of the free-stream flow (refs. 15 and 16).

The primary purpose of this report is therefore twofold. First, to present shock shape results for spheres, spherically blunted cones, and flat-faced cylinder models in helium, air, and $CO_2$ gases. These data are added to the existing body of data at lower density ratios and extend this body of data to density ratios close to those expected in planetary entry. Second, to present results from a calibration study performed in the Langley 6-inch expansion tube with these test gases.

## SYMBOLS

| | |
|---|---|
| $a$ | speed of sound, m/sec |
| $d$ | diameter, m |
| $\ell$ | secondary diaphragm thickness, m |

| | |
|---|---|
| $L$ | distance downstream from secondary diaphragm, m |
| $L_a$ | length of acceleration section, m |
| $M$ | Mach number |
| $N_{Re}$ | unit Reynolds number, per meter |
| $p$ | pressure, $N/m^2$ |
| $r$ | radius, m |
| $R$ | expansion-tube radius, m |
| $t$ | time after arrival of incident shock into region ⑩, sec |
| $T$ | temperature, K |
| $U$ | velocity, m/sec |
| $U_s$ | incident shock velocity, m/sec |
| $x,r$ | cylindrical coordinates |
| $y$ | vertical distance from tube centerline, m |
| $Z$ | number of kmoles of dissociated gas per number of kmoles of undissociated gas |
| $\gamma$ | effective ratio of specific heats |
| $\gamma_E$ | isentropic exponent |
| $\Delta$ | shock standoff distance at centerline ($r = 0$), m |
| $\epsilon$ | normal shock density ratio, $\rho_{5s}/\rho_5$ |
| $\theta$ | cone semiapex angle, deg |

$\lambda$ percent deviation of free-stream velocity at distance $r = r_n$ or $r_b$ from centerline value (r = 0)

$\xi_\phi$ nondimensional error parameter (eq. (3))

$\rho$ density, $kg/m^3$

$\tau$ time interval between arrival of incident shock into region ⑩ and interface, sec

$\phi$ measured or calculated flow quantity

Subscripts:

A applied

b model base

c calculated

D secondary diaphragm

eff effective

I interface

m measured

n spherical nose

w model surface

1 state of quiescent test gas in front of incident shock in intermediate section

2 state of test gas behind incident shock in intermediate section

2r state of test gas behind totally reflected shock at secondary diaphragm

2s state of test gas behind standing shock at secondary diaphragm

3 driver gas following unsteady expansion

4 driver-gas conditions at time of primary-diaphragm rupture

5 state of test gas flow or free-stream conditions

5s static conditions behind bow shock of model positioned at test section

5t stagnation conditions behind bow shock of model positioned at test section

10 state of quiescent acceleration gas in front of incident shock in acceleration section

20 state of acceleration gas behind incident shock in acceleration section

Superscript:

* sonic point

## FACILITY

The Langley 6-inch expansion tube is basically a cylindrical tube, divided by two diaphragms (primary and secondary) into three sections. (See fig. 1.) The upstream section is the driver or high-pressure section. This section is pressurized at ambient temperature with a gas having a high speed of sound. (Greater operation efficiency is realized as driver-gas speed of sound increases.) The intermediate section is sometimes referred to as the driven section. This section is evacuated and filled with the desired test gas at ambient temperature. The driver and driven sections are separated by a double diaphragm apparatus capable of withstanding a maximum pressure differential of 68.95 $MN/m^2$. A single diaphragm may also be used between the driver and driven sections. The downstream section is referred to as the expansion or acceleration section. A weak, low-pressure diaphragm (secondary diaphragm) separates the driven and acceleration sections. Test models are positioned at the exit of the acceleration section. Flow through this section exhausts into a dump tank; hence, models are tested in an open jet. The operating sequence of the expansion tube is shown schematically in figure 1, and discussed in detail in reference 17.

For the present tests, the driver length was 2.44 m and the driver cross-sectional diameter was 16.51 cm. Double diaphragm mode of operation was employed to reduce randomness in pressure ratio across the primary diaphragm at time of rupture. Primary diaphragms were fabricated from stainless steel, and diaphragm thickness from the bottom of the cross-pattern grooves to the side facing the driver section was 2.54 mm. The volume of the double diaphragm section is small compared with the driver section, with the

ratio of double diaphragm section volume to driver section volume being 0.07. Intermediate section length was 4.65 m and acceleration section length was 16.98 m. The inside diameter of these two sections was 15.24 cm. The secondary diaphragm was 6.35-$\mu$m-thick mylar.

## SURVEY RAKE AND MODELS

Vertical pitot-pressure profiles at the test section were made with the nine-probe survey rake shown in figure 2(a). This rake had a probe spacing of 1.905 cm, and the outside diameter of each probe at the sensing surface was 7.87 mm (fig. 2(b)). The centerline of the center-rake probe was coincident with the expansion-tube centerline. As shown in figure 2(b), an overlapping baffle arrangement was used to protect the pressure instrumentation from particle contamination in the flow. (Principal sources of particle contamination are primary diaphragm petal tips, steel slivers along the rupture line, and mylar fragments from the secondary diaphragm. These particles are believed to arrive at the test section after the quasi-steady test period.) For results presented herein, the sensing surfaces of the survey-rake probes were positioned 4.13 cm downstream of the acceleration section exit.

Five sphere models having diameters $d_n$, ranging from 1.27 to 7.62 cm (fig. 3(a)), and four flat-faced cylinder models having diameters $d_b$, ranging from 1.91 to 7.62 cm (fig. 3(b)), were tested. Also tested were four spherically blunted cones having semiapex angles of $50^o$, $60^o$, $70^o$, and $80^o$ and bluntness ratio $r_n/r_b$ of 0.5 (fig. 3(c)). The $70^o$ blunted cone is representative of the Viking aeroshell configuration. Base diameter for all cone models was 5.08 cm. All models were fabricated from stainless steel, hence there was no charring or ablation of the model surface during the test-flow period. The model support system is shown schematically in figure 3(d). Flat-faced cylinder, sphere, and spherically blunted cone models were positioned 3.81, 1.59, and 3.49 cm, respectively, downstream of the acceleration section exit. Results presented herein are for zero angle of attack.

## INSTRUMENTATION

Since the expansion tube is characterized by extremely short test times (less than 250 $\mu$sec, or so, for the present results), pressure instrumentation must have very fast response to pressure change. Pitot pressure and expansion-tube wall pressure were measured with miniature piezoelectric (quartz) transducers having rise times of approximately 1 to 3 $\mu$sec. Each pressure transducer was used in conjunction with a charge amplifier, and the output signal was recorded from an oscilloscope with the aid of a camera. Representative oscilloscope films illustrating the static pressure variation at the

wall of the acceleration section (transducer positioned 1.88 m upstream of acceleration section exit) and the pitot-pressure variation with time are presented in figure 4 for air and helium test gases.

Shock shapes were obtained with a single-pass schlieren system utilizing a vertical knife edge. The point light source, which had a duration of approximately 150 nsec, was pulsed during the quasi-steady test-flow period. These shock shapes were recorded on 10.7- by 12.7-cm negatives. Representative schlieren photographs illustrating the shock shapes on the Viking aeroshell ($\theta = 70^{o}$) and flat-faced cylinder models with $CO_2$ test gas, as well as the pitot-pressure survey rake with air test gas, are shown in figure 5.

The propagation of the incident shock through the intermediate section (region ①, fig. 1) and the incident shock through the acceleration section (region ⑩, fig. 1) was monitored continuously by using a microwave interferometer technique. This microwave system generates a standing wave in the tube, and the interference of the reflected signal from the shock wave with the transmitted signal creates alternate maxima and minima in impedance as the distance from antenna to shock wave changes with time. (The antenna consisted of a 0.61-mm-diameter wire stretched vertically across the expansion-tube diameter and positioned downstream of the test model. See fig. 5.) The varying periodic signal is recorded on a high-speed (60 rps) drum-camera-oscilloscope combination. The signal generator was adjusted to put out a 1.326 GHz signal. Film speed was checked for each test by utilizing a time mark generator to place marks on the film representing 100 $\mu$sec increments.

Due to insufficient electron density at the shock front, microwave results were not obtained in the intermediate section with helium and $CO_2$ test gases. Hence, the more conventional means of determining incident shock velocity by positioning pressure, heat transfer, and photomultiplier instrumentation along the wall of the tube at known intervals was also used. This procedure allows a distance-time history to be generated, and the average incident shock velocity to be determined between successive instrumented stations. Oscilloscopes used to record output of instrumentation along the wall were delayed by digital time delay generators to enable faster sweep rates. The output of this instrumentation also started and stopped counter-timers. The time for the shock to travel between stations was obtained from manual reading of oscilloscope films and from counter-timer readings.

## DATA REDUCTION AND UNCERTAINTY

### Pressure

Oscilloscope films of pitot pressure and tube wall pressure traces were read manually at test times $t$ of 100 to 200 $\mu$sec. Each pitot-pressure probe (that is, each pres-

sure transducer and associated charge amplifier and oscilloscope) was calibrated statically before and after the test series, as were tube wall pressure transducers. Uncertainties in such pressure measurements are dependent on many factors, such as pressure level with regard to transducer sensitivity, calibration technique (static or dynamic), change in calibration factor during course of tests, transducer linearity, oscilloscope accuracy, quality of oscilloscope traces with respect to the signal-to-noise ratio, and data read-up procedure. Hence, specifying precise uncertainties for these pressure measurements is not possible. On the basis of this and previous experience, the maximum uncertainties in pressure measurements are believed to be less than approximately ±20 percent for tube wall pressure $p_5$, and less than approximately ±10 percent for pitot pressure $p_{5t}$.

## Shock Detachment Distance

The detachment distance of the leading edge of the bow shock from the model surface was read manually from enlargements of schlieren photographs to approximately model size for the larger diameter sphere and flat-faced cylinder models and to twice model size for the cones and smaller models. These readings were made by using a digitizing system having a sensitivity of 100 counts per 2.54 mm. For a number of tests, the shock standoff distance $\Delta$ was also inferred from densitometer scans of the negatives. These standoff distances were within 6 percent of those obtained by manual reading. Due to lower flow density, refractivity, and density gradient across the shock for helium, the shock resolution on enlargements for helium tests was less than that for other test gases. Hence, a greater uncertainty in reading the shock displacement exists for the helium tests because of the poorer definition of the leading edge of the bow shock. High illumination on the model forebody for the air tests tended to obscure the shock displacement. A shutter device having an open-shut time less than 50 $\mu$sec was employed with some success for these tests. The maximum uncertainty in measured shock displacement is believed to be less than ±10 percent.

## Shock Velocity

The distance between successive minima or successive maxima of the microwave traces for the incident shock in the intermediate section and acceleration section was digitized by using a precision film reader having a calibration factor of 30.11 micrometers per count. By running a brass plug down an accurately determined length of the expansion tube and counting cycles, the distance between successive minima or successive maxima was verified to correspond to a movement of 22.71 cm. Since 5.08 cm of film length corresponds to 1 msec, the time, hence the corresponding velocity, between successive minima or successive maxima may be determined. Microwave film traces for these incident shocks in the intermediate and acceleration sections were read every cycle

(successive minima or successive maxima). A first-order least-squares curve fit was applied to the resulting values of incident shock velocity along the acceleration section for a given test. Incident shock velocities, $U_{s,10}$, used as input to predict test-section flow quantities, were obtained from this curve fit at a distance 0.83 m upstream of the tube exit.

An average shock velocity between stations in the intermediate and acceleration sections was determined by knowing the distance between stations and the time for the shock to travel this distance. Times were read from pressure, heat transfer, and photomultiplier traces on oscilloscope film, and from counter-timers. Uncertainties in instrumentation response, oscilloscope time scale accuracy, and reading of oscilloscope film are believed to result in a corresponding uncertainty in the time interval for incident shock arrival between successive stations of less than 5 percent.

For the present study, uncertainties in incident shock velocity in the intermediate section and in the acceleration section are believed to be less than ±2.5 percent. These uncertainties are based on both procedures (microwave and generation of distance-time history) for inferring shock velocity.

## PREDICTION METHODS

### Expansion-Tube Flow

Free-stream and postnormal shock flow conditions at the test section were calculated by using the thermochemical equilibrium computer program of reference 18. Inputs to this program were (1) inferred acceleration-gas—test-gas interface velocity $U_5$, (2) measured tube wall or free-stream static pressure $p_5$, and (3) measured pitot pressure $p_{5t}$. Although originally written to obtain accurate test-section conditions for real gases $CO_2$, $N_2$, $O_2$, and Ar or mixtures of these gases, this program (ref. 18) was modified to include real He and $H_2$ gases also.

In the operating sequence of the expansion tube, an unsteady expansion is used to accelerate the test gas. Due to the rapid expansion of the flow through the expansion fan, vibrational relaxation and dissociative recombination may lag translation (ref. 19). As the temperature and density of the flow decrease in the expansion, vibrational energy and chemistry tend to remain unchanged (that is, become frozen) during the expansion process. The complex problem of predicting flow conditions for a nonequilibrium, unsteady expansion process is not considered herein. Instead, limiting situations corresponding to zero (frozen) and infinite (equilibrium) relaxation rates in the expansion are computed by using the real-gas mixture program of reference 17. This program performs an isentropic, one-dimensional, unsteady expansion from the conditions behind the incident shock in the intermediate section to the test-section velocity.

The flow energy lost in the rupture of the secondary diaphragm must result in an upstream-facing shock wave reflected from this diaphragm (ref. 20). When the diaphragm ruptures, the resulting expansion fan overtakes and weakens the reflected shock. It is sometimes assumed that the reflected shock has been weakened to a standing shock by the time it processes the flow which eventually becomes the test flow. Therefore, the possible existence of a standing normal shock at the secondary diaphragm was considered in reference 17. For the present study, the program of reference 17 was modified to include a totally reflected normal shock at the secondary diaphragm, thereby providing a limiting case for this shock-wave reflection phenomenon. In reference 17, freezing of the vibrational energy and chemistry is assumed to occur in the region behind the incident shock in the intermediate section (region ②) or behind the shock resulting from incident shock reflection at the secondary diaphragm (region ②s or ②r). For the frozen expansion, the flow immediately behind the bow shock of a model positioned at the test section is assumed to be in thermochemical equilibrium or frozen at the free-stream composition.

## Blunt Body Shock Shapes

Calculated shock shapes presented herein were obtained by using the programs of references 15, 21, and 22. Flat-faced cylinder and spherically blunted cone shock shapes were calculated by using the one-strip integral method of reference 21. This method is restricted to an inviscid, ideal gas (constant ratio of specific heats) and to blunt bodies (spherically blunted cone, flat-faced cylinder, and concave and convex spherical caps) with sonic corners. As the cone semiapex angle decreases for the spherically blunted cone models, the sonic point is expected eventually to move off the corner and forward onto the spherical segment. This departure of the sonic point from the corner results in a nonconvergence condition in the program of reference 21. For such cases and for the sphere models, shock shapes were calculated by using the programs of references 15 and 22. The method of reference 15 is a two-step, time-dependent method of second-order accuracy for calculating supersonic flow about axisymmetric blunt bodies for perfect or equilibrium gas flow. Only the perfect gas mode of this method was exercised for the present study. Included in the method of reference 15 and employed herein is the capability of calculating the effect of a parabolic free-stream velocity distribution (flow nonuniformity) on shock shape. The calculation procedure of reference 22 is a direct procedure restricted to ideal-gas, inviscid flow within the shock layer. Shock shapes presented herein and designated as being from reference 15 were generated by Richard W. Barnwell; similarly, predictions designated as being from reference 22 were generated by Ernest V. Zoby.

The basic inputs to the programs of references 15, 21, and 22 are Mach number, ratio of specific heats, and model geometry. Values of $M_{eff}$ and $\gamma_{eff}$ were used as input, as well as free-stream and postshock values (that is, $M_5$ and $\gamma_{E,5}$, and $M_5$

and $\gamma_{E,5s}$). These effective values were determined from ideal-gas, normal shock relations (ref. 23) and are as follows:

$$\gamma_{eff} = \frac{1 + \epsilon\left(1 - \frac{2}{M_{eff}^2}\right)}{\epsilon - 1} \tag{1}$$

and

$$\frac{p_{5t}}{p_5} = \left[\frac{(\gamma_{eff} + 1)M_{eff}^2}{2}\right]^{\frac{\gamma_{eff}}{\gamma_{eff}-1}} \left[\frac{\gamma_{eff} + 1}{2\gamma_{eff}M_{eff}^2 - (\gamma_{eff} - 1)}\right]^{\frac{1}{\gamma_{eff}-1}} \tag{2}$$

where $p_{5t}$ and $p_5$ are measured quantities and the normal shock density ratio $\epsilon$ was obtained from the thermochemical equilibrium program of reference 18. Equations (1) and (2) were solved by iteration for $M_{eff}$ and $\gamma_{eff}$ until successive values of $M_{eff}$ were within 0.25 percent.

The effective ratio of specific heats is defined in references 13 and 14 as the value of $\gamma_{eff}$ which gives the correct normal shock density ratio $\epsilon$ when free-stream Mach number $M_5$ is used in equation (1) in place of $M_{eff}$. From this equation, $\gamma_{eff}$ is observed to be essentially a function of $\epsilon$ only for large values of Mach number $\left(\gamma_{eff} \to \frac{\epsilon + 1}{\epsilon - 1} \text{ as } M \to \infty\right)$. The dependence of $\gamma_{eff}$ on Mach number for two values of normal shock density ratio (representative of those obtained in the present study for air and $CO_2$) is illustrated in the following table:

| M | $\gamma_{eff}/(\gamma_{eff})_{M\to\infty}$ for – | |
|---|---|---|
| | $\epsilon = 11.1$ | $\epsilon = 18.8$ |
| 4 | 0.885 | 0.881 |
| 5 | .927 | .924 |
| 6 | .949 | .947 |
| 7 | .963 | .961 |
| 8 | .971 | .970 |
| 10 | .982 | .981 |
| 12 | .987 | .987 |
| 14 | .991 | .990 |

Replacing $M_{eff}$ by the corresponding value of $M_5$ will result in a small change in computed $\gamma_{eff}$, provided $M_{eff}$ and $M_5$ are greater than seven, or so. For the conditions of this study, shock detachment distances calculated by using inputs $M_{eff}$ and $\gamma_{eff}(\epsilon, M_{eff})$ will be essentially the same as detachment distances calculated by using inputs $M_5$ and $\gamma_{eff}(\epsilon, M_5)$.

## TEST CONDITIONS

Test gases were helium, dry air, and $CO_2$, and the driver gas was unheated helium at a nominal pressure of 33 $MN/m^2$. Test conditions were selected to yield approximately the same $U_5$ for air and $CO_2$ and same order of magnitude for $p_5$ for the three test gases. This selection represented a successful attempt to avoid the range of test conditions where tube wall boundary-layer transition is encountered during the test flow. This latter phenomenon is detrimental to test core flow quality (ref. 20). The quiescent test gas pressure $p_1$, for all test gases, was 3.45 $kN/m^2$. For a given test, the acceleration gas was the same as the test gas. Quiescent acceleration gas pressure $p_{10}$ varied from 3.1 $N/m^2$ for $CO_2$ to 22.0 $N/m^2$ for helium. Quasi-steady test time varied from 200 to 250 $\mu$sec for all test gases.

Nominal values of measured inputs to the thermochemical equilibrium program of reference 18 yielded the following flow conditions for each test gas:

| Test gas | $p_5$, $kN/m^2$ | $\rho_5$, kg/m3 | $T_5$, K | $\gamma_{E,5}$ | $U_5$, km/sec | $M_5$ | $N_{Re,5}$, per meter | $\epsilon$ | $\gamma_{E,5s}$ | $p_{5t}$, $kN/m^2$ | $T_{5t}$, K |
|---|---|---|---|---|---|---|---|---|---|---|---|
| He . . . . | 1.66 | 0.00201 | 398 | 1.67 | 7.06 | 6.02 | $5.48 \times 10^5$ | 3.69 | 1.67 | 88.9 | 5194 |
| Air . . . | 2.59 | 0.00718 | 1255 | 1.32 | 5.32 | 7.72 | 7.95 | 11.11 | 1.15 | 196.5 | 6247 |
| $CO_2$ . . . | 1.21 | 0.00486 | 1315 | 1.17 | 4.95 | 9.18 | 5.15 | 18.81 | 1.15 | 116.5 | 3827 |

The program of reference 18 was modified to calculate the following flow quantities (corresponding to nominal values of measured inputs) of interest in the shock shape study:

| Test gas | $M_{eff}$ | $\gamma_{eff}$ | $N_{Re,5s}$, per meter |
|---|---|---|---|
| He . . . . . | 6.02 | 1.67 | $0.95 \times 10^5$ |
| Air . . . . . | 8.90 | 1.17 | 2.60 |
| $CO_2$ . . . . . | 9.94 | 1.09 | 2.38 |

The models tested for shock shapes were not instrumented, and the relatively large model diameters prohibited installation of a pitot-pressure probe in the inviscid test core without

disturbing the model flow field. Nominal values of $p_5$ and $U_5$ for each test gas were obtained from tests with the survey rake (calibration phase of study) and with the models (shock shape phase of study), whereas nominal values of $p_{5t}$ for each test gas were obtained from the center probe of the survey rake.

## RESULTS AND DISCUSSION

### Expansion-Tube Flow Characteristics

Pitot-pressure profiles.- Vertical pitot-pressure profiles for helium, air, and $CO_2$ are shown in figure 6 for a test time $t$ of 150 $\mu$sec. Test repeatability, always a primary concern with impulse-type facilities, is good for helium and air, and somewhat less satisfactory for $CO_2$. This poorer repeatability for $CO_2$ is due, in part, to the difficulty of repeating and maintaining the lower value of quiescent acceleration gas pressure required for the $CO_2$ tests. The test core was defined as the relatively flat section of the vertical pitot-pressure profile about the tube centerline, for which the pitot pressure is within 10 percent of the average of the three center probes. The boundaries of the test core were uncertain in several instances because of the nature of the pitot-pressure distributions and relatively large survey-rake probe spacing of 1.91 cm. The test core for all three test gases is approximately half the expansion-tube diameter (7.62 cm). For the present tests, the free-stream Reynolds number based on pitot-probe sensing-surface diameter was greater than $4 \times 10^3$. Hence, pitot-pressure measurements in the test core should be essentially free from Reynolds number effects (ref. 24).

Incident shock velocity along acceleration section.- Incident shock velocity along the acceleration section, as inferred from microwave measurements, is shown in figure 7 for the three test gases. These data correspond to the pitot-pressure profile results presented in figure 6. Shock velocity is plotted as a function of distance downstream of the secondary diaphragm $L$. Least-squares line fits to the data between $L$ equal to 2.27 m and 16.98 m (acceleration section exit) are also presented. The fact that microwave measurements were obtained for helium flow in the acceleration section is believed to be the result of trace contaminants in the helium acceleration gas. Since the Mach number of the incident shock into the acceleration section $\left(U_{s,10}/a_{10}\right)$ for the helium tests was approximately 7, the temperature immediately behind this shock was approximately 5000 K (ref. 25). For the pressure levels of this flow, this temperature is insufficient for ionization of the helium gas; hence, the electron concentration tracked by the microwave signal is probably the result of ionization of flow contaminants introduced into the low pressure quiescent acceleration gas by leakage and outgassing. Calculated pressure behind the incident shock in the helium acceleration gas is in good agreement with measured free-stream static pressure; thus, the level of contaminants should not have an appreciable

influence on helium results presented herein. The data scatter of figure 7 is primarily a result of reading successive maxima or minima of the microwave output.

The line fits to the data for air and $CO_2$ (figs. 7(b) and 7(c), respectively) illustrate that the shock velocity decreases in traversing the acceleration section for these test gases, but remains essentially constant for helium (fig. 7(a)). Hence, it appears that a wave structure overtakes the test flow for air and $CO_2$ test gases (ref. 20).

The run-to-run variation of the difference in $U_{s,10}$ between L equal to 2.27 m and 16.98 m $\Delta U_{s,10}$ is shown in figure 8. These results were obtained during the shock shape phase of this study (to be discussed subsequently) with helium, air, and $CO_2$ test gases. Values of $p_1$ and $p_{10}$ and nominal values of $p_4$ were the same as for the calibration tests. The values of $\Delta U_{s,10}$ were obtained from least-squares line fits to $U_{s,10}$ data. Average incident shock velocity attenuation in traversing the acceleration section for air and $CO_2$ is approximately 330 and 310 m/sec, respectively. Repeatability for a relatively large number of tests was within 15 percent, or so, for both gases. Run-to-run variation in $\Delta U_{s,10}$ for helium was much greater than that for air or $CO_2$. The average value of $\Delta U_{s,10}$ was approximately -20 m/sec, thereby representing a slight acceleration in $U_{s,10}$ with increasing distance from the secondary diaphragm. Flow attenuations of 150 to 300 m/sec were observed in the Langley pilot model expansion tube (ref. 20) for air test gas. This attenuation was attributed in reference 20 to downstream-facing expansion waves generated by the growing boundary layer upstream. A decrease in flow velocity occurs when these waves intercept the flow.

Distance-time histories for the incident shock in the acceleration section are shown in figure 9 for all three test gases. Zero time corresponds to the primary diaphragm opening process as detected by an accelerometer. Velocities inferred from response of pressure, heat transfer, and photomultiplier instrumentation (open symbols in fig. 9) are in relatively good agreement with the microwave results of figure 7 for all test gases. This finding confirms that the microwave signal was tracking the incident shock in the acceleration gas for these gases.

Free-stream (interface) velocity.- Since free-stream velocity is a basic quantity of interest, it is necessary to infer the acceleration-gas—test-gas interface velocity, which is not measured, from the measured incident shock velocity in the acceleration section. (The interface velocity is assumed to be a good representation of the free-stream velocity immediately behind the interface (ref. 26).) This inference of the interface velocity may be performed by considering the theoretical results of reference 27 for real-air flow. For air test gas, the pitot-pressure probe response, which is denoted in figure 9 by shaded symbols, showed the time interval between arrival of the incident shock at the test section and the test-air—acceleration-air interface $\tau$ is about 25 to 30 $\mu$sec. In figure 10, predicted time intervals (ref. 27) between arrival of the incident shock and the

test-air—acceleration-air interface are shown as a function of distance downstream from the secondary diaphragm for several values of $U_{s,10}$. These calculated results assume laminar flow and are based on the present values of $p_{10}$ (8 N/m$^2$ for air), $L_a$ (16.98 m), and tube diameter (0.1524 m). The dashed lines of figure 10 represent time intervals predicted by using simple theory for ideal air (ref. 28). Comparison of the measured time interval for air, where the nominal value of measured $U_{s,10}$ is 5.32 km/sec, with calculations based on the results of reference 27 shows measured and predicted time intervals to be in good agreement.

Ratios of incident shock velocity $U_{s,10}$ to test-air—acceleration-air interface velocity $U_I$, as computed from the results of reference 27, are shown as a function of distance downstream of the secondary diaphragm in figure 11. The predicted interface velocity is within 1 percent of the incident shock velocity over the downstream 75 percent of the acceleration section for the range of $U_{s,10}$ considered, including the measured value for air. At the acceleration-section exit, the interface velocity is essentially equal to $U_{s,10}$. That is, the maximum separation distance between the incident shock and interface is reached upstream of the exit. Based on the predictions using reference 27, free-stream velocity $U_5$ is assumed equal to $U_{s,10}$ at the test section for all test gases, and thus may be inferred directly from microwave measurements. (See the section "Data Reduction and Uncertainty.")

Test repeatability.- Before comparing measured flow quantities with predicted expansion-tube flow quantities, the run-to-run variation of basic measured quantities will be illustrated. In figure 12, the variations of incident shock velocity in the intermediate section $U_{s,1}$ (fig. 12(a)), test-gas—acceleration-gas interface velocity near the tube exit $U_5$ (fig. 12(b)), and wall static pressure measured 1.89 m upstream of the tube exit $p_5$ (fig. 12(c)) are shown for a number of expansion-tube runs. As the case for $\Delta U_{s,10}$ (fig. 8), these results were obtained during the shock shape phase of this study. The data scatter in $U_{s,1}$ (obtained from counter readings, thereby representing an average velocity, see the section "Instrumentation") and $U_5$ (inferred from microwave measurements) is observed to be small for all three test gases. This small degree of data scatter is attributed primarily to the double diaphragm mode of operation employed in this investigation and the small leakage of the facility while under vacuum. Values of $p_5$ are shown in figure 12(c) for test times of 100 and 200 $\mu$sec. It is observed that $p_5$ decreases with test time for all three test gases, and run-to-run repeatability is poorer than that observed for measured velocities $U_{s,1}$ and $U_5$. Mean values of $U_{s,1}$ used to predict expansion-tube performance and mean values of $U_5$ and $p_5$ used to calculate test-section flow conditions for helium, air, and $CO_2$ test gases, along with limits of data scatter in these quantities (fig. 12), are as follows (mean values of $U_{s,1}$ were the same as average values for all three test gases; mean values of $U_5$ were within 0.5 percent of average values for air and $CO_2$ and the same for helium):

| Test gas | $U_{s,1}$, m/sec | | $U_5$, m/sec | | $p_5$, N/m$^2$ | |
|---|---|---|---|---|---|---|
| | Mean value | Data scatter about mean, percent | Mean value | Data scatter about mean, percent | Mean value | Data scatter about mean, percent |
| He . . . . . | 3888 | 2.5 | 7058 | 1.6 | 1655 | ≈21 |
| Air . . . . . | 2865 | 1.1 | 5323 | 1.3 | 2586 | ≈20 |
| $CO_2$ . . . . . | 2539 | 1.1 | 4949 | 1.7 | 1207 | ≈17 |

Comparison of measured and predicted performance.- Measured wall pressure $p_5$ and pitot pressure on the expansion-tube centerline $p_{5t}$ are compared with predicted values (ref. 17) in figures 13 to 15 for the three test gases. Nominal values of measured incident shock velocity in the intermediate section $U_{s,1}$ were used as input to the program of reference 17 to determine flow conditions behind the incident shock. Microwave measurements of the incident shock velocity into the intermediate section (region ①) for air revealed the incident shock initially accelerates, then attenuates with distance downstream from the primary diaphragm. (Microwave results were not obtained in the intermediate section with helium and $CO_2$ test gases.) The maximum value of $U_{s,1}$ for air occurred approximately 2.5 m downstream of the primary diaphragm. Values of $U_{s,1}$ for the three test gases used as input were inferred from response of pressure instrumentation (read from counters) located 7 cm to 1.14 m upstream of the secondary diaphragm. The incident shock velocity for air is attenuating slightly in this region, and the value of $U_{s,1}$ at the time of encounter with the secondary diaphragm may be somewhat less than $U_{s,1}$ inferred from counter readings. Shown in figures 13 to 15 is the effect of a standing normal shock and totally reflected normal shock at the secondary diaphragm for both thermochemical equilibrium and frozen flow expansions. The effect of flow attenuation in the acceleration section is also shown in figures 14 and 15 for an equilibrium expansion and the limits of no shock reflection at the secondary diaphragm and a totally reflected shock. A method for determining the effect of flow attenuation on free-stream (region ⑤) flow quantities is discussed in reference 20. This method results in the shifting of a $U_5$-$p_5$ curve, which does not include the effect of flow attenuation, by $U_5 - 2\Delta U_5$ for given values of $p_5$. For example, a given value of $(U_5,p_5)$ on the air curve (fig. 14(b)) for an equilibrium expansion and no shock reflection at the secondary diaphragm is displaced to the left and corresponds to $(U_5 - 664,p_5)$, since $\Delta U_5$ for air is approximately 332 m/sec. The calculation of flow attenuation effects on postnormal shock quantities such as $p_{5t}$ was made by using the program of reference 17. Following the computation of the equilibrium expansion to region ⑤ and normal shock crossing, the velocity $U_5$ was set equal to $U_5 - 2\Delta U_5$ and the shock crossing procedure repeated.

An upper limit for the effect of flow attenuation was obtained by using attenuation in $U_{s,10}$ instead of $U_I$ to determine this effect for each gas. Attenuation in interface velocity, which is the quantity of interest in examining the effect of flow attenuation, was not measured. However, attenuation in interface velocity is somewhat less than that for the incident shock velocity, which was measured. This is illustrated in figure 16 for air test gas, where incident shock velocity $U_{s,10}$ and acceleration-air—test-air interface velocity $U_I$ are plotted as a function of distance downstream of the secondary diaphragm. The solid line denotes the least-squares line fit to microwave measurements for an air test. Values of $U_{s,10}$ represented by this line were used in conjunction with reference 27 to obtain corresponding values of $U_I$ as a function of L. From figure 16, the interface velocity for air accelerates to a maximum value at a distance downstream of the secondary diaphragm of approximately 3.5 m, then attenuates. At this distance of 3.5 m, $U_{s,10}$ is 1.013 times the predicted value of $U_I$, with agreement between these velocities improving with increasing distance downstream of 3.5 m. The attenuation in measured $U_{s,10}$ for this air test was found to be approximately 320 m/sec, whereas the predicted (ref. 27) attenuation in interface velocity is approximately 230 m/sec. Thus, using attenuation in measured $U_{s,10}$ provides an upper limit for this effect.

The shaded regions of figures 13 to 15 denote the effect of previously discussed run-to-run uncertainties in $U_{s,1}$ for equilibrium expansion with no shock reflection at the secondary diaphragm and no flow attenuation. This shaded region is presented to illustrate that relatively small uncertainties in $U_{s,1}$ result in large uncertainties in predicted $p_5$ and $p_{5t}$ for a given $U_5$. Hence, to minimize uncertainty in predicted expansion-tube test-section flow conditions, an accurate determination of $U_{s,1}$ is required. The cross-hatched regions of figures 13 to 15 represent the range of uncertainty in measured flow quantities $p_5$, $p_{5t}$, and $U_5$.

Predicted values for equilibrium and frozen flow were the same for helium, indicating an absence of ionization of the helium in the flow cycle. Since predictions for a standing shock at the secondary diaphragm for helium were very close to those for no shock reflection, the case for a standing shock is not presented in figure 13. Also, the effect of flow attenuation is not included, since the average value of $\Delta U_{s,10}$ was observed (fig. 8) to be nearly zero for helium. Measured values of $p_{5t}$ and $p_5$ are greater than the predicted values for a given $U_5$, and best agreement is obtained for the case where a totally reflected shock at the secondary diaphragm is included in the prediction of reference 17.

The primary reason for employing helium as the test gas was to divorce possible effects of flow chemistry on test-section flow quantities from the gas dynamics or fluid mechanics of the flow. The absence of flow chemistry for the helium tests provides an approximate "model" of the expansion-tube fluid mechanics, thus providing a basis from which to examine possible effects of chemistry for the other gases. This model is approx-

imate due to differences in viscous effects and wave characteristics between helium flow and flow of the other test gases. For example, the opening time of the secondary diaphragm is roughly proportional to $\sqrt{\rho_D \ell / p_A}$ (ref. 29). For the present study, secondary diaphragm density $\rho_D$ and thickness $\ell$ were the same for all test gases. However, the calculated pressure behind a reflected shock at the secondary diaphragm (which corresponds to the applied pressure $p_A$) is approximately 7 times that of helium for air and 16 times that of helium for $CO_2$. Secondary diaphragm opening times for helium should be roughly 2.7 times those for air and 4 times those for $CO_2$. Conditions yielding the longest diaphragm opening times should show the most pronounced effects of shock reflection. Thus, the effect of shock reflection from the secondary diaphragm is expected to be most pronounced for helium and least pronounced for $CO_2$.

Figures 14 and 15 for air and $CO_2$ test gas, respectively, show a large effect of this shock reflection at the secondary diaphragm on predicted frozen flow expansions. In reference 17, the flow is assumed to freeze in the region behind the incident shock or the shock resulting from reflection at the secondary diaphragm. Thus, the large effect of shock reflection observed in figures 14 and 15 on predicted frozen flow quantities is due to increases in dissociation between the cases for no shock reflection (incident shock) and a standing shock or totally reflected shock.

For air and $CO_2$, the prediction method which provides the best overall agreement with measured quantities assumes an equilibrium expansion, no shock reflection, and includes flow attenuation. This comparison of measured air and $CO_2$ flow quantities with predicted values does not provide sufficiently accurate information to deduce the thermochemical state of the expansion-tube flow, as evident from the following considerations:

(1) The uncertainty in measured quantities $p_5$, $p_{5t}$, and $U_5$

(2) The effect of uncertainty in measured $U_{s,1}$ on predicted flow quantities and the fact that values of $U_{s,1}$ used for air may be somewhat high

(3) The shock reflection at the secondary diaphragm and attenuation of the incident shock into the acceleration section are observed phenomena

(4) The attenuation in $U_{s,10}$ was used to predict the effect of flow attenuation, thereby yielding an upper limit for this effect

(5) The helium results of figure 13 infer existence of a totally reflected shock

(6) The findings of reference 19 indicated the presence of nonequilibrium flow for oxygen-nitrogen test gas mixtures in the Langley pilot model expansion tube.

Additional data on this subject will be discussed subsequently.

Uncertainty in calculated test-section flow quantities.- An important consideration in interpreting results from impulse-type facilities is the uncertainty in calculated flow

quantities resulting from uncertainties in measured inputs. The sensitivity of calculated free-stream and postnormal shock flow quantities to variation in measured inputs $p_5$, $p_{5t}$, and $U_5$ was determined by using the program of reference 18. The results of this error analysis are shown in figure 17, where the error parameter $\xi_\phi$ is plotted for various free-stream and postshock flow quantities for helium, air, and $CO_2$ test gases. The parameter $\xi_\phi$ is defined as

$$\xi_\phi \equiv \frac{\phi_{error} - \phi_{correct}}{\phi_{correct}} \times 100 \tag{3}$$

where $\phi$ represents the measured or calculated flow quantity of interest. The "correct" inputs used to obtain the "correct" calculated flow quantity correspond to the nominal values of $p_5$, $p_{5t}$, and $U_5$. (See the section "Test Conditions.") Maximum uncertainty in inputs $p_5$, $p_{5t}$, and $U_5$ was ±20 percent, ±10 percent, and ±2.5 percent, respectively. These maximum uncertainties for $p_5$ and $U_5$ are greater than the limits of data scatter about the mean (fig. 12), and will yield conservative corresponding uncertainties in calculated flow quantities. The open symbols of figure 17 denote one of the inputs was varied to the maximum uncertainty while the remaining two inputs were held constant at their nominal value. The closed symbols denote the case where all three inputs were varied to their maximum uncertainty so as to yield the maximum corresponding uncertainty in calculated flow quantities $M_5$ and $N_{Re,5}$.

Naturally, the type of investigation being conducted in a facility would dictate what flow quantities are most important and what limits of uncertainty in these quantities can be tolerated. Maximum uncertainties in quantities of primary interest in the present shock shape study for helium, air, and $CO_2$ test gases are presented in the following table. These values correspond to the combination of input uncertainties which yield the maximum uncertainty in calculated $M_5$ (represented by the shaded symbols of fig. 17; $\xi_{p_5} = -20$, $\xi_{U_5} = -2.5$, $\xi_{p_{5t}} = 11.1$).

| Test gas | Maximum uncertainty, percent, for – | | | | | | | |
|---|---|---|---|---|---|---|---|---|
| | $M_5$ | $\gamma_{E,5}$ | $N_{Re,5}$ | $\rho_{5s}/\rho_5$ | $N_{Re,5s}$ | $\gamma_{E,5s}$ | $\gamma_{eff}$ | $M_{eff}$ |
| He . . . . . | 17.8 | 0 | 48.8 | 2.1 | 20.0 | 0 | 0 | 18.4 |
| Air . . . . . | 16.8 | 2.3 | 44.7 | -1.0 | 16.3 | 0.5 | 0.8 | 17.8 |
| $CO_2$ . . . . . | 17.1 | 1.4 | 46.2 | 2.9 | 17.0 | -0.7 | 0.3 | 18.3 |

## Shock Shapes

Uncertainties in predicted shock shapes.- Before discussing measured shock shapes, predicted shock shapes from the ideal gas integral method of reference 21 will be presented. Basic inputs to the program of reference 21 are Mach number, ratio of specific heats, and body geometry. Inputs considered herein are free-stream isentropic exponent $\gamma_{E,5}$, postnormal shock isentropic exponent $\gamma_{E,5s}$, and effective ratio of specific heats $\gamma_{eff}$ (eq. (1)). For inputs $\gamma_{E,5}$ and $\gamma_{E,5s}$, the corresponding Mach number input is $M_5$ and for input $\gamma_{eff}$, $M_{eff}$ is input. Now, uncertainties in predicted flow quantities will naturally result in corresponding uncertainties in calculated shock detachment distance. The effect of uncertainties in inputs $\gamma_{eff}$ and $M_{eff}$ for helium, air, and $CO_2$ is shown in figure 18 for a flat-faced cylinder and a spherically blunted cone having a semiapex angle $\theta$ of $70^o$ and bluntness ratio $r_n/r_b$ of 0.5 (Viking aeroshell). The uncertainty between the maximum and minimum values of calculated shock standoff distance $\Delta/r_b$, as well as the corresponding uncertainty between maximum and minimum values of inputs $\gamma_{eff}$ and $M_{eff}$ used in this example, are as follows for the three test gases:

| Test gas | Maximum uncertainty, percent, for – | | | |
|---|---|---|---|---|
| | $\gamma_{eff}$ | $M_{eff}$ | $\Delta/r_b$ (flat-faced cylinder) | $\Delta/r_b$ (spherically blunted cone, $\theta = 70^o$, $r_n/r_b = 0.5$) |
| He . . . . . | 0 | 26.9 | 3.4 | 6.0 |
| Air . . . . . | 1.4 | 24.1 | 0.2 | 0.7 |
| $CO_2$ . . . . . | 0.6 | 28.3 | 3.6 | 13.4 |

The uncertainty in calculated $\Delta/r_b$ for these cases is within the ±10 percent uncertainty for measured values of $\Delta/r_b$.

Several points of interest may be observed from figure 18. The uncertainty in predicted shock shapes for helium is due only to uncertainty in input $M_{eff}$, since ideal-helium behavior exists ($\gamma_{eff}$ is constant). This relatively small variation in shock detachment distance, corresponding to a much larger variation in $M_{eff}$, is expected (Mach number independence principle, ref. 30). The calculated shock detachment distance is observed to decrease with decreasing $\gamma_{eff}$ (increasing normal shock density ratio $\epsilon$) and decrease with decreasing model bluntness from a flat-faced cylinder to a spherically blunted cone. As the model bluntness decreases, the uncertainty in calculated shock detachment distance increases, indicating a greater sensitivity to inputs $\gamma_{eff}$ and $M_{eff}$ for the less blunt bodies. Although not shown explicitly in figure 18,

calculated shock detachment distance is quite sensitive to input $\gamma_{eff}$, with this sensitivity increasing as the value of $\gamma_{eff}$ decreases. At low values of $\gamma_{eff}$, input $\gamma_{eff}$ must be known accurately to ensure reasonably accurate values of calculated shock detachment distance.

Shock shapes for flat-faced cylinder.- Measured shock shapes for a flat-faced cylinder having a diameter $d_b$ of 5.72 cm are shown in figure 19 for helium, air, and $CO_2$ test gases. The expected decrease in measured shock detachment distance with increasing $\epsilon$, even though $M_5$ is increasing, is illustrated in this figure. (From mass conservation, as the density in the postshock region increases, the shock standoff distance must decrease in order for the mass flow away from the stagnation region in the shock layer to remain nearly constant.) The measured $\Delta/r_b$ decreases by a factor of approximately 2.5 as $\epsilon$ increases fivefold. Calculated shock detachment distances (ref. 21) are also presented in figure 19. The solid lines denote inputs $\gamma_{eff}$ and $M_{eff}$, the broken lines denote inputs $\gamma_{E,5}$ and $M_5$, and the dashed lines denote inputs $\gamma_{E,5s}$ and $M_5$. Only a single line is shown for helium due to the ideal-helium behavior $(\gamma_{E,5} = \gamma_{E,5s} = \gamma_{eff}$ and $M_5 = M_{eff})$. For helium, the calculated detachment distance underpredicts the measured detachment distance. This trend was also observed in reference 31 for a flat-faced cylinder at a Mach number of 20 in helium. The difference between measured and calculated detachment distance for helium may be due to only one strip being used in reference 21. As noted in reference 32, employing a two-strip integral method (accuracy increases with number of strips) results in a greater shock detachment distance for a flat-faced cylinder than given by the one-strip method. For air and $CO_2$, agreement between measured and calculated detachment distance improves when $\gamma_{E,5s}$ is used as input as compared with $\gamma_{E,5}$ input. Best agreement between measured and predicted detachment distance for these two test gases is observed for inputs $\gamma_{eff}$ and $M_{eff}$. This supports the proposal (see, for example, refs. 1, 5, 8, and 30) that flow-field calculations for blunt bodies at hypersonic speeds where real-gas effects are significant can be greatly simplified by use of ideal-gas relations with an appropriate value of ratio of specific heats. This ratio of specific heats yields the correct normal shock density ratio, which is the controlling factor governing shock detachment distance at hypersonic flow conditions. Figure 19 clearly illustrates the sensitivity of calculated $\Delta/r_b$ to ratio of specific heats. For example, an 11 percent decrease in this ratio $(\gamma_{E,5}$ to $\gamma_{eff})$ for air yields a 24 percent decrease in calculated $\Delta/r_b$, whereas, only a 7 percent decrease for $CO_2$ also results in a 24 percent decrease in $\Delta/r_b$. (The value of $M_{eff}$ for air is 13 percent greater than $M_5$, and $M_{eff}$ for $CO_2$ is 8 percent greater than $M_5$. However, for these flow conditions, the inviscid forebody flow should be relatively insensitive to Mach number.)

Shock shapes for sphere.- Measured shock shapes for a sphere having a diameter $d_n$ of 6.35 cm are shown in figure 20 for helium, air, and $CO_2$. The expected decrease

in measured shock detachment distance with increasing $\epsilon$ is observed. Measured $\Delta/r_n$ decreases by a factor of approximately 5 for the fivefold increase in $\epsilon$. This decrease in $\Delta/r_n$ is twice that observed for the flat-faced cylinder (fig. 19) for the same increase in $\epsilon$. Hence, the effect of increasing $\epsilon$ on shock standoff distance diminishes as the body shape becomes more blunt (sphere to flat-faced cylinder). Also shown in figure 20 are calculated shock shapes (refs. 15 and 22) for a sphere. Basic inputs to the programs of references 15 and 22 were $\gamma_{eff}$ and $M_{eff}$. Shock detachment distances in the stagnation region predicted from these two programs are within 4 percent for each test gas. For uniform free-stream flow (that is, $\lambda$ equal to zero for predictions from ref. 15 illustrated in fig. 20), the detachment distances away from the stagnation region predicted by these two programs are in good agreement for helium (fig. 20(a)). The agreement for air and $CO_2$ (figs. 20(b) and 20(c)) is poorer, with the detachment distance predicted from reference 22 exceeding that predicted from reference 15. Measured and predicted detachment distances for helium are in good agreement for $r/r_n$ less than approximately 0.8; for further increase in $r/r_n$, the measured detachment distance exceeds prediction. For air and $CO_2$, measured detachment distance exceeds prediction, with the difference between measured and predicted detachment distance increasing with distance $(r/r_n)$ from the stagnation region.

Effect of flow nonuniformity.- Nonuniform free-stream flow properties can have an appreciable effect on shock shape (refs. 15 and 16). In reference 15, the effect of a parabolic variation of $U_5$ with perpendicular distance from the model axis was examined. The expression for the velocity was written in the form

$$U_5\left(\frac{r}{r_b}\right) = U_5\left(\frac{r}{r_b} = 0\right)\left[1 - \lambda\left(\frac{r}{r_b}\right)^2\right] \tag{4}$$

where $U_5(r/r_b = 0)$ is the value of $U_5$ on the expansion-tube centerline and $\lambda$ is the percent deviation of $U_5$ at a distance $r$ equal to $r_b$ (or $r_n$ for a sphere) from the axis from $U_5(r/r_b = 0)$. Free-stream static pressure and total enthalpy are assumed to be constant. In general, the effect of flow nonuniformity is to move the shock detachment distance in the stagnation region slightly closer to the body and farther from the body in the transonic and supersonic regions (refs. 15 and 16). For the configurations tested in this study, the flat-faced cylinder is least sensitive to flow nonuniformity and the sphere most sensitive; hence, the sphere results are used to examine whether flow nonuniformity exists for the present test gases.

Predicted shock shapes (ref. 15) with the effect of flow nonuniformity on the shock shape of a sphere taken into account are shown in figure 20. Comparison of these predicted shock shapes with the measured shock shapes shows that values of $\lambda$ equal to 0.01, 0.06, and 0.07 in the program of reference 15 provide good agreement for helium,

air, and $CO_2$ test gas, respectively. This comparison indicates that the helium flow may be slightly nonuniform, and the air and $CO_2$ flows are probably nonuniform. (The uncertainty associated with the prediction of the shock detachment distance away from the stagnation region for a sphere, using perfect gas relations and $M_{eff}$ and $\gamma_{eff}$ inputs, prohibits a definite conclusion concerning flow nonuniformity.)

Shock shapes for spherically blunted cones.- Measured and predicted (ref. 21) shock detachment distances in helium are compared in figure 21 for four spherically blunted cones $(r_n/r_b = 0.5, \ r_b = 2.54 \text{ cm})$ with semiapex angles of $80^o$, $70^o$, $60^o$, and $50^o$. Calculated values of $\Delta/r_b$ are within 10 percent of measured values for all cone models. The method of reference 21 underpredicts the shock detachment distance for $\theta$ equal to $80^o$ to approximately the same extent it underpredicted that for the flat-faced cylinder. However, as $\theta$ decreases from $80^o$, the degree of underprediction diminishes and for a value of $\theta$ equal to $50^o$, measured detachment distance is less than calculated. Since the measured and predicted detachment distances agree to within 10 percent (that is, within the experimental accuracy and the uncertainty in calculated detachment distance), no conclusion concerning this underprediction or overprediction of reference 21 is drawn.

Shock shapes for these same spherically blunted cones are shown in figure 22 for air and figure 23 for $CO_2$. At the lower values of $\theta$ for air and $CO_2$, combinations of inputs $M_{eff}$, $\gamma_{eff}$, $r_n/r_b$, and $\theta$ to the program of reference 21 resulted in the sonic point for a complete, smooth sphere occurring at the sphere-cone junction. Such a condition results in nonconvergence. For this case, predicted shock shapes were obtained from the program of reference 15 or 22. Agreement between measured and predicted detachment distance for air (fig. 22) becomes poorer as $\theta$ decreases from $70^o$, with the measured detachment distance exceeding predicted values. Measured and predicted detachment distance for $CO_2$ (fig. 23) is observed to be in good agreement for a value of $\theta$ of $80^o$, but measured detachment distance exceeds prediction for $\theta$ less than $80^o$.

Effect of cone semiapex angle.- Measured $\Delta/r_b$ for the cone and flat-faced cylinder models is plotted as a function of cone semiapex angle $\theta$ in figure 24. Also shown in figure 24 are predictions from the methods of references 15, 21, and 22 for these models and the present test conditions (basic inputs $M_{eff}$ and $\gamma_{eff}$), and asymptotic sphere predictions from reference 15. Helium results at Mach 8 and 20 (ref. 31) for sharp cones, and helium results at Mach 22 (ref. 33) as well as air results at Mach 3 (ref. 34) for spherically blunted cones are shown. The shock standoff distance for the present helium results, the helium results of reference 31, and the ideal-air results of reference 34 are observed to decrease almost linearly with decreasing cone semiapex angle from $90^o$ (flat-faced cylinder) to $50^o$. Such linear behavior for ideal-gas flows

leads to the correlations presented in reference 34. However, measured and predicted $\Delta/r_b$ decrease monotonically with decreasing $\theta$ from $90^o$ to $60^o$ for real air and from $90^o$ to $70^o$ for real $CO_2$, and remain essentially constant for further decrease in $\theta$. These trends for the three test gases are expected since the sonic point on the model surface moves off the corner and along the cone section onto the spherical section as the cone semiapex angle decreases. The semiapex angle for which this departure of the sonic point from the model corner occurs increases as the density ratio increases. Hence, the ratio $\Delta/r_b$ for $r_n/r_b$ equal to a constant will approach the (constant) value for a sphere most readily for $CO_2$ in thermochemical equilibrium and least readily for helium as $\theta$ decreases. As for the sphere, percent variation in measured $\Delta/r_b$ with $\epsilon$ for each cone model exceeds that for the flat-faced cylinder.

The shock detachment distance $\Delta^*/r_b$ at the corner of the model $\left(r/r_b = 1\right)$ is shown in figure 25 as a function of cone semiapex angle. (The quantity $\Delta^*$ represents the shock detachment distance at the corner as measured parallel to the free-stream flow direction.) Also shown in this figure are the helium results of reference 31. Measured and predicted helium results show that $\Delta^*/r_b$ is essentially independent of $\theta$ for the range of $\theta$ and $r_n/r_b$ examined. For air and $CO_2$, measured $\Delta^*/r_b$ is nearly constant for $70^o \leqq \theta \leqq 90^o$, and decreases somewhat with further decrease in $\theta$. This decrease in $\Delta^*/r_b$ with decreasing $\theta$, as the value of $\theta$ at which the surface sonic point moves off the corner is approached, is predicted by references 21 and 22.

Effect of model diameter.- Shock detachment distance for four flat-faced cylinders of various diameters is shown in figure 26 for helium, air, and $CO_2$ test gases. The diameter $d_b$ was varied from 1.91 to 7.62 cm. Some data scatter is evident for the helium results (fig. 26(a)), although the measured $\Delta/r_b$ is within 10 percent for all $d_b$. At the corner $\left(r/r_b = 1\right)$, the detachment distance for the smallest diameter is approximately 15 percent greater than the other three diameters. Shock detachment distances for the four diameters in air (fig. 26(b)) and $CO_2$ (fig. 26(c)) are in relatively good agreement. Thus, no appreciable effect of model diameter on shock detachment distance is observed for the flat-faced cylinder models for these test gases. It is interesting to note that the smallest diameter model occupied approximately 6 percent of the cross-sectional test core area (as determined from pitot-pressure surveys), whereas the largest diameter model occupied the entire test core. However, no flow blockage phenomena were observed for these flat-faced cylinder models which were tested in an open jet test section.

In figure 27, the shock detachment distance for five sphere models of various diameters is shown for air and $CO_2$ test gases. (Helium results are not presented in fig. 27 due to the poorer shock resolution on the schlieren photographs; see the section "Data Reduction and Uncertainty.") The sphere diameter $d_n$ was varied from 1.27 to 7.62 cm.

The shock detachment distance is observed to increase as the sphere diameter decreases for both test gases. Shock shapes are essentially the same (in view of the experimental uncertainty in measured shock detachment distance) over the range of sphere diameters tested for air and $CO_2$. No flow blockage phenomena were observed for these sphere models.

Measured $\Delta/r_n$ for spheres having diameters from 1.27 to 7.62 cm and measured $\Delta/r_b$ for flat-faced cylinders having diameters from 1.91 to 7.62 cm are shown as a function of model diameter $d_n$ or $d_b$ in figure 28. The barred symbols denote a $\pm 10$ percent uncertainty in measured $\Delta/r_n$ or $\Delta/r_b$; open symbols denote sphere models and shaded symbols denote flat-faced cylinder models. Also shown in figure 28 are predictions from the methods of reference 15 for a sphere and reference 21 for a flat-faced cylinder (basic inputs are $M_{eff}$ and $\gamma_{eff}$). The measured $\Delta/r_b$ for the flat-faced cylinders is essentially constant with $d_b$ and in good agreement with prediction. Likewise, the helium sphere results show no effect of $d_n$ on measured $\Delta/r_n$. However, sphere models with air and $CO_2$ test gases indicate a definite effect of $d_n$, with measured $\Delta/r_n$ increasing with decreasing $d_n$.

Effect of viscosity.- One possible contributor to the variation in measured $\Delta/r_n$ with sphere diameter is viscous effects. At sufficiently low Reynolds numbers, the shock and boundary-layer thicknesses are no longer negligible compared with the shock detachment distance, and the shock detachment distance becomes a function of Reynolds number as well as density ratio. In this regime, $\Delta/r_n$ increases with decreasing Reynolds number (ref. 35). This trend is illustrated by the argon results of reference 35 reproduced in figure 29, where $\Delta/r_n$ or $\Delta/r_b$ is plotted as a function of Reynolds number based on static conditions immediately behind the normal portion of the bow shock (region (5s)) and on body diameter $N_{Re,5s,d_b}$. Since (1) the present values of $N_{Re,5s,d_b}$ are in excess of $10^3$ (ref. 35), (2) the present helium sphere results and the flat-faced cylinder results are independent of Reynolds number for $N_{Re,5s,d_b}$ greater than $2 \times 10^3$, and (3) the present large wall cooling ($T_w/T_{5t}$ equal to approximately 0.06, 0.05, and 0.08 for helium, air, and $CO_2$) tends to decrease the boundary-layer displacement thickness (ref. 36), measured $\Delta/r_n$ should be independent of Reynolds number (viscous effects).

Effect of flow nonequilibrium.- A second possible explanation is the departure of air and $CO_2$ flow in the shock layer from thermochemical equilibrium. The value of $\Delta/r_n$ for inviscid nonequilibrium flow in the shock layer will be greater than that for equilibrium flow (ref. 36). Before attributing these larger values of $\Delta/r_n$ to nonequilibrium flow in the shock layer, the effect of free-stream thermochemistry on $\Delta/r_n$ will be considered. Departure of free-stream nozzle airflow from equilibrium was observed in reference 36 to result in relatively small changes in $\Delta/r_b$. The effect of flow chemistry is examined for the expansion tube by first considering the normal shock

density ratio and free-stream Mach number for air as a function of free-stream velocity. (See fig. 30.) These results, which correspond to the predicted flow conditions of figure 14, were obtained from reference 17 and include limiting cases of no shock reflection and a totally reflected shock at the secondary diaphragm. Three limiting cases for the expansion process and conditions behind the bow shock of the model considered are (1) equilibrium expansion—equilibrium postshock, (2) frozen expansion—equilibrium postshock, and (3) frozen expansion—frozen postshock. The effect of flow attenuation is illustrated for the case of an equilibrium expansion and equilibrium postshock. For both the case of no shock reflection (fig. 30(a)) and a totally reflected shock (fig. 30(b)), the difference in density ratio $\epsilon$ at the present value of $U_5$ (5.32 km/sec) between case (1) and case (2) is less than 1 percent. For this $U_5$, the density ratio for case (3) is approximately half that for case (1) or (2). The results of figure 30 were used to determine corresponding values of $M_{eff}$ and $\gamma_{eff}$ (for given values of $U_5$) for the three cases under consideration. These quantities were used as input to the program of reference 21 to obtain corresponding values of $\Delta/r_b$ for a flat-faced cylinder, the results of which are shown in figure 31. Also shown in figure 31 are measured values of $\Delta/r_b$ for air. Departure of the free-stream air from equilibrium flow to frozen flow produces only a small effect on calculated $\Delta/r_b$ (as deduced in ref. 36), provided the postshock region remains in equilibrium. This is true for both the case of no shock reflection (fig. 31(a)) and a totally reflected shock (fig. 31(b)). Frozen free-stream and postshock flow (case (3)) results in $\Delta/r_b$ for a flat-faced cylinder being approximately 30 percent greater than for case (1) or (2) for both no shock reflection and a totally reflected shock. Measured $\Delta/r_b$ is in good agreement with cases (1) and (2) for both shock reflection cases. This is in agreement with figure 28, in that the postshock region appears to be close to equilibrium for the flat-faced cylinders. However, no conclusion may be drawn from figure 31 concerning the thermochemical state of the free-stream airflow, due to the small difference in calculated $\Delta/r_b$ between equilibrium and frozen free-stream flow. Inclusion of flow attenuation produces a small decrease in predicted $\Delta/r_b$. This decrease is not sufficient to alter any conclusions drawn from figure 31 concerning the thermochemical state of the flow.

In contrast to the air results of figure 30, similar results for $CO_2$ (fig. 32) show $\epsilon$ for an equilibrium expansion—equilibrium postshock (case (1)) to be significantly greater than for a frozen expansion-equilibrium postshock (case (2)) at the value of $U_5$ of interest (4.95 km/sec). The results of figure 32 for $CO_2$ were used to generate inputs to the method of reference 21. The resulting predicted values of $\Delta/r_b$ for a flat-faced cylinder are shown in figure 33. Also shown in figure 33 are measured values of $\Delta/r_b$ for $CO_2$. For no shock reflection (fig. 33(a)) and a totally reflected shock (fig. 33(b)), the measured $\Delta/r_b$ is observed to be in good agreement with case (1) (equilibrium expansion—equilibrium postshock). Hence, the free-stream flow for $CO_2$ appears to be

close to equilibrium, as does the postshock flow region. Unlike air, greater values of $\Delta/r_b$ than expected could imply a frozen expansion, but the postshock flow may or may not be in equilibrium for $CO_2$ test gas. Again, the effect of flow attenuation on predicted $\Delta/r_b$ is small.

Scaling law parameter.- The spherically blunted cone results of figure 24 and the data of figure 28 (excluding the helium results) are replotted in figure 34, where the measured shock standoff distance nondimensionalized by predicted shock standoff distance $\Delta_m/\Delta_c$ (ref. 15 for sphere predictions, ref. 21 for flat-faced cylinder predictions, and refs. 15, 21, and 22 for spherically blunted cone predictions) is shown as a function of the binary scaling law parameter (refs. 30 and 37). This parameter is the product of free-stream density and a characteristic length and has been observed to correlate hypersonic, nonequilibrium flows for a given free-stream velocity, provided two-body collisions dominate the chemical reaction process. The characteristic length used was the calculated shock standoff distance $\Delta_c$. Open symbols denote sphere results, shaded symbols denote flat-faced cylinder results, and half-shaded symbols denote spherically blunted cone results. The sphere and cone results for air and $CO_2$ follow the same trend, with $\Delta_m/\Delta_c$ approaching unity as $\rho_5\Delta_c$ increases. Based on the previous discussion, this increase in $\Delta_m/\Delta_c$ with decreasing $\rho_5\Delta_c$ is believed due to departure from equilibrium in the postshock flow region for both test gases, since viscous effects are negligible. It should be noted that applying the binary scaling law to the air results of reference 38 implies the existence of chemical nonequilibrium in the postshock region for the present sphere and cone results in air. From reference 30, vibrational equilibrium in the postshock region is expected for the present air results. The results of figure 34 indicate that to avoid nonequilibrium flow in the postshock region at the present air and $CO_2$ flow conditions, the parameter $\rho_5\Delta_c$ should be greater than approximately $2 \times 10^{-5}$ kg/m$^2$ for air and $1 \times 10^{-5}$ kg/m$^2$ for $CO_2$.

Correlation of shock standoff distance.- Predicted values of $\Delta/r_n$ for spheres at hypersonic speeds in various equilibrium gases have been observed to correlate with the inverse of normal shock density ratio over a wide range of density ratios (ref. 9). Results for the larger diameter sphere models are shown in figure 35, where $\Delta/r_n$ is plotted as a function of $\epsilon^{-1}$. Also shown in figure 35 are predictions presented in references 1, 7, and 9, predictions of reference 15 for a sphere, and measured values of $\Delta/r_n$ for spheres in $CF_4$ flow. (Predictions from refs. 1, 7, and 9 are obtained from simple expressions. For convenience, these expressions are $\frac{\Delta}{r_n} = \frac{2}{3(\epsilon - 1)}$ for ref. 1, $\frac{\Delta}{r_n} = 0.52(\epsilon - 1)^{-0.861}$ for ref. 7, and $\frac{\Delta}{r_n} = \frac{0.78}{\epsilon}$ for ref. 9.) The $CF_4$ data were obtained by Raymond E. Midden in the Langley hypersonic $CF_4$ tunnel. Sphere diameters were 2.54 and 7.62 cm, calculated $CF_4$ free-stream Mach number was 6.1, and normal shock density ratio was 12. No significant effect of diameter on measured val-

ues of $\Delta/r_n$ was observed for these $CF_4$ results. As expected, the helium results are in good agreement with the predicted results and the $CF_4$ results are in relatively good agreement with the prediction. The air and $CO_2$ results are approximately 15 to 25 percent greater than prediction, due to the probable existence of nonequilibrium flow within the shock layer. The present sphere results (acknowledging that some departure from equilibrium may exist for air and $CO_2$) are amenable to a straight line fit which yields the expression

$$\frac{\Delta}{r_n} = \frac{0.70}{\epsilon^{0.88}} \tag{5}$$

The present shock standoff distances for the flat-faced cylinder are also presented in figure 35. These results are predicted to within a few percent over the range $3.7 \leqq \epsilon \leqq 18.8$ by the expression

$$\frac{\Delta}{r_b} = \frac{1.32}{\epsilon^{0.56}} \tag{6}$$

The simple relation $\left(\frac{\Delta}{r_b} = \frac{1.03}{\sqrt{\epsilon - 1}}\right)$ derived in reference 1 for a flat-faced cylinder is observed to yield values of $\Delta/r_b$ within the experimental uncertainty (denoted by barred symbols of fig. 35) of the present measured values.

## CONCLUDING REMARKS

A preliminary experimental investigation to determine flow characteristics in the Langley 6-inch expansion tube with helium, air, and $CO_2$ test gases has been performed. Vertical pitot-pressure profiles at the test section showed the existence of a test core for all test gases, with the diameter of this core being approximately half the tube diameter. Test repeatability was good. Free-stream velocities from 5 to 7 km/sec were generated at hypersonic conditions, resulting in normal shock density ratios from approximately 4 to 19. Comparison of predicted expansion-tube performance and measured flow quantities for helium indicated the test gas was processed by a totally reflected shock from the secondary diaphragm before undergoing an unsteady expansion to the test section. A similar comparison for air and $CO_2$ indicated the flow expansion was probably close to thermochemical equilibrium. For these two gases, the incident shock velocity in the acceleration section, hence free-stream velocity, was observed to decrease in traversing the acceleration section. Inclusion of this attenuation in the prediction was found to improve agreement with experiment. For helium test gas, the incident shock velocity was essentially constant with distance along the acceleration section.

Measured shock detachment distances on a flat-faced cylinder model in helium, air, and $CO_2$ were in good agreement with ideal-gas predictions, provided the normal shock density ratio was accounted for by using an effective ratio of specific heats. Measured and predicted normalized shock standoff distance for the spherically blunted cone models decreased monotonically with cone semiapex angle towards the sphere value as expected. The normalized standoff distance at the corner of the blunted cone models was essentially independent of semiapex angle between $50^{\circ}$ and $90^{\circ}$ for helium and between $70^{\circ}$ and $90^{\circ}$ for air and $CO_2$. Variation of flat-faced cylinder diameter by a factor of 4 did not produce a significant effect on shock shape or normalized standoff distance, even for diameters as large as the test core diameter. A pronounced effect of diameter was observed for sphere models in air and $CO_2$, with normalized standoff distance increasing with decreasing diameter. Since viscous effects are negligible for the present conditions, this variation is attributed to nonequilibrium flow in the shock layer. Differences between measured and predicted shock detachment distance for a sphere worsened with increasing distance from the stagnation region, indicating the possible existence of free-stream flow nonuniformity for all three test gases. For the present air and $CO_2$ test conditions, the product of free-stream density and shock standoff distance should be greater than approximately $10^{-5}$ kg/m2 to avoid nonequilibrium effects in the shock layer. Free-stream nonequilibrium in expansion-tube flow was shown to have a small effect on shock standoff distance for air, but an appreciable effect for $CO_2$. Comparison of measured standoff distance for a flat-faced cylinder with predicted values, obtained by using a program for predicting expansion-tube flow conditions in conjunction with a program for predicting flow past blunt bodies, indicated the $CO_2$ free-stream flow was in equilibrium. A simple expression was obtained that predicts the shock standoff distance for a flat-faced cylinder over the present range of density ratio.

Langley Research Center,
National Aeronautics and Space Administration,
Hampton, Va., November 29, 1974.

## REFERENCES


1. Serbin, Hyman: The High Speed Flow of Gas Around Blunt Bodies. Aeronaut. Quart., vol. IX, pt. 4, Nov. 1958, pp. 313-330.

2. Van Dyke, Milton D.; and Gordon, Helen D.: Supersonic Flow Past a Family of Blunt Axisymmetric Bodies. NASA TR R-1, 1959.

3. Hayes, Wallace D.; and Probstein, Ronald F.: Hypersonic Flow Theory. Academic Press, Inc., 1959.

4. Ridyard, Herbert W.; and Storer, Elsie M.: Stagnation-Point Shock Detachment of Blunt Bodies in Supersonic Flow. J. Aerosp. Sci., vol. 29, no. 6, June 1962, pp. 751-752.

5. Choudhury, P. Roy: Shock-Standoff Distance for Spherical Bodies at High Mach Numbers. J. Aerosp. Sci., vol. 29, no. 6, June 1962, p. 745.

6. Seiff, Alvin: Recent Information on Hypersonic Flow Fields. Proceedings of the NASA-University Conference on the Science and Technology of Space Exploration, Vol. 2, NASA SP-11, 1962, pp. 269-282. (Also available as NASA SP-24.)

7. Ambrosio, Alphonso; and Wortman, Andrzej: Stagnation-Point Shock-Detachment Distance for Flow Around Spheres and Cylinders in Air. J. Aerosp. Sci., vol. 29, no. 7, July 1962, p. 875.

8. Lomax, Harvard; and Inouye, Mamoru: Numerical Analysis of Flow Properties About Blunt Bodies Moving at Supersonic Speeds in an Equilibrium Gas. NASA TR R-204, 1964.

9. Inouye, Mamoru: Blunt Body Solutions for Spheres and Ellipsoids in Equilibrium Gas Mixtures. NASA TN D-2780, 1965.

10. Schwartz, R. N.; and Eckerman, J.: Shock Location in Front of a Sphere as a Measure of Real Gas Effects. J. Appl. Phys., vol. 27, no. 2, Feb. 1956, pp. 169-174.

11. Chapman, Dean R.: Some Possibilities of Using Gas Mixtures Other Than Air in Aerodynamic Research. NACA Rep. 1259, 1956. (Supersedes NACA TN 3226.)

12. Jones, Robert A.; and Hunt, James L. (With appendix A by James L. Hunt, Kathryn A. Smith, and Robert B. Reynolds, and appendix B by James L. Hunt and Lillian R. Boney): Use of Tetrafluoromethane To Simulate Real-Gas Effects on the Hypersonic Aerodynamics of Blunt Vehicles. NASA TR R-312, 1969.

13. Jones, Robert A.; and Hunt, James L.: Measured Pressure Distributions on Large-Angle Cones in Hypersonic Flows of Tetrafluoromethane, Air, and Helium. NASA TN D-7429, 1973.

14. Hunt, James L.; Jones, Robert A.; and Smith, Kathryn A.: Use of Hexafluoroethane To Simulate the Inviscid Real-Gas Effects on Blunt Entry Vehicles. NASA TN D-7701, 1974.

15. Barnwell, Richard W.: A Time-Dependent Method for Calculating Supersonic Blunt-Body Flow Fields With Sharp Corners and Embedded Shock Waves. NASA TN D-6031, 1970.

16. Patterson, Jerold L.; and Lewis, Arthur B.: An Investigation of Nonuniform Hypersonic Free-Stream Flows About Blunt Axisymmetric Bodies. AFFDL-TR-69-57, U.S. Air Force, Nov. 1969. (Available from DDC as AD 700 984.)

17. Miller, Charles G., III: A Program for Calculating Expansion-Tube Flow Quantities for Real-Gas Mixtures and Comparison With Experimental Results. NASA TN D-6830, 1972.

18. Miller, Charles G., III: Computer Program of Data Reduction Procedures for Facilities Using $CO_2$-$N_2$-$O_2$-Ar Equilibrium Real-Gas Mixtures. NASA TM X-2512, 1972.

19. Haggard, Kenneth V.: Free-Stream Temperature, Density, and Pressure Measurements in an Expansion Tube Flow. NASA TN D-7273, 1973.

20. Jones, Jim J.; and Moore, John A.: Exploratory Study of Performance of the Langley Pilot Model Expansion Tube With a Hydrogen Driver. NASA TN D-3421, 1966.

21. South, Jerry C., Jr.: Calculation of Axisymmetric Supersonic Flow Past Blunt Bodies With Sonic Corners, Including a Program Description and Listing. NASA TN D-4563, 1968.

22. Zoby, Ernest V.; and Graves, Randolph A., Jr.: A Computer Program for Calculating the Perfect Gas Inviscid Flow Field About Blunt Axisymmetric Bodies at an Angle of Attack of $0^{\circ}$. NASA TM X-2843, 1973.

23. Ames Research Staff: Equations, Tables, and Charts for Compressible Flow. NACA Rep. 1135, 1953. (Supersedes NACA TN 1428.)

24. Bailey, A. B.; and Boylan, D. E.: Some Experiments on Impact-Pressure Probes in a Low-Density, Hypervelocity Flow. AEDC-TN-61-161, U.S. Air Force, Dec. 1961.

25. Olstad, Walter B.; Kemper, Jane T.; and Bengtson, Roger D.: Equilibrium Normal-Shock and Stagnation-Point Properties of Helium for Incident-Shock Mach Numbers From 1 to 30. NASA TN D-4754, 1968.

26. Friesen, Wilfred J.: Use of Photoionization in Measuring Velocity Profile of Free-Stream Flow in Langley Pilot Model Expansion Tube. NASA TN D-4936, 1968.

27. Mirels, Harold: Test Time in Low-Pressure Shock Tubes. Phys. Fluids, vol. 6, no. 9, Sept. 1963, pp. 1201-1214.

28. Gaydon, A. G.; and Hurle, I. R.: The Shock Tube in High-Temperature Chemical Physics. Reinhold Pub. Corp., 1963.

29. Simpson, C. J. S. M.; Chandler, T. R. D.; and Bridgeman, K. B.: Measurement of the Opening Times of Diaghragms in a Shock Tube and the Effect of the Opening Process on Shock Trajectories. NPL Aero Rep. 1194, Brit. A.R.C., May 1966.

30. Hayes, Wallace D.; and Probstein, Ronald F.: Hypersonic Flow Theory. Volume I – Inviscid Flows. Second ed., Academic Press, Inc., 1966.

31. Stewart, David A.; and Inouye, Mamoru: Shock Shapes and Pressure Distributions for Large-Angle Pointed Cones in Helium at Mach Numbers of 8 and 20. NASA TN D-5343, 1969.

32. Inouye, Mamoru; and Marvin, Joseph G.: Comparison of Experimental and Theoretical Shock Shapes and Pressure Distributions on Flat-Faced Cylinders at Mach 10.5. NASA TN D-4397, 1968.

33. Johnson, Robert H.: The Cone-Sphere in Hypersonic Helium Above Mach 20. Aero/Space Eng., vol. 18, no. 2, Feb. 1959, pp. 30-34.

34. Ward, L. Christopher; and Pugh, Philip G.: Shock Standoff Distances of Blunt and Sharp Cones. AIAA J., vol. 6, no. 10, Oct. 1968, pp. 2018-2019.

35. Bailey, A. B.; and Sims, W. H.: Shock Detachment Distance for Blunt Bodies in Argon at Low Reynolds Number. AIAA J., vol. 1, no. 12, Dec. 1963, pp. 2867-2868.

36. Kuehn, Donald M.: Experimental and Theoretical Pressures on Blunt Cylinders for Equilibrium and Nonequilibrium Air at Hypersonic Speeds. NASA TN D-1979, 1963.

37. Gibson, Walter E.: Dissociation Scaling for Nonequilibrium Blunt Nose Flows. ARS J. (Tech. Notes), vol. 32, no. 2, Feb. 1962, pp. 285-287.

38. Marrone, Paul V.: Inviscid, Nonequilibrium Flow Behind Bow and Normal Shock Waves, Part I. General Analysis and Numerical Examples. Rep. No. QM-1626-A-12(I) (Contract No. DA-30-069-ORD-3443), Cornell Aeronaut. Lab., Inc., May 1963.

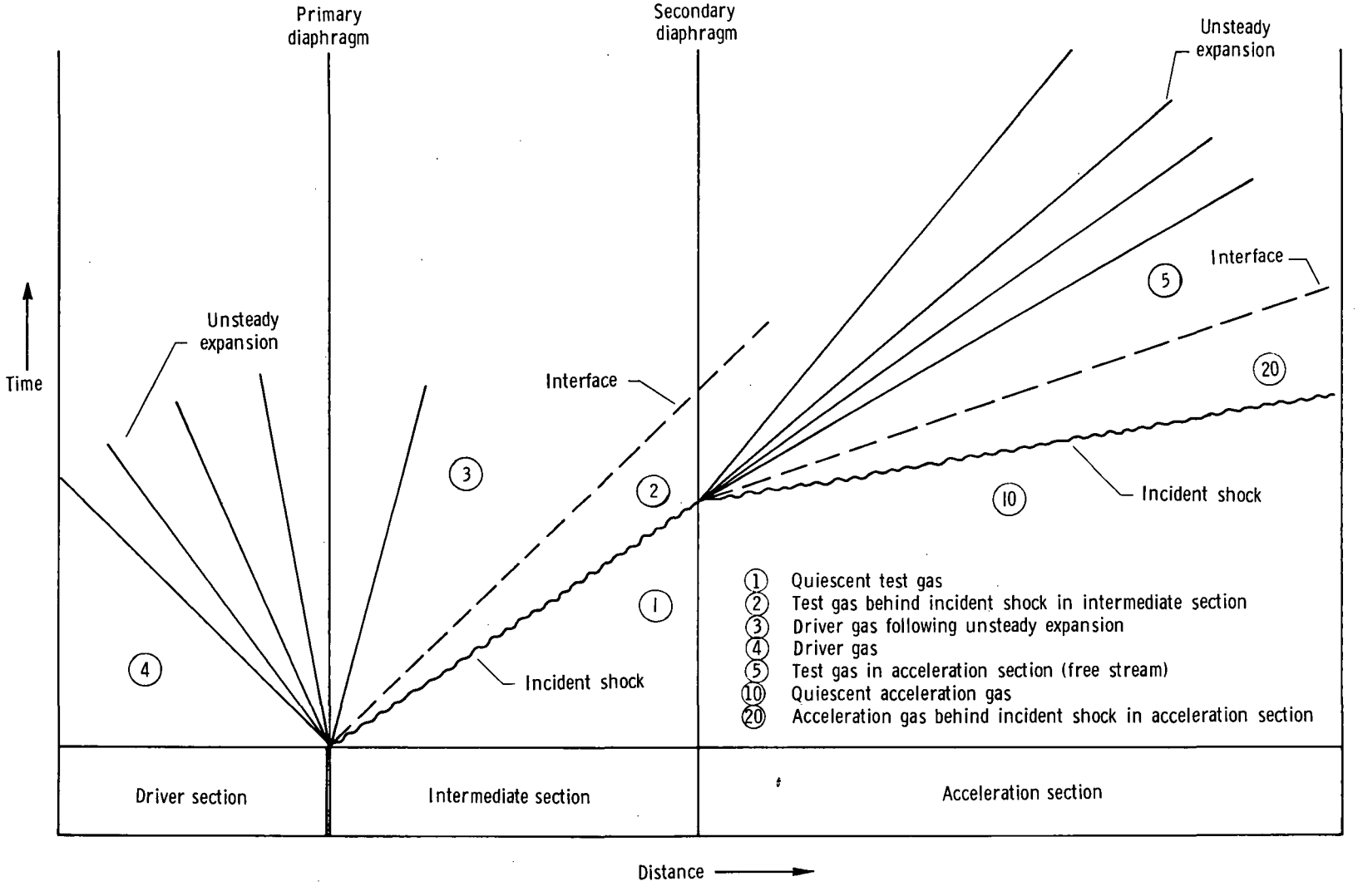


Figure 1.- Schematic diagram of expansion-tube flow sequence.

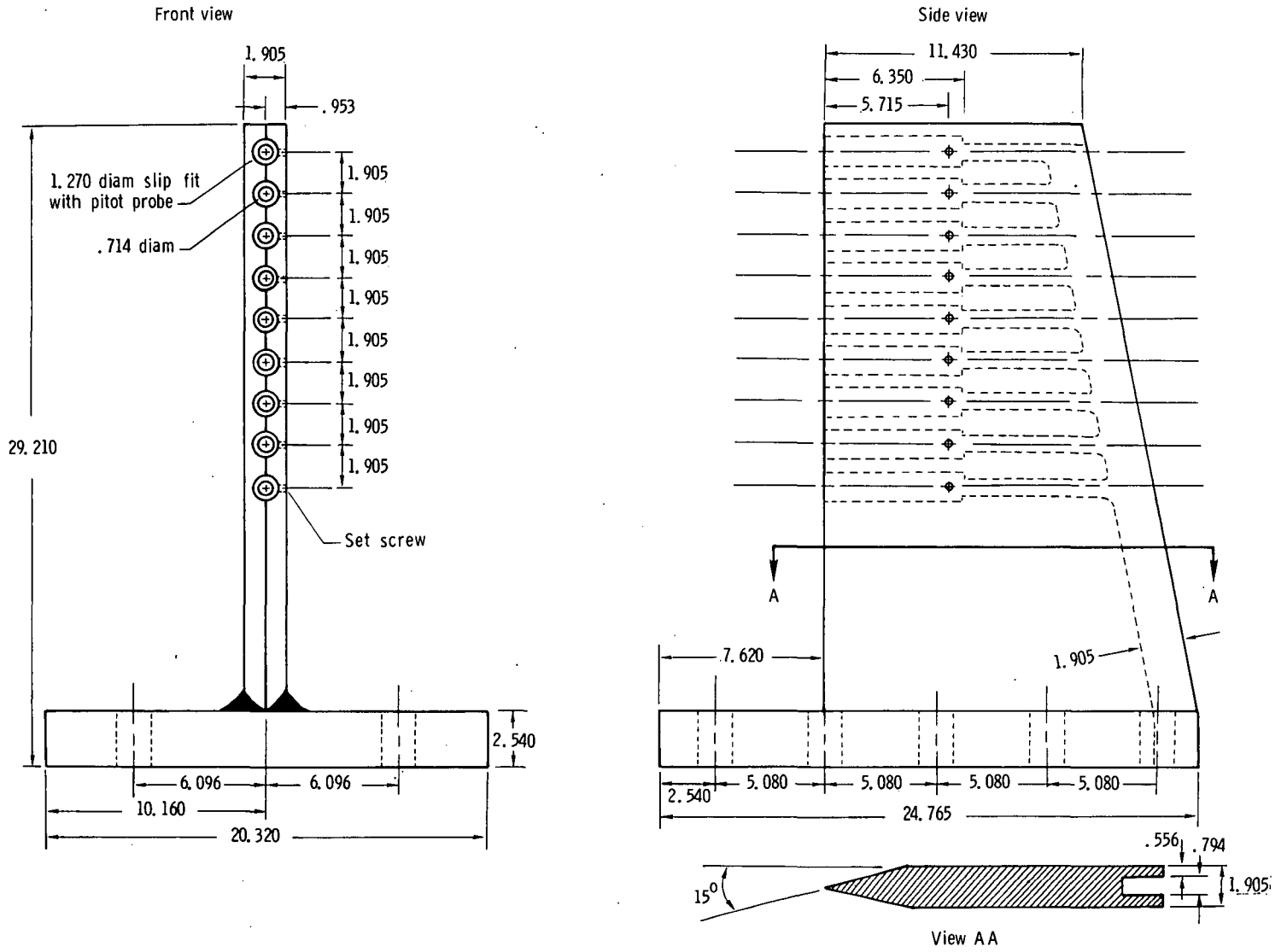


(a) Pitot-pressure survey rake.

Figure 2.- Pitot-pressure survey rake and probe. All dimensions in centimeters unless otherwise indicated.

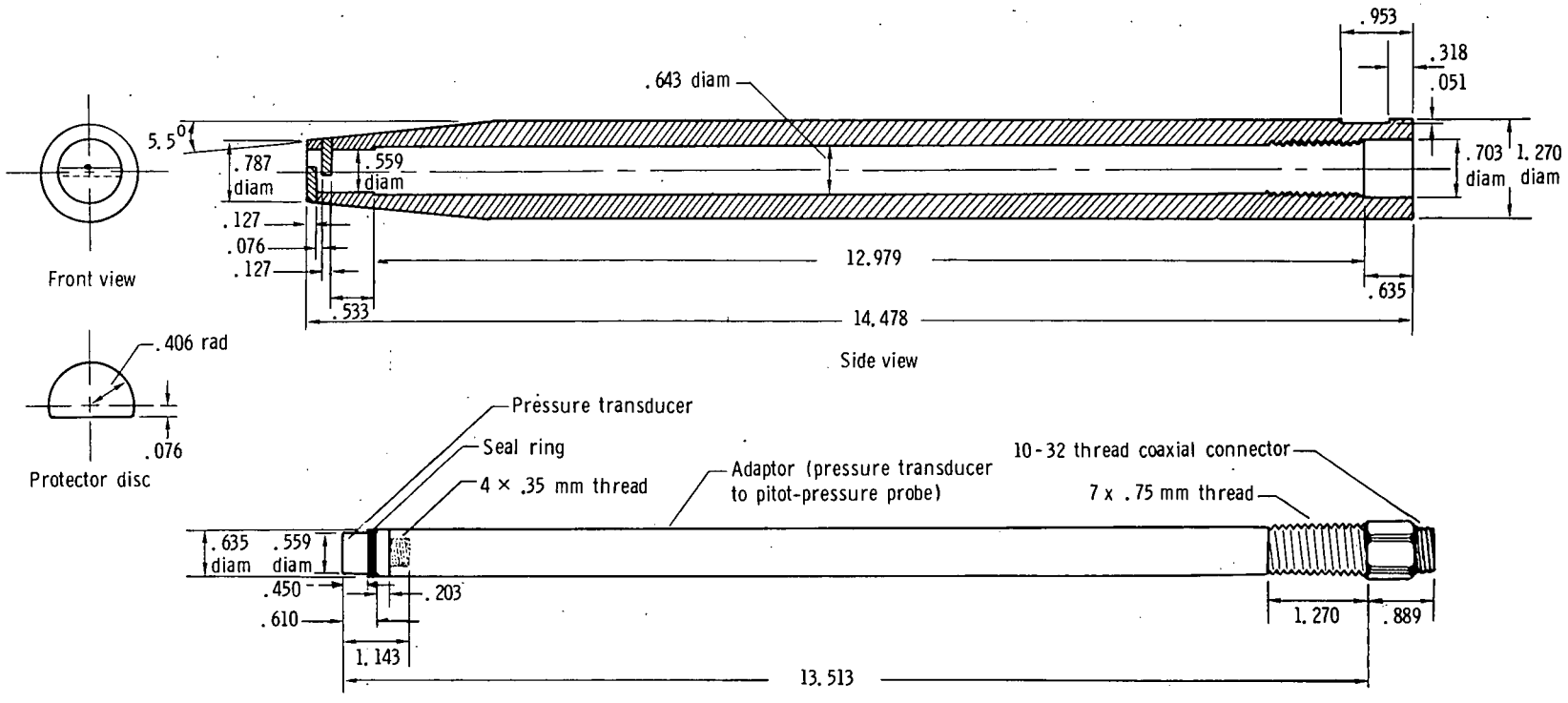


(b) Pitot-pressure probe.

Figure 2.- Concluded.

| Model | $d_n = 2r_n$, cm |
|---|---|
| 1 | 1.27 |
| 2 | 2.54 |
| 3 | 4.45 |
| 4 | 6.35 |
| 5 | 7.62 |

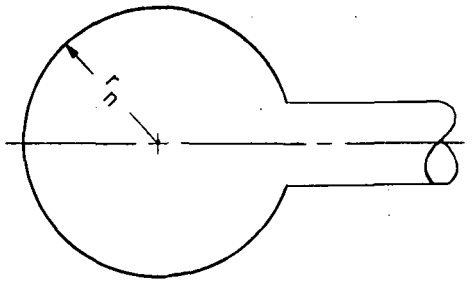


(a) Sphere models.

| Model | $d_b = 2r_b$, cm |
|---|---|
| 1 | 1.91 |
| 2 | 3.81 |
| 3 | 5.72 |
| 4 | 7.62 |

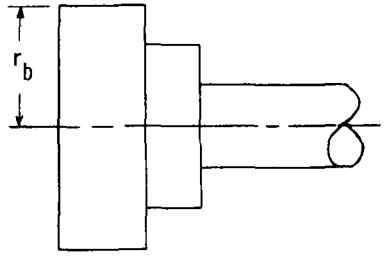


(b) Flat-faced cylinder models.

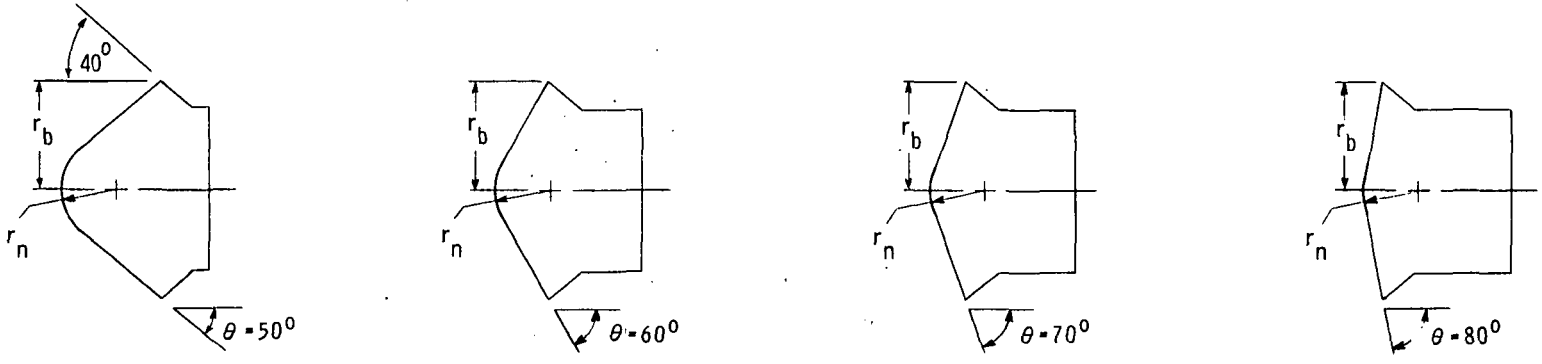


(c) Spherically blunted cone models; $r_b = 2.54$ cm, $r_n = 1.27$ cm.

Figure 3.- Models and support system used in present study.

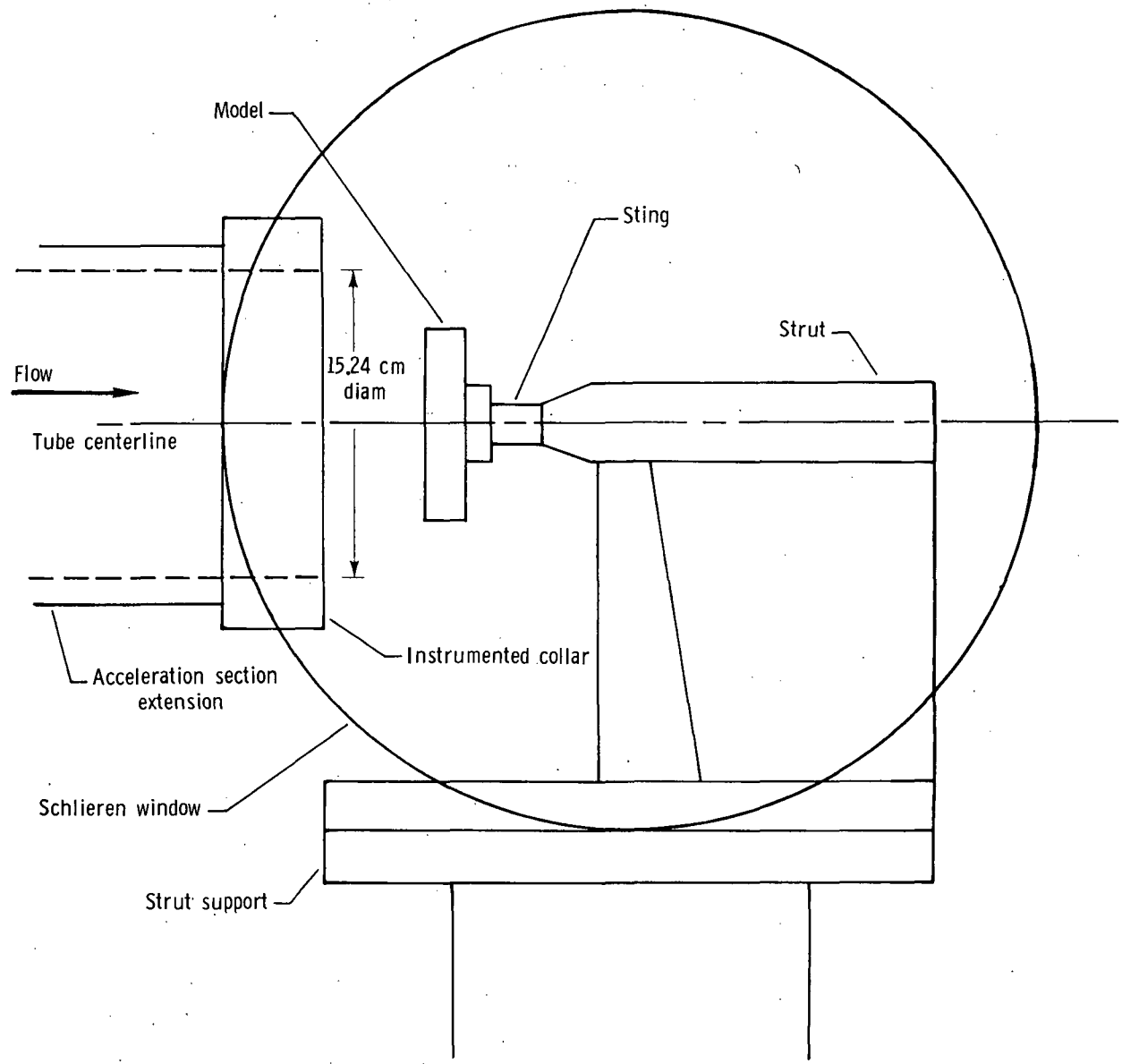


(d) Model support system.

Figure 3.- Concluded.

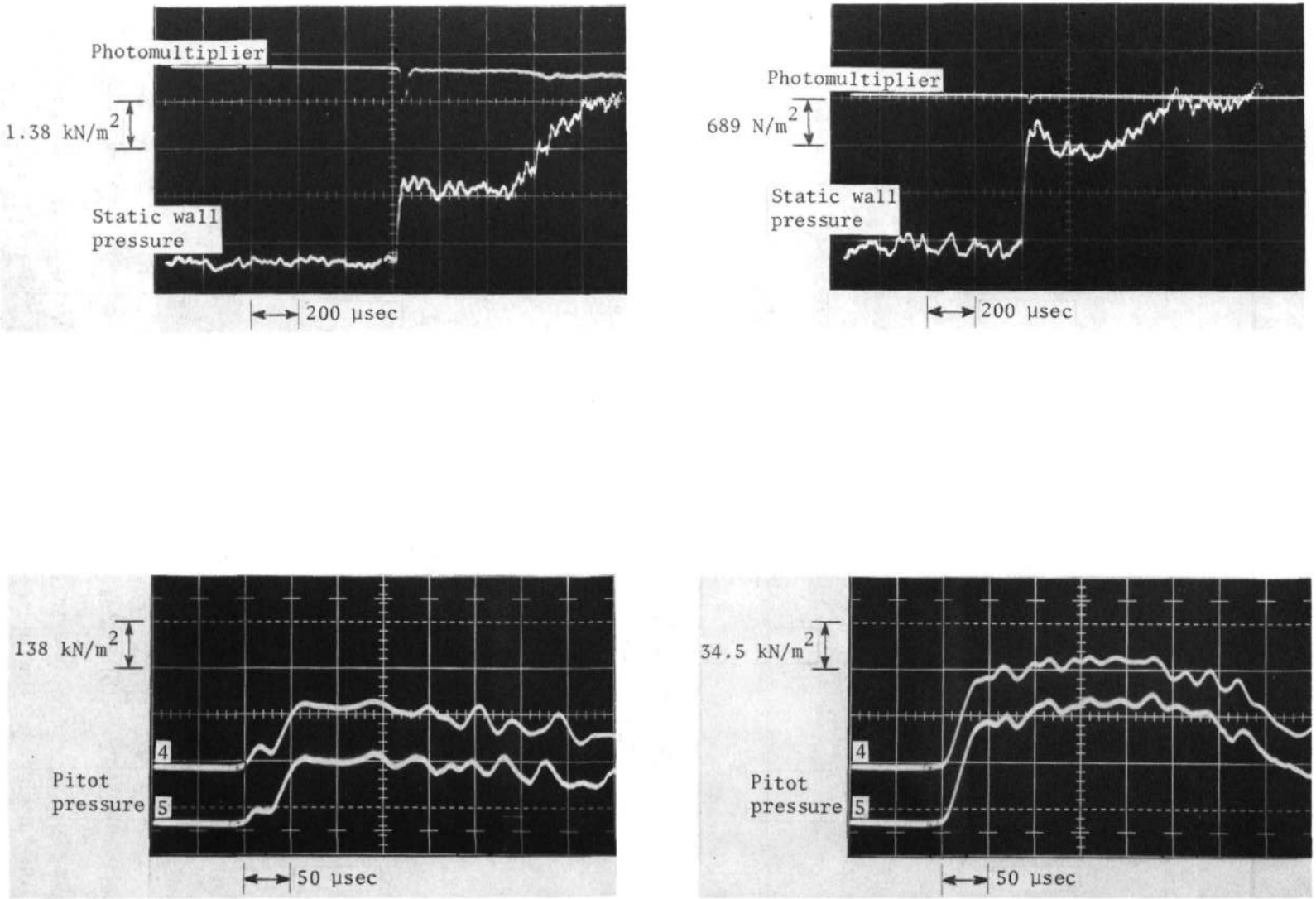


(a) Air.

(b) Helium.

Figure 4.- Representative oscilloscope traces of static wall pressure and pitot pressure for air and helium test gases.

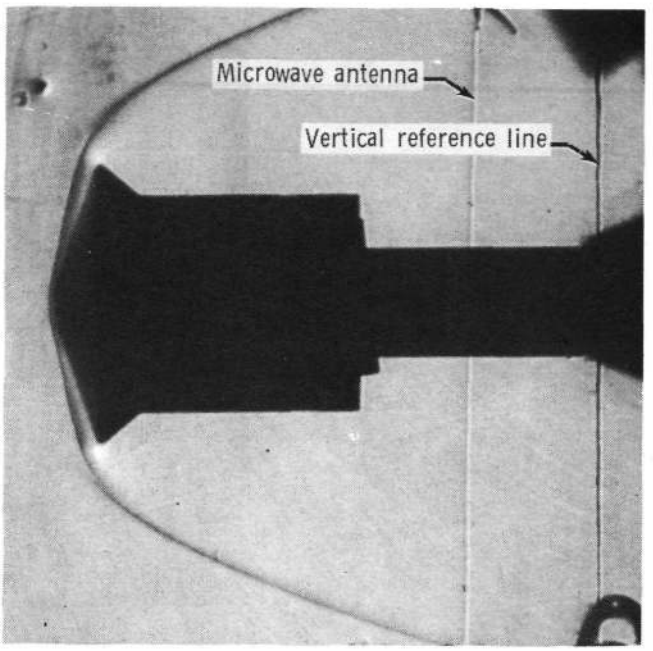


(a) Viking aeroshell model.

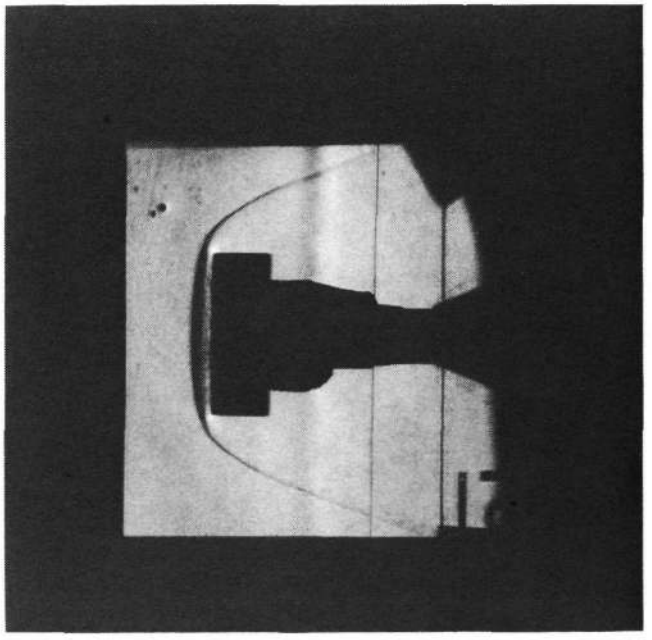

L-74-8540

(b) Flat-faced cylinder model.

Figure 5.- Schlieren photographs of shock shapes for Viking aeroshell and flat-faced cylinder models with $CO_2$ test gas and survey rake with air test gas.

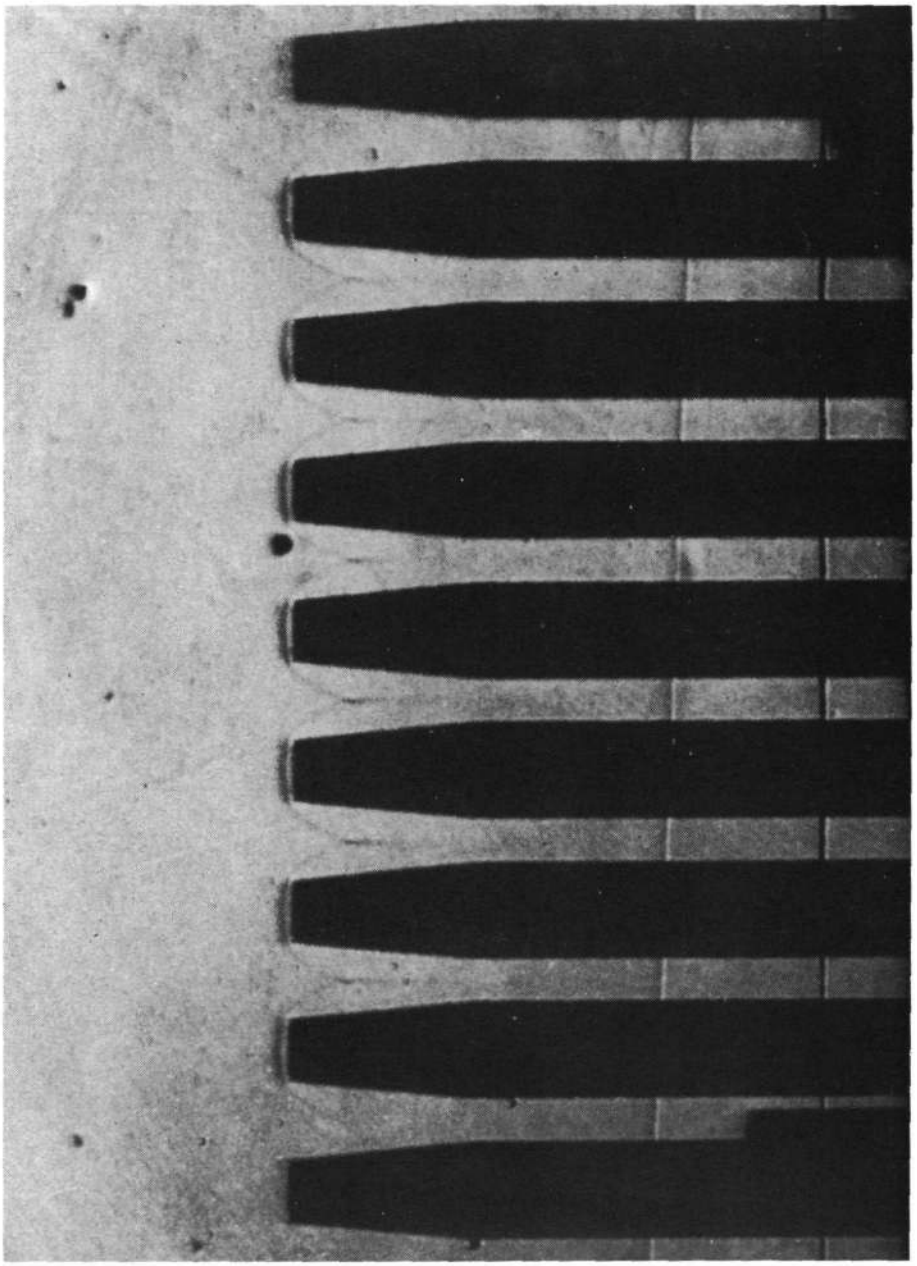

L-74-8541

(c) Pitot-pressure survey rake.

Figure 5.- Concluded.

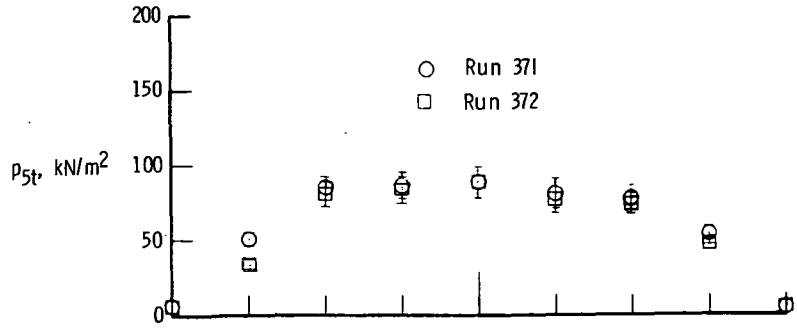


(a) Helium.

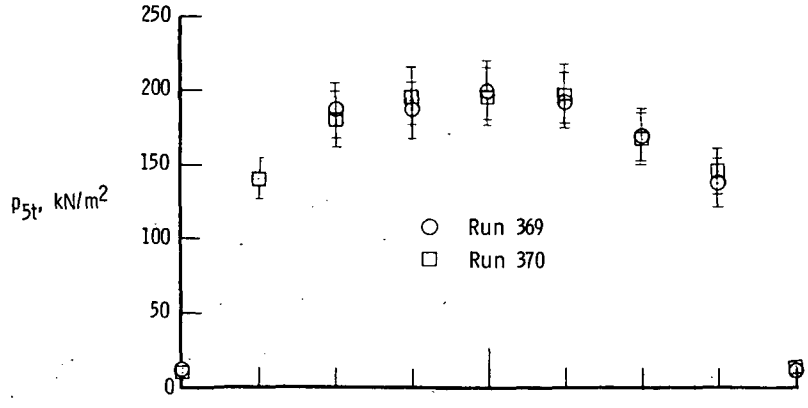


(b) Air.

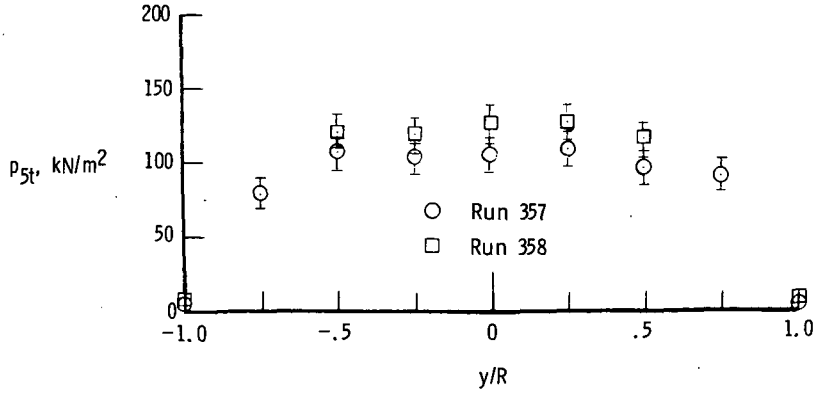


(c) $CO_2$.

Figure 6.- Vertical pitot-pressure profiles for helium, air, and $CO_2$ test gases. R = 7.62 cm.

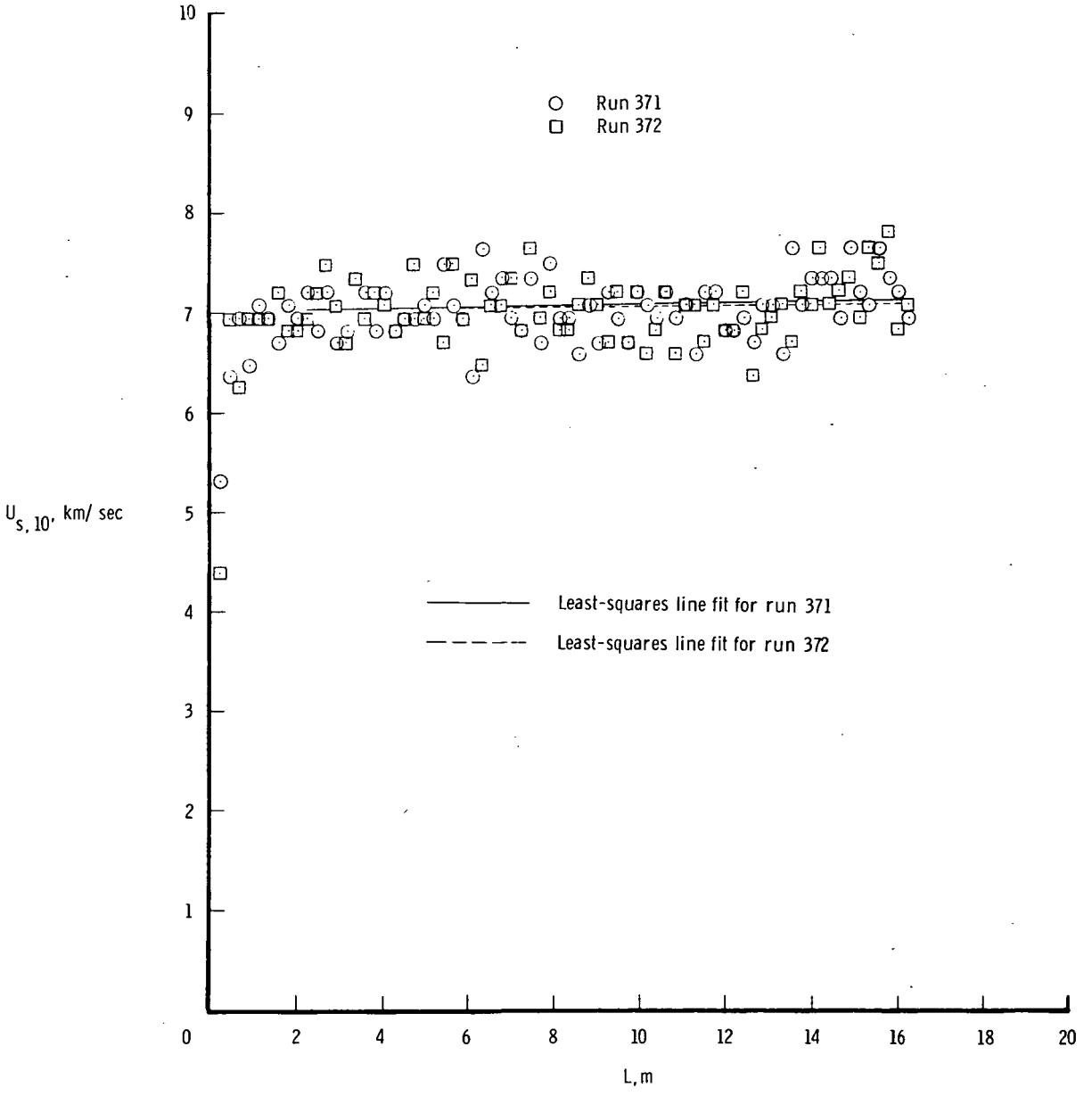


(a) Helium.

Figure 7.- Incident shock velocity into quiescent acceleration gas as inferred from microwave measurements for helium, air, and $CO_2$ acceleration gases.

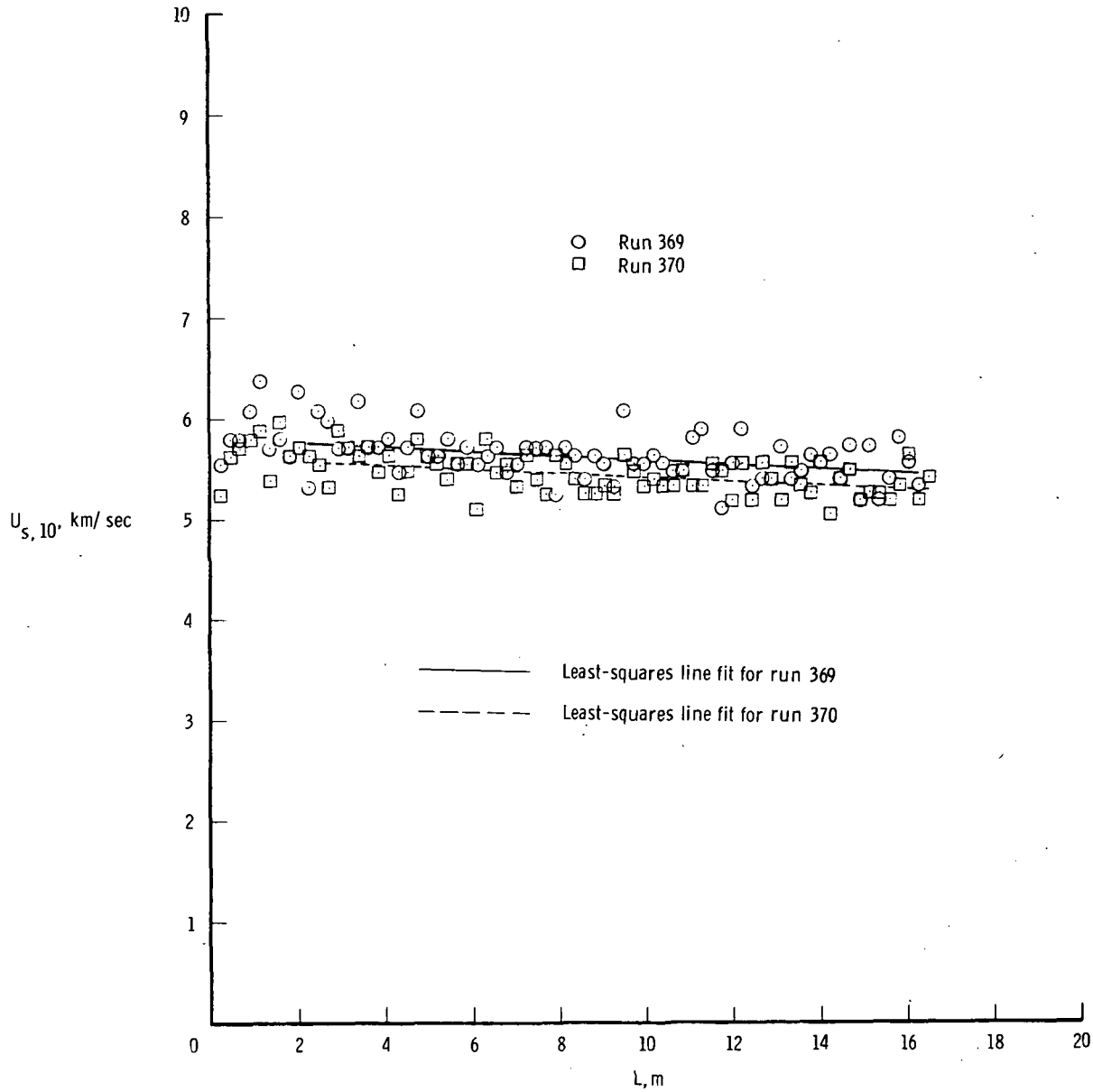


(b) Air.

Figure 7.- Continued.

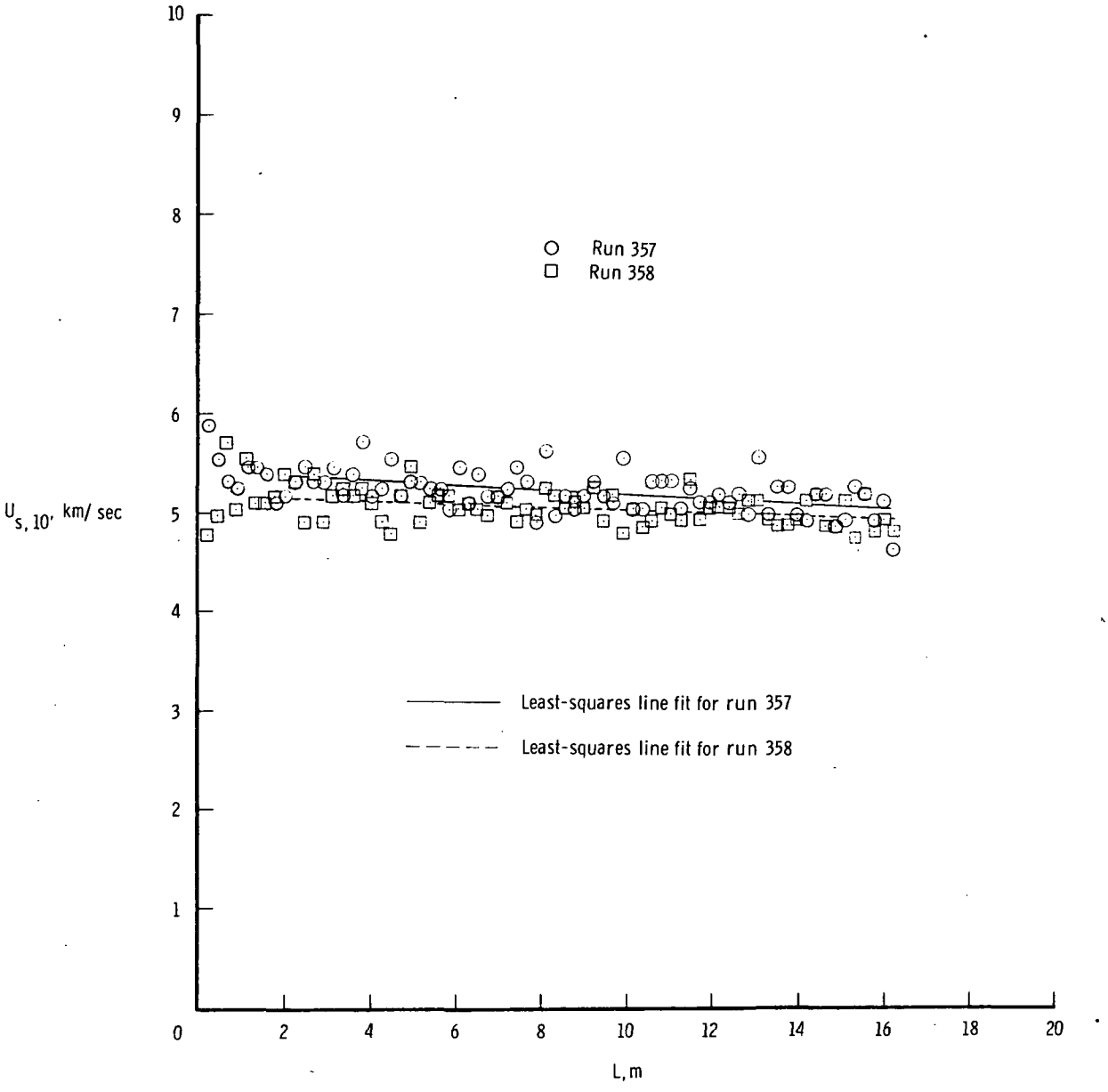


(c) $CO_2$.

Figure 7.- Concluded.

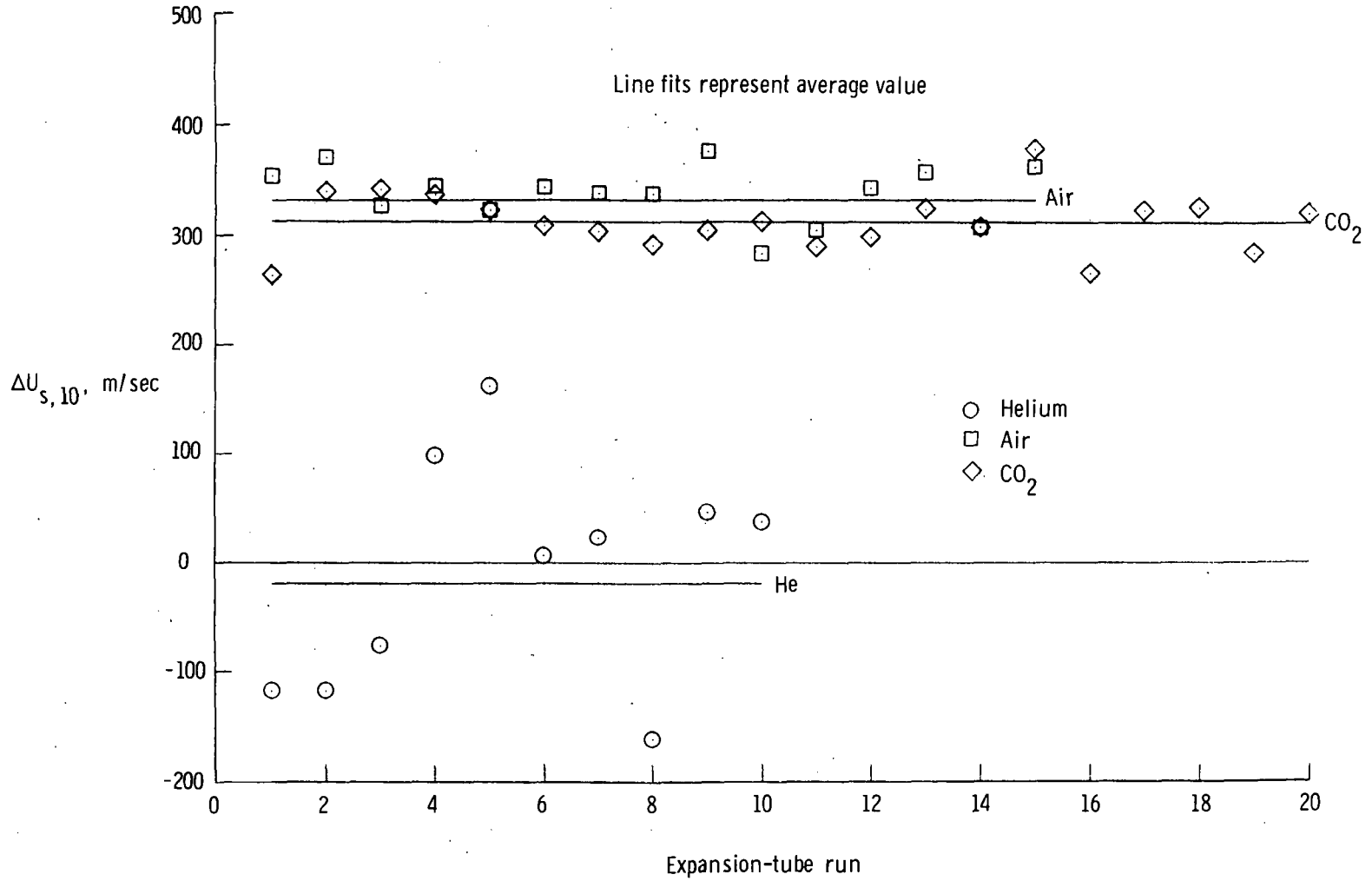


Figure 8.- Variation of incident shock along acceleration section as a function of expansion-tube runs for helium, air, and $CO_2$ test gases.

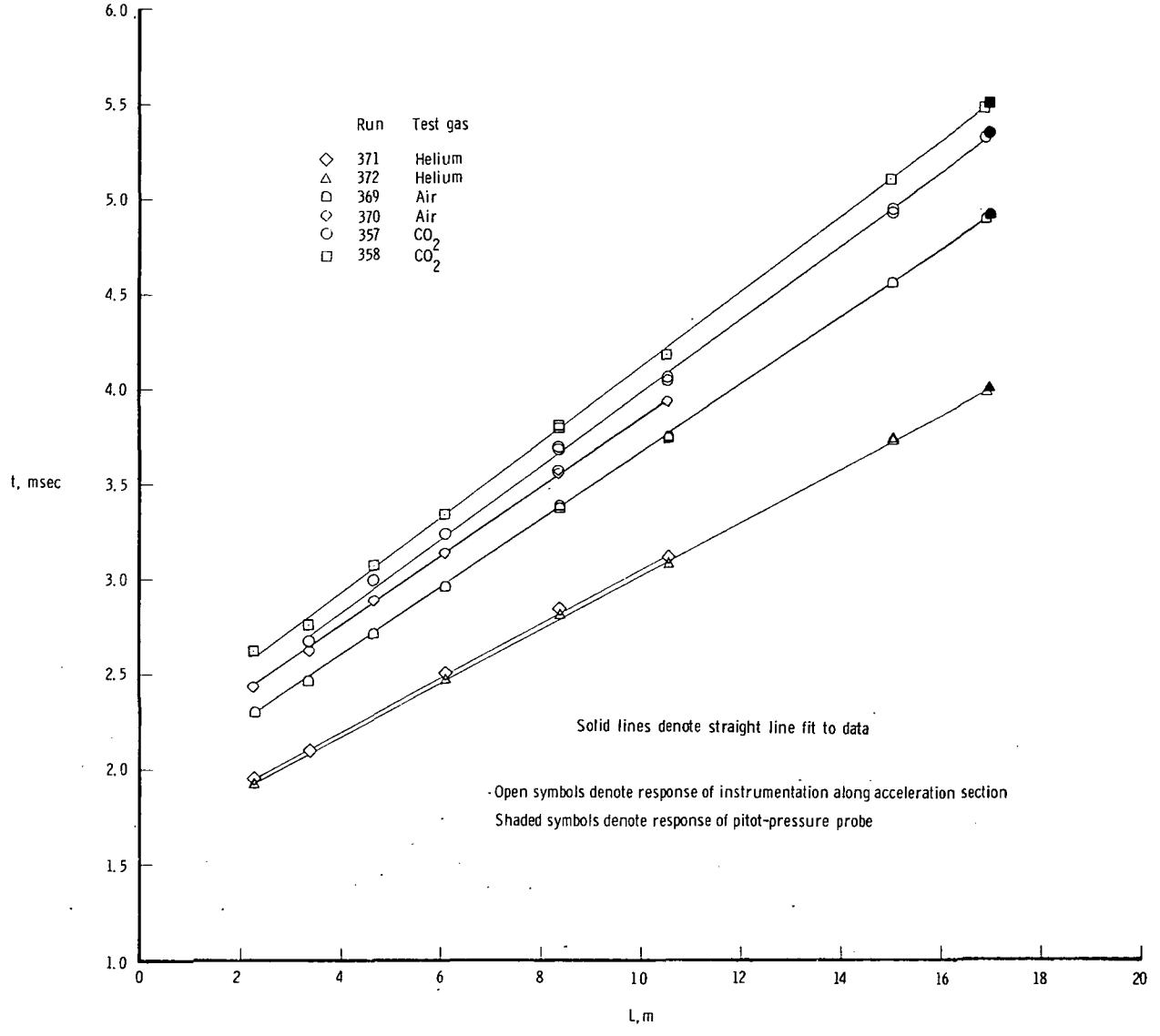


Figure 9.- Distance-time diagram for incident shock into quiescent helium, air, and $CO_2$ acceleration gases.

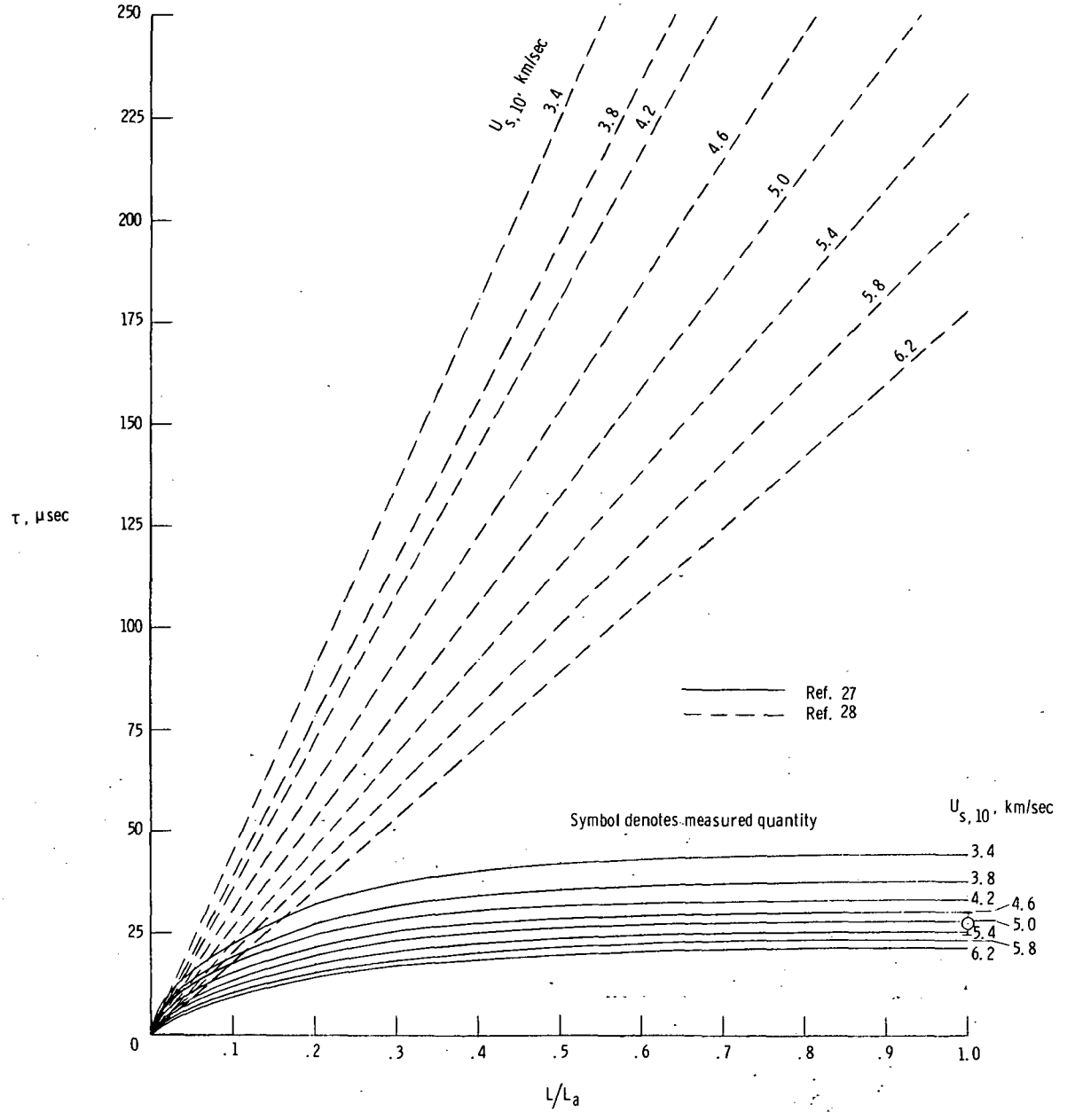


Figure 10.- Predicted time interval between arrival of incident shock into region (10) and test-air—acceleration-air interface as a function of distance downstream from secondary diaphragm. $p_{10} = 8\ N/m^2$.

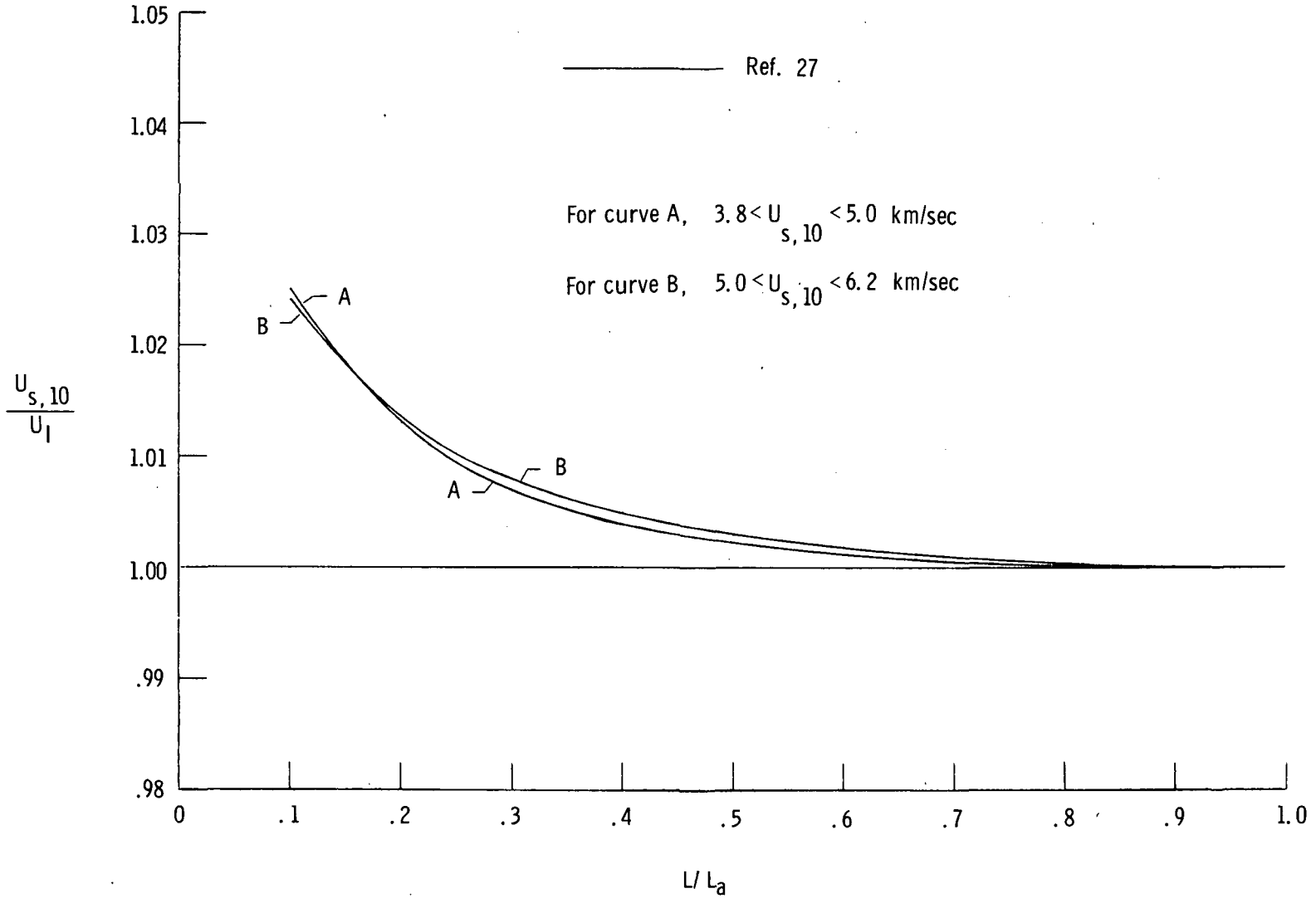


Figure 11.- Predicted ratios of incident shock velocity into region ⑩ to test-air—acceleration-air interface velocity as a function of distance downstream of secondary diaphragm. $p_{10} = 8$ N/m$^2$.

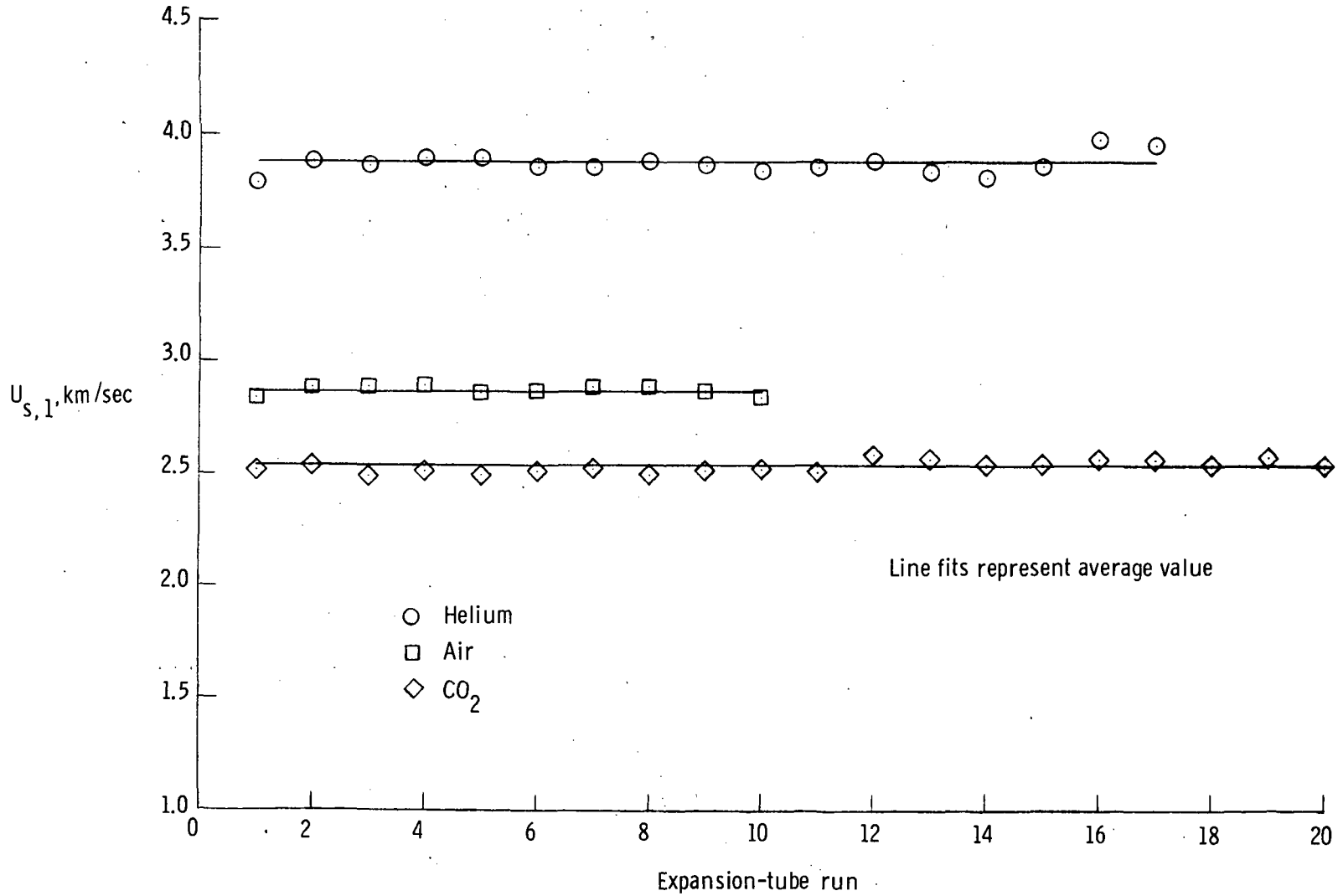


(a) Incident shock velocity into intermediate section.

Figure 12.- Variation of several measured flow quantities with expansion-tube runs for helium, air, and $CO_2$ test gases.

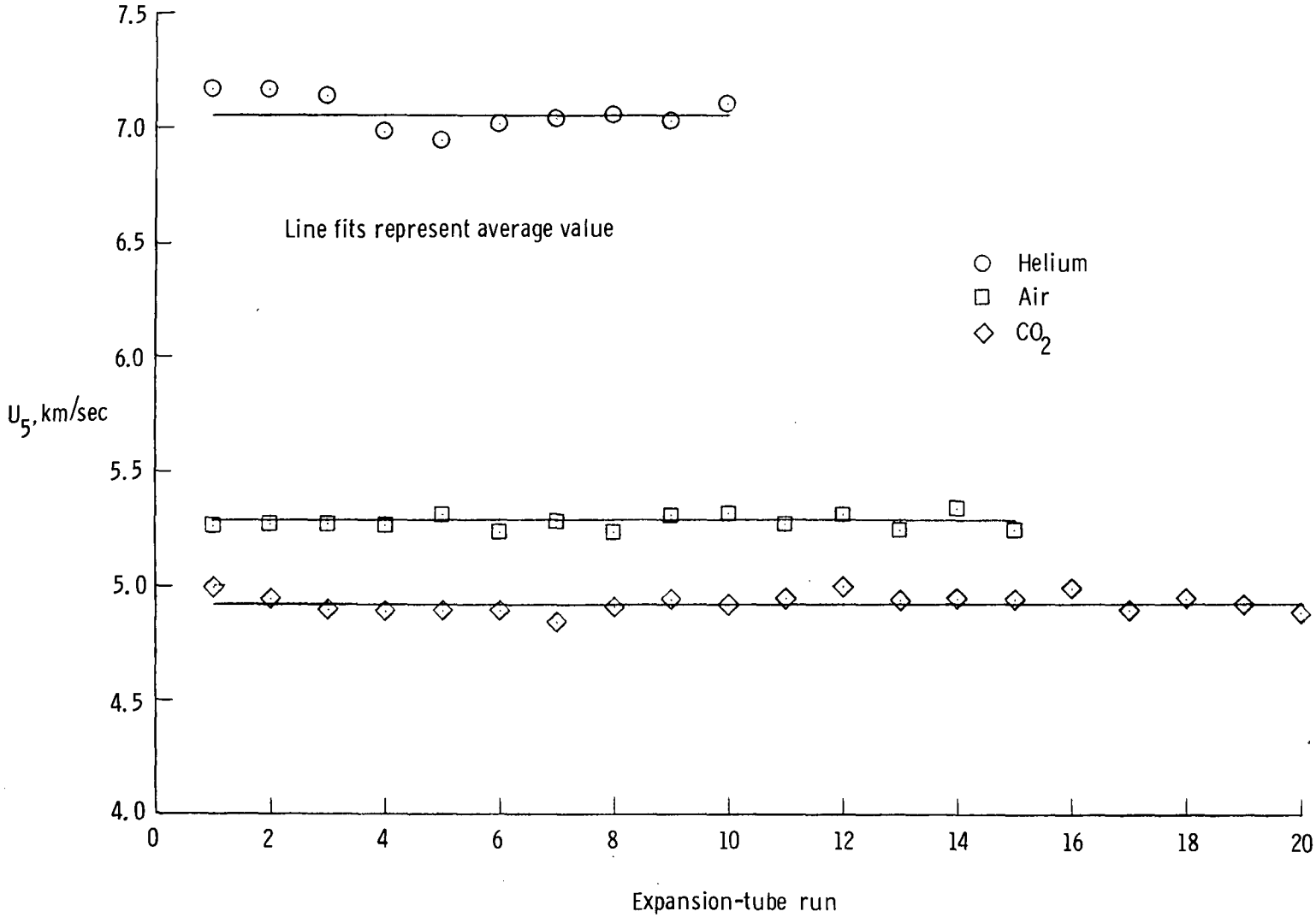


(b) Test-gas—acceleration-gas interface velocity.

Figure 12.- Continued.

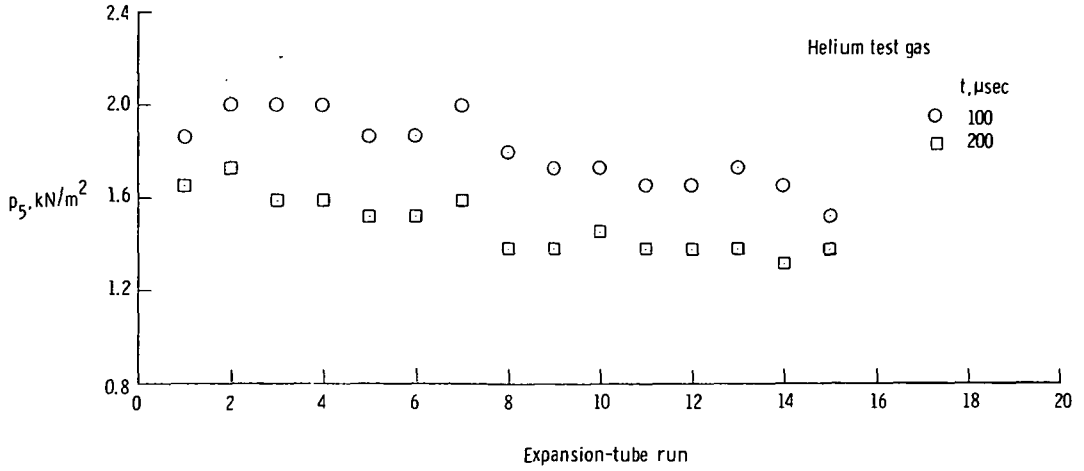


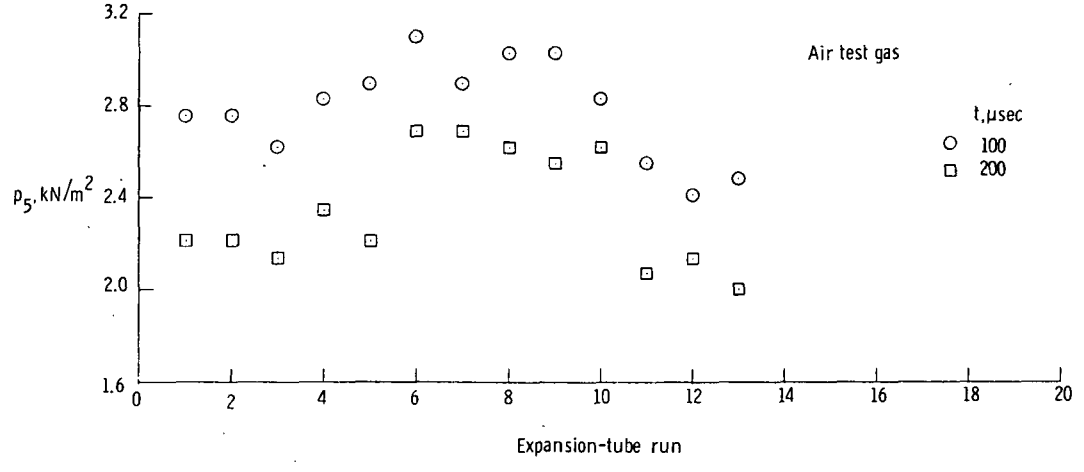


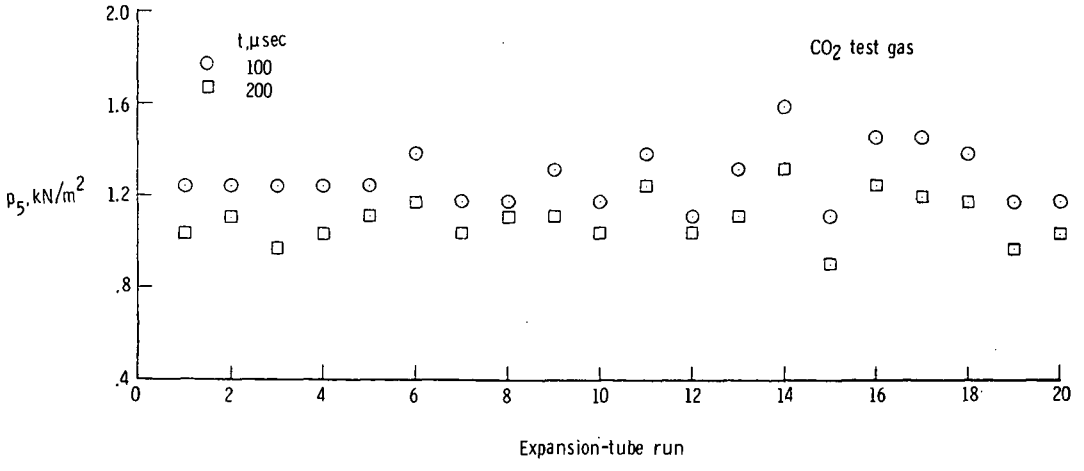


(c) Tube wall pressure.

Figure 12.- Concluded.

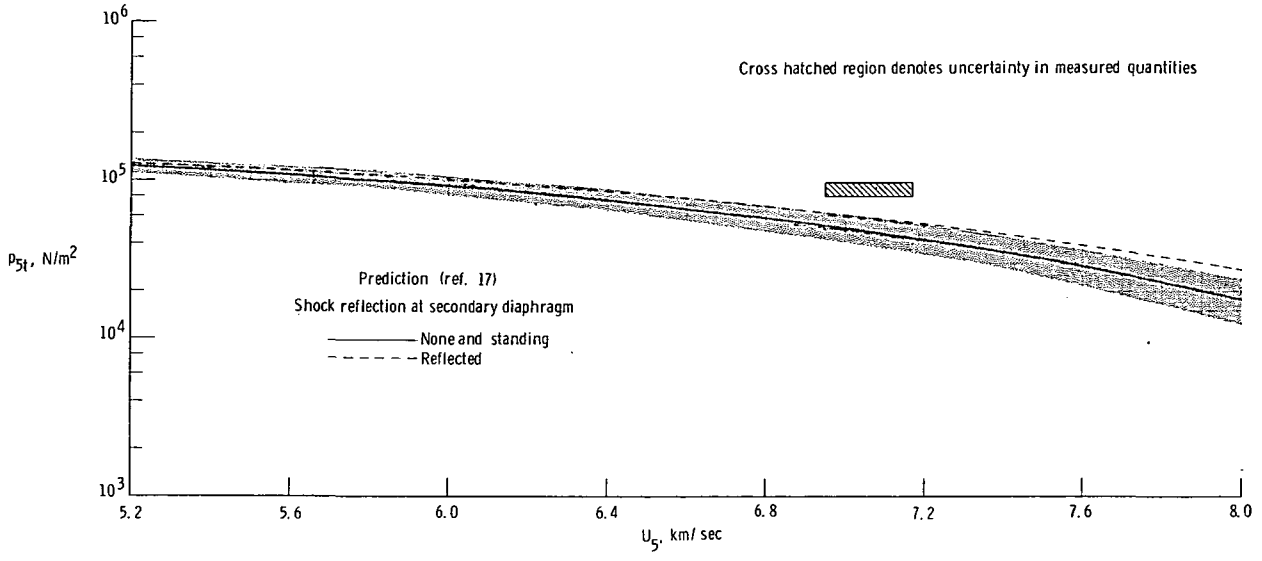


(a) Pitot pressure.

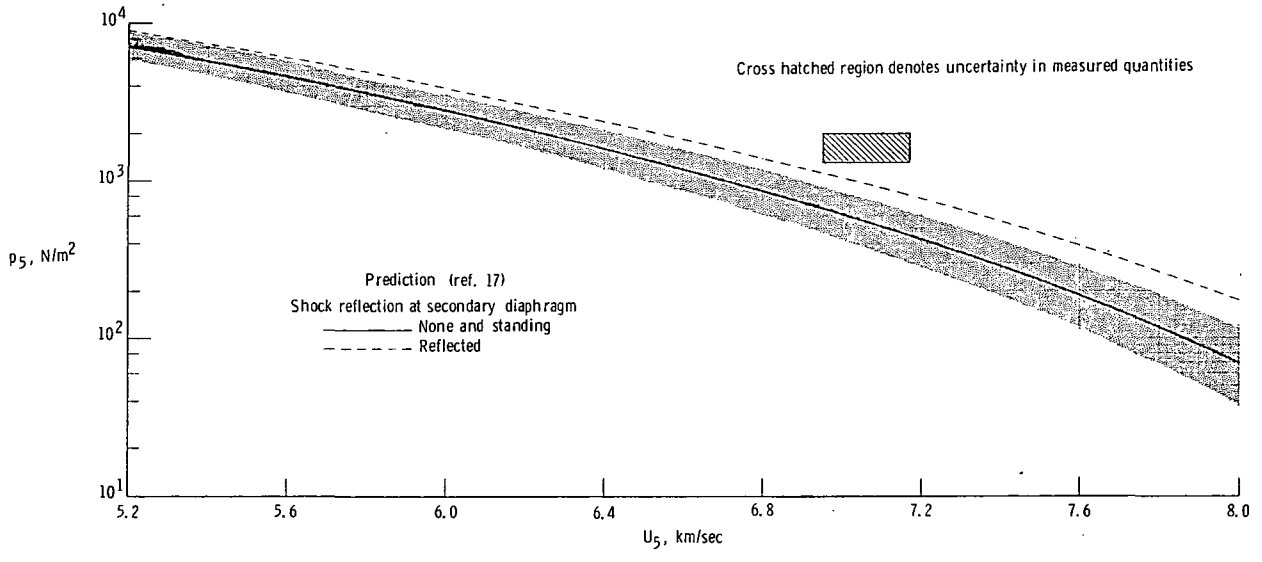


(b) Free-stream static pressure.

Figure 13.- Pitot pressure and free-stream static pressure as a function of free-stream velocity for helium test gas. (Shaded region denotes uncertainty corresponding to ±2.5 percent uncertainty in $U_{s,1}$ for no shock reflection at secondary diaphragm.)

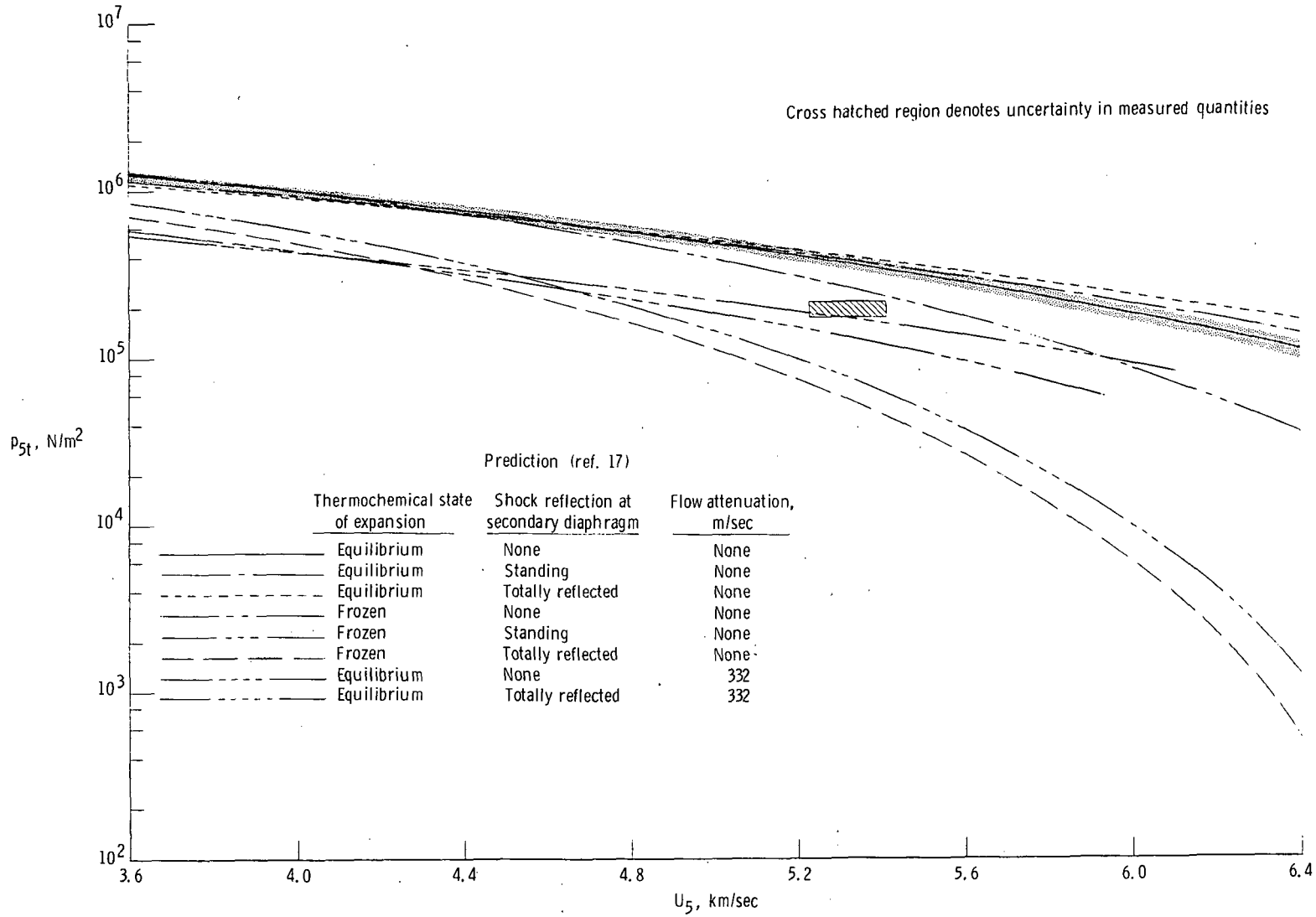


(a) Pitot pressure.

Figure 14.- Pitot pressure and free-stream static pressure as a function of free-stream velocity for air test gas. (Shaded region denotes uncertainty corresponding to ±1.1 percent uncertainty in $U_{s,1}$ for an equilibrium expansion and no shock reflection at secondary diaphragm.)

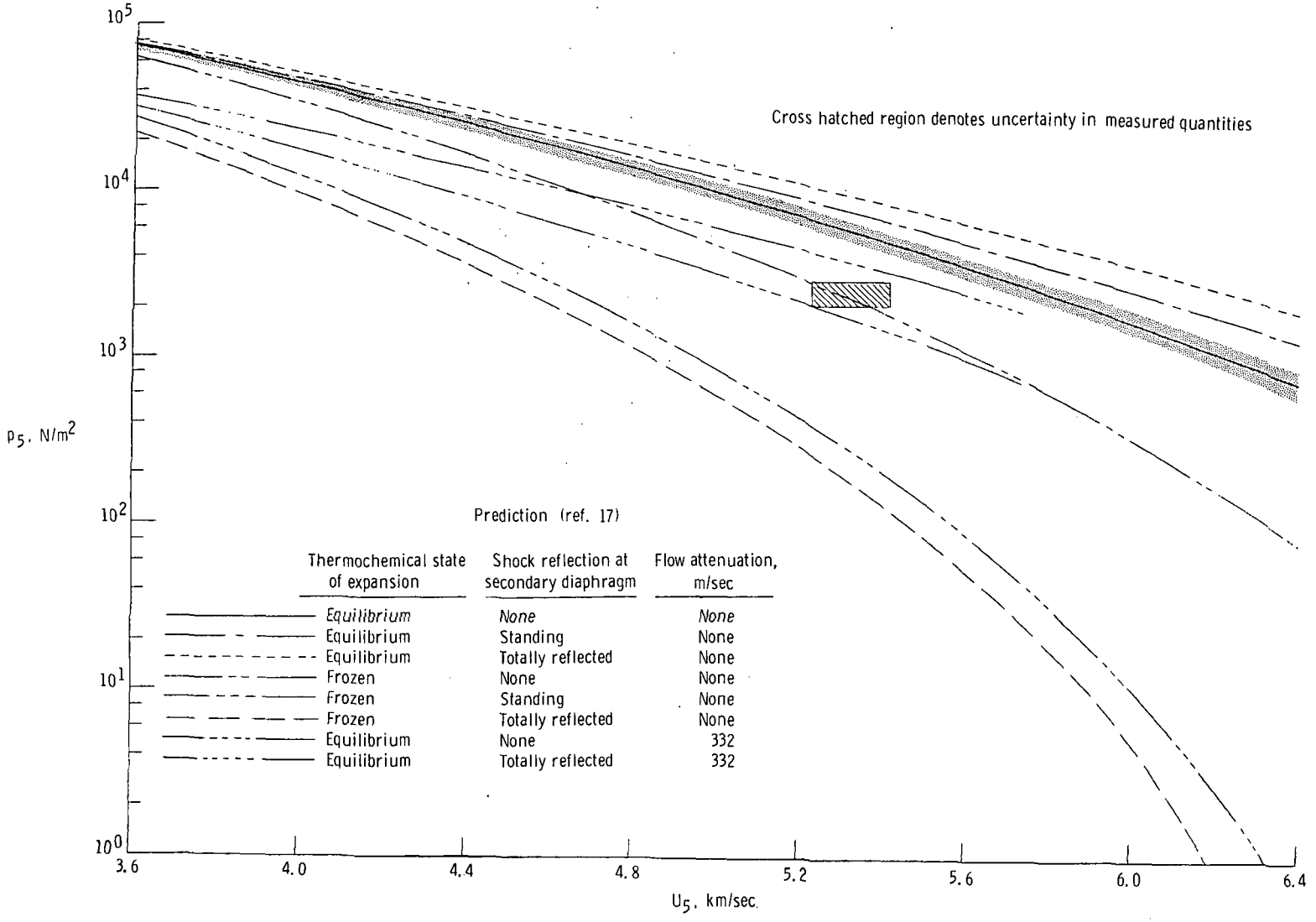


(b) Free-stream static pressure.

Figure 14.- Concluded.

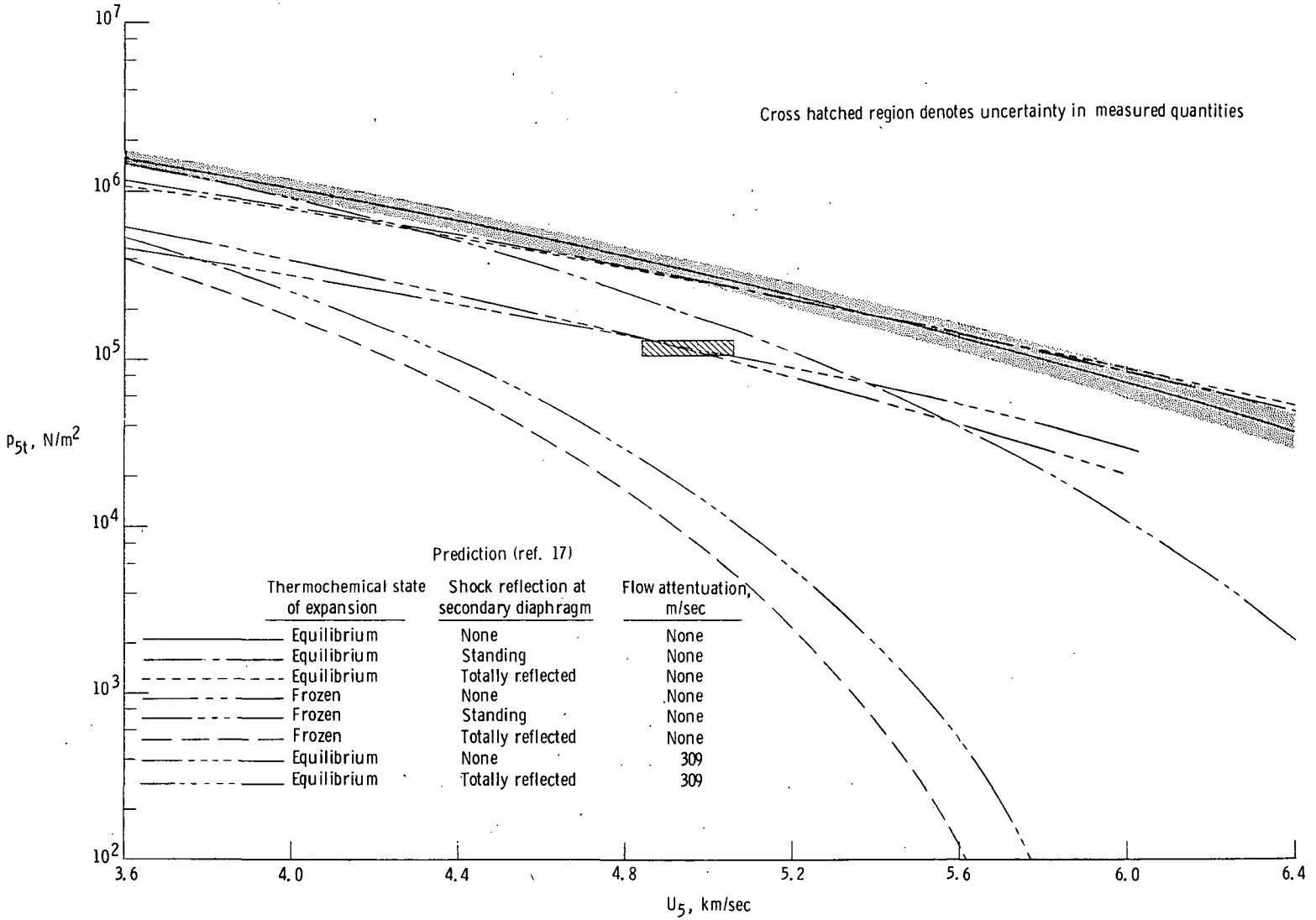


(a) Pitot pressure.

Figure 15.- Pitot pressure and free-stream static pressure as a function of free-stream velocity for $CO_2$ test gas. (Shaded region denotes uncertainty corresponding to ±1.1 percent uncertainty in $U_{s,1}$ for an equilibrium expansion and no shock reflection at secondary diaphragm.)

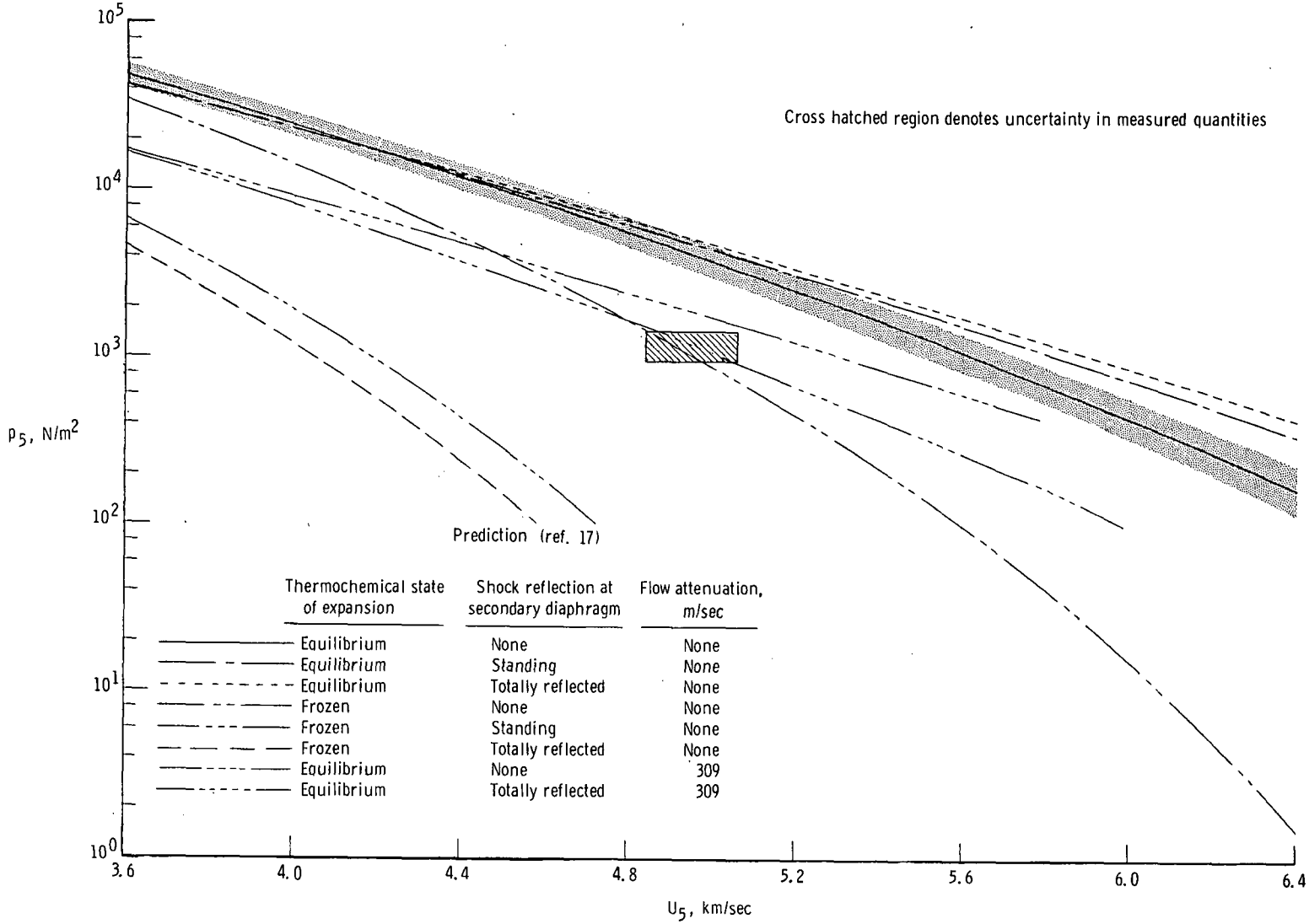


(b) Free-stream static pressure.

Figure 15.- Concluded.

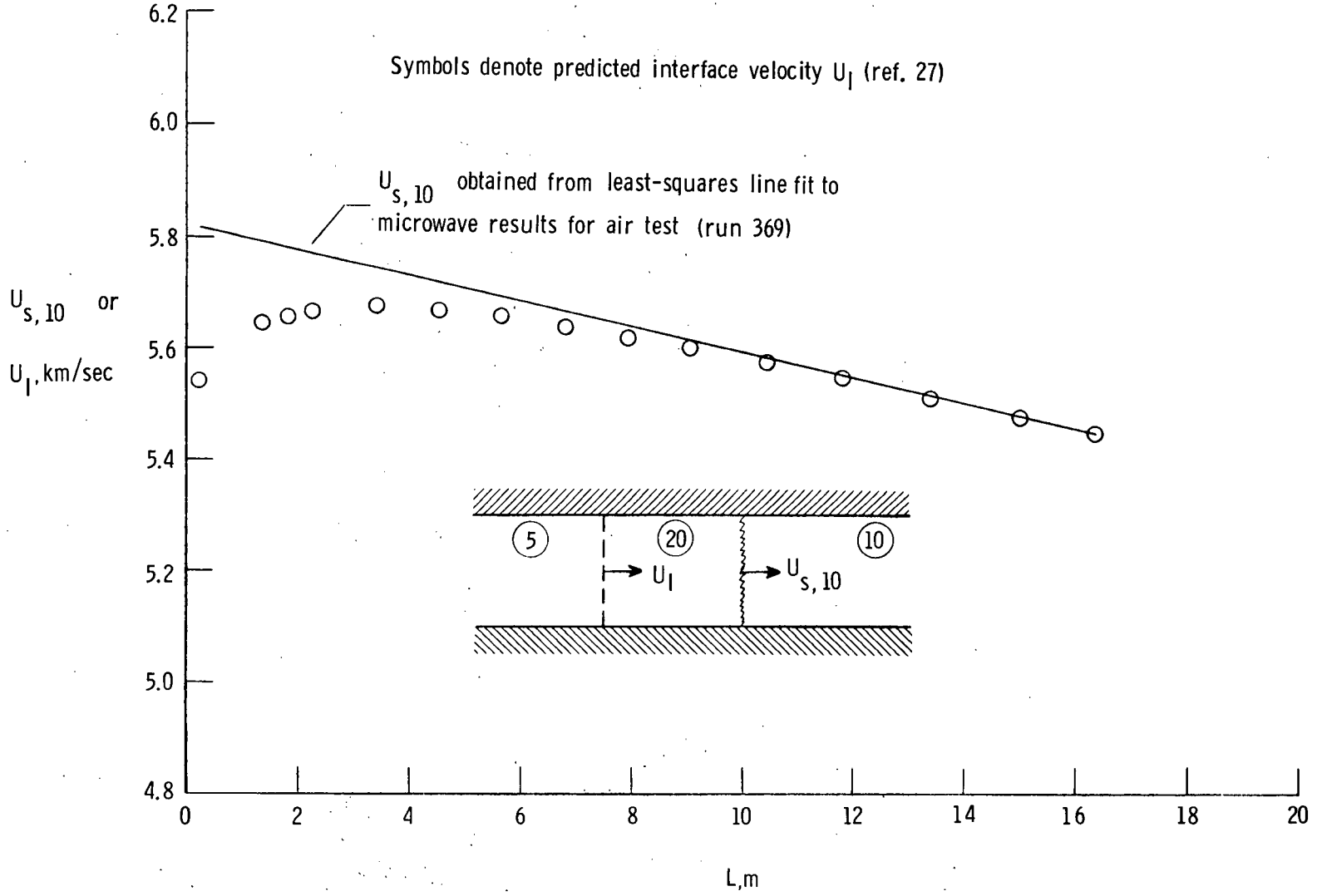


Figure 16.- Incident shock velocity into region (10) and acceleration-air—test-air interface velocity as a function of distance downstream of secondary diaphragm.

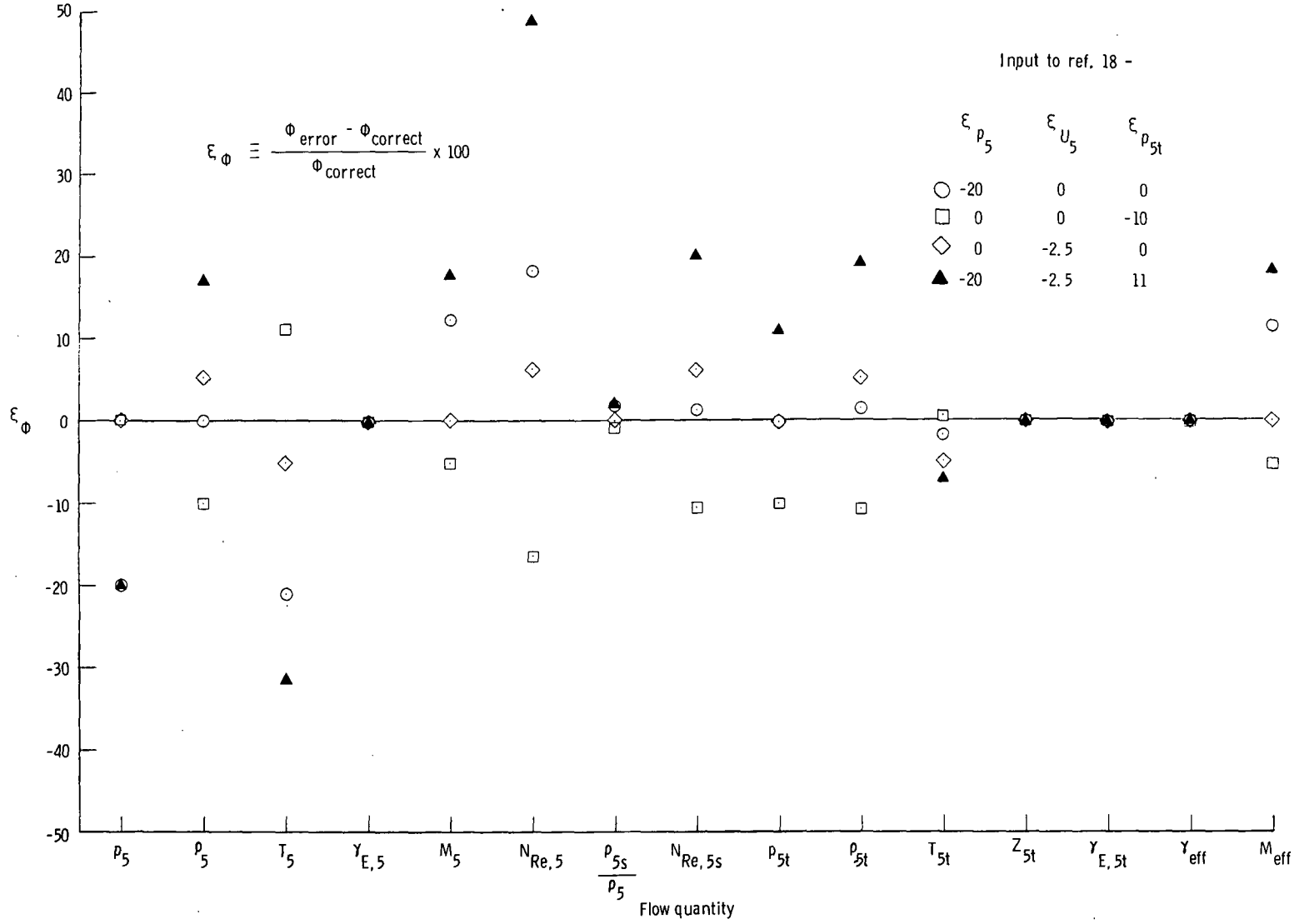


(a) Helium.

Figure 17.- Uncertainties in various free-stream and postshock flow quantities resulting from uncertainties in measured inputs to reference 18 for helium, air, and $CO_2$ test gases.

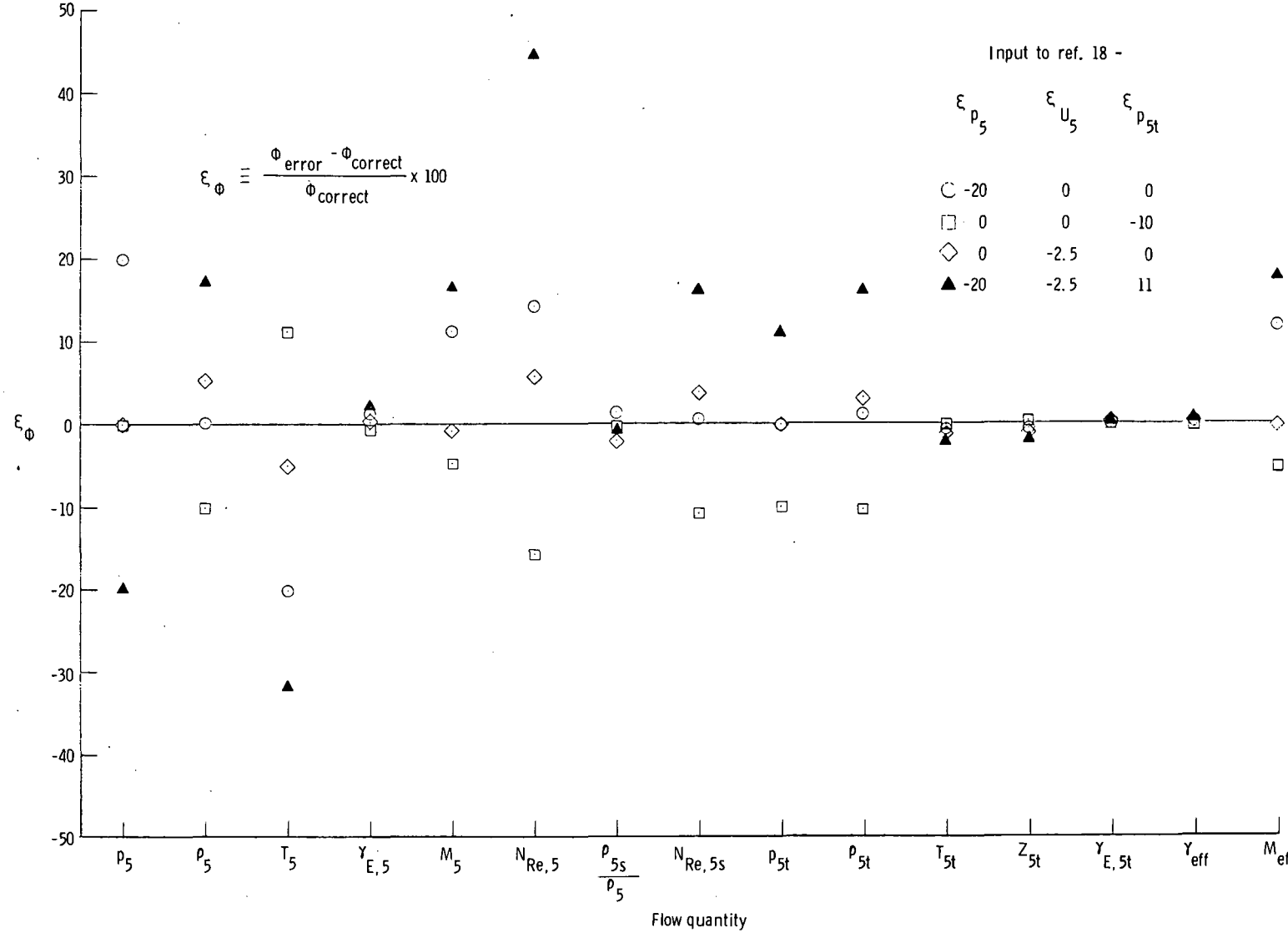


(b) Air.

Figure 17.- Continued.

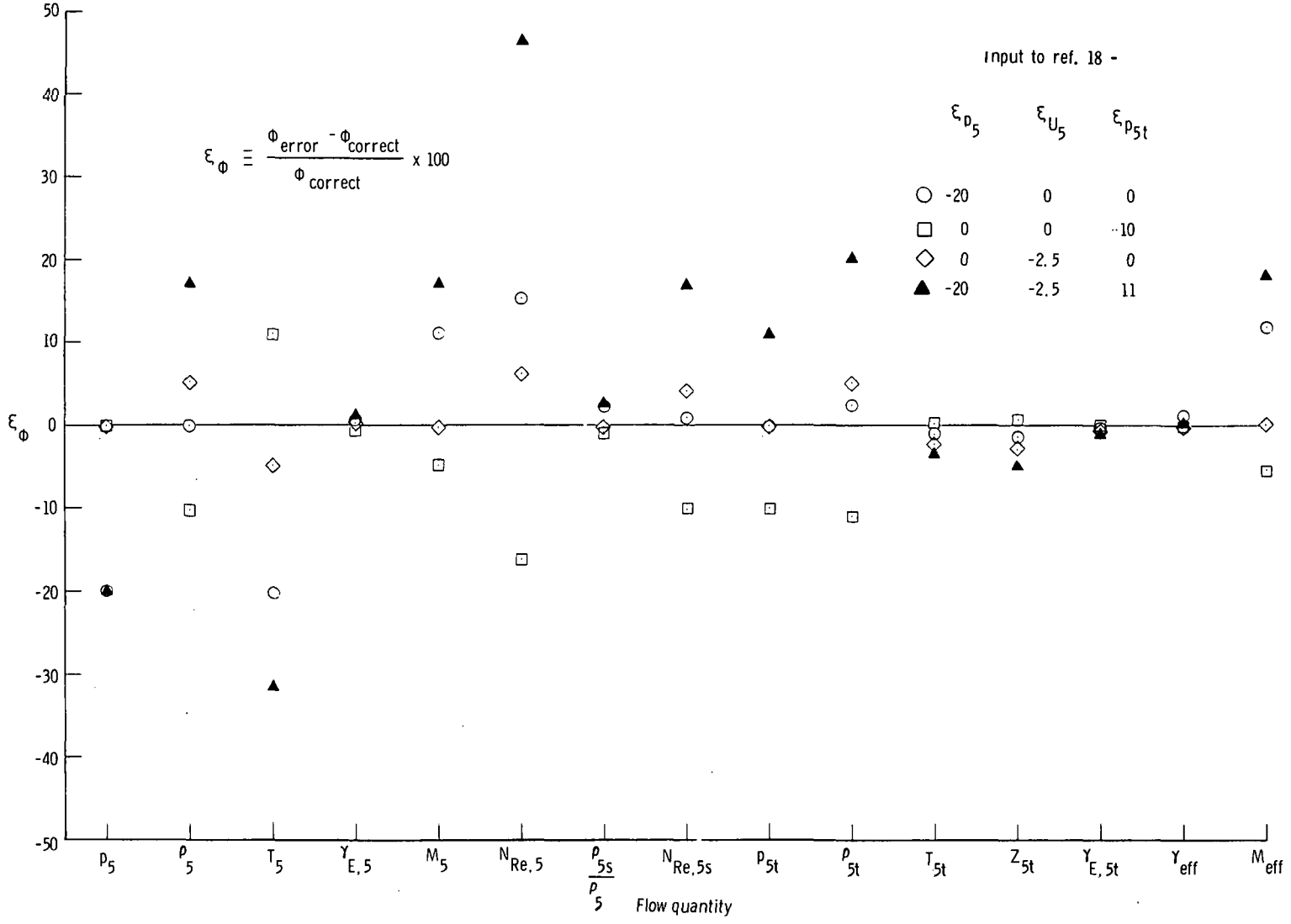


(c) $CO_2$.

Figure 17. Concluded.

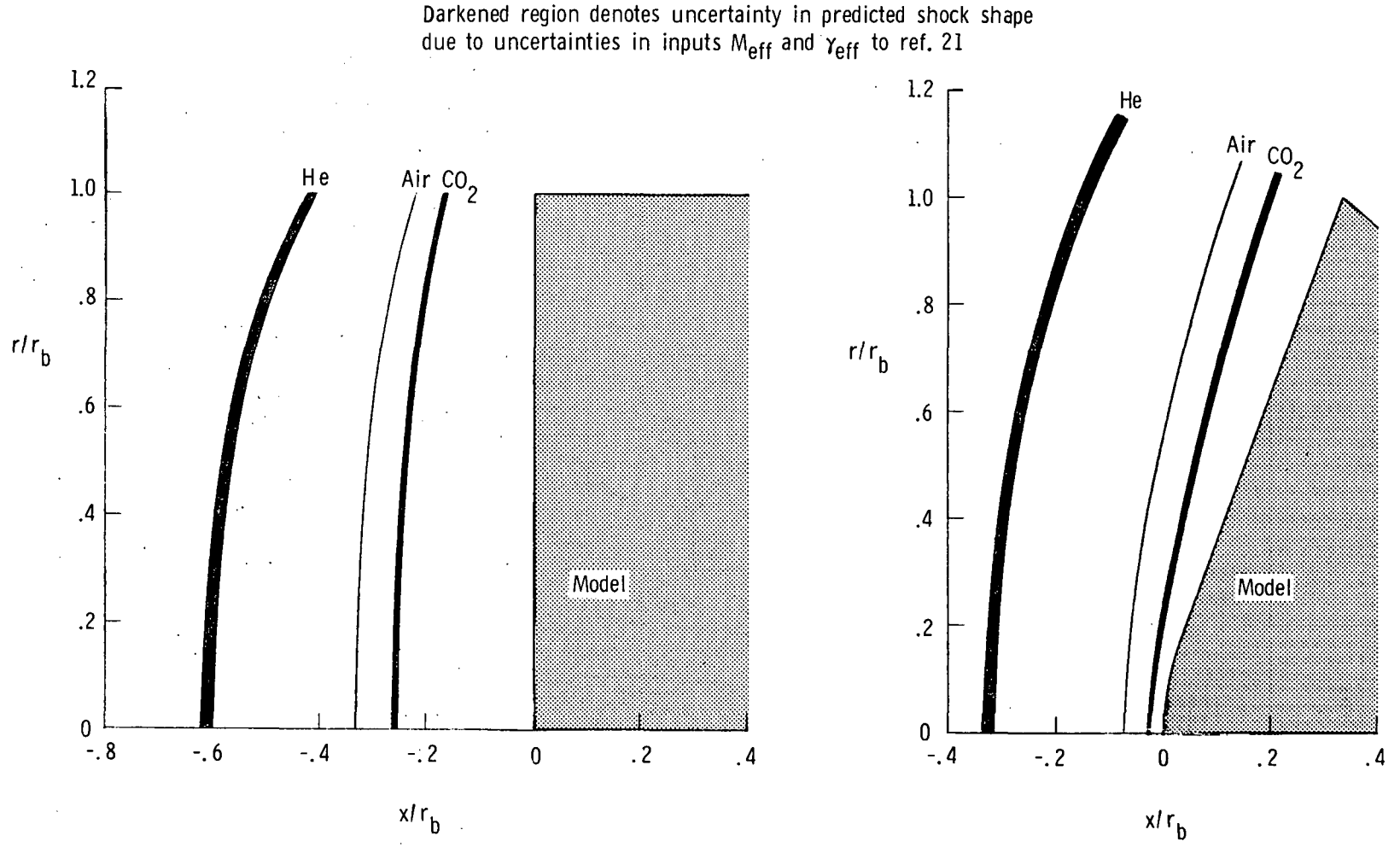


(a) Flat-faced cylinder.

(b) Spherically blunted cone. $\theta = 70^{o}$; $r_n/r_b = 0.5$.

Figure 18.- Effect of uncertainties in inputs to program of reference 21 on predicted shock shape for flat-faced cylinder and spherically blunted cone.

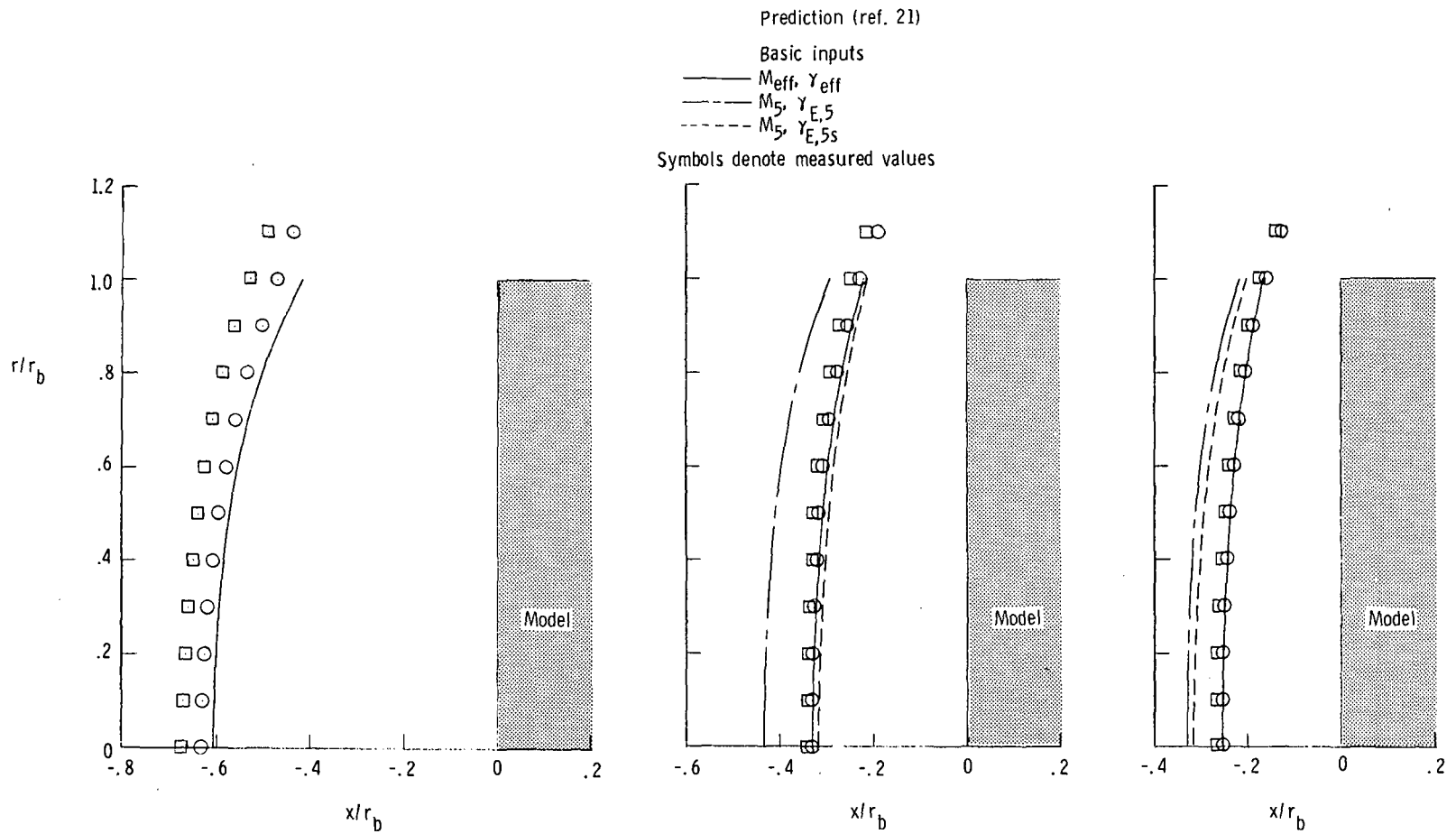


(a) Helium. $M_5 = 6.0$; $\epsilon = 3.7$. (b) Air. $M_5 = 7.7$; $\epsilon = 11.1$. (c) $CO_2$. $M_5 = 9.2$; $\epsilon = 18.8$.

Figure 19.- Measured and predicted shock shapes for flat-faced cylinder in helium, air, and $CO_2$ test gases. $d_b = 5.72$ cm.

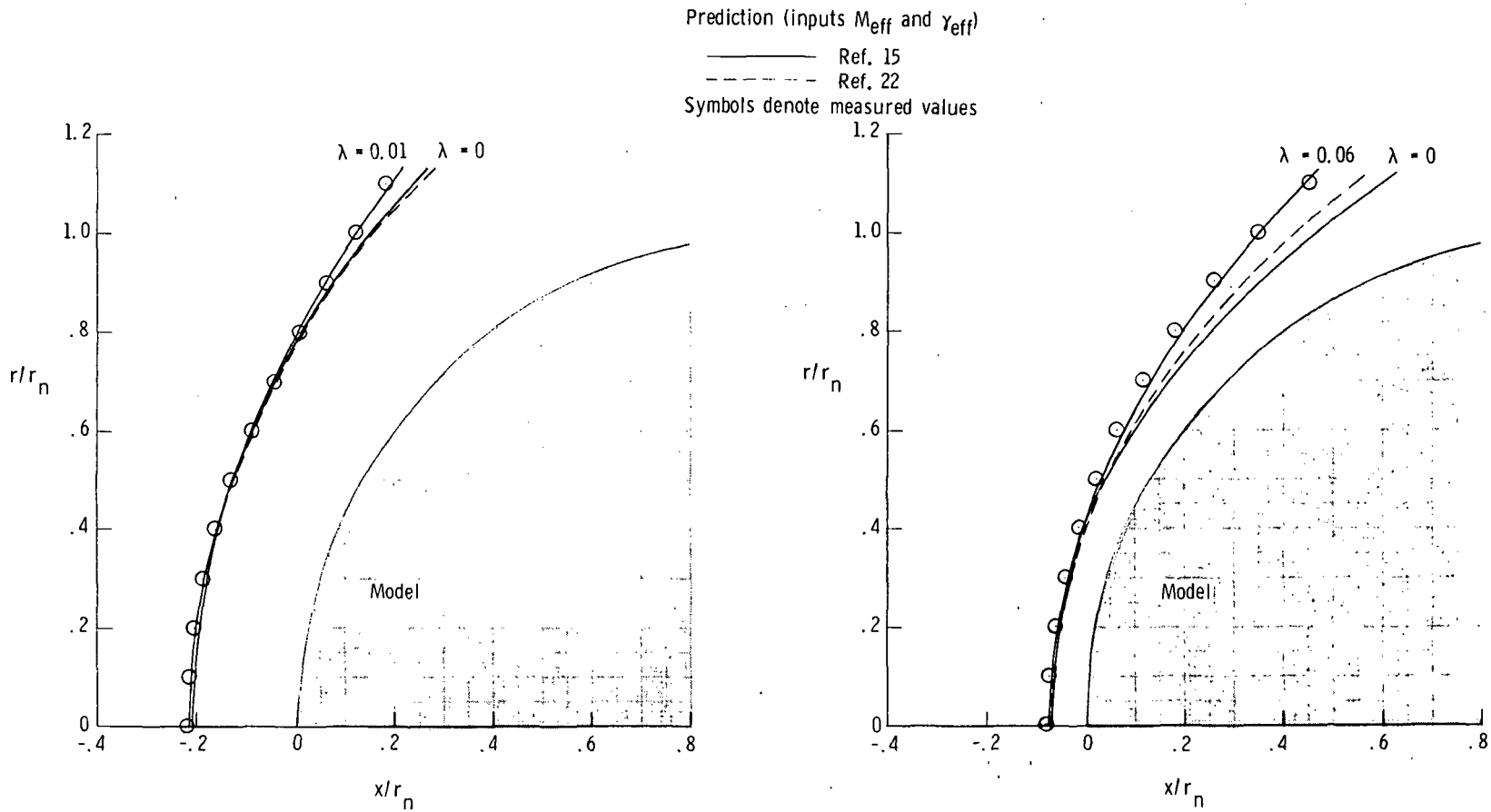


(a) Helium. $M_5 = 6.0$; $\epsilon = 3.7$.

(b) Air. $M_5 = 7.7$; $\epsilon = 11.1$.

Figure 20.- Measured and predicted shock shapes for sphere model in helium, air, and $CO_2$ test gases. $d_n = 6.35$ cm.

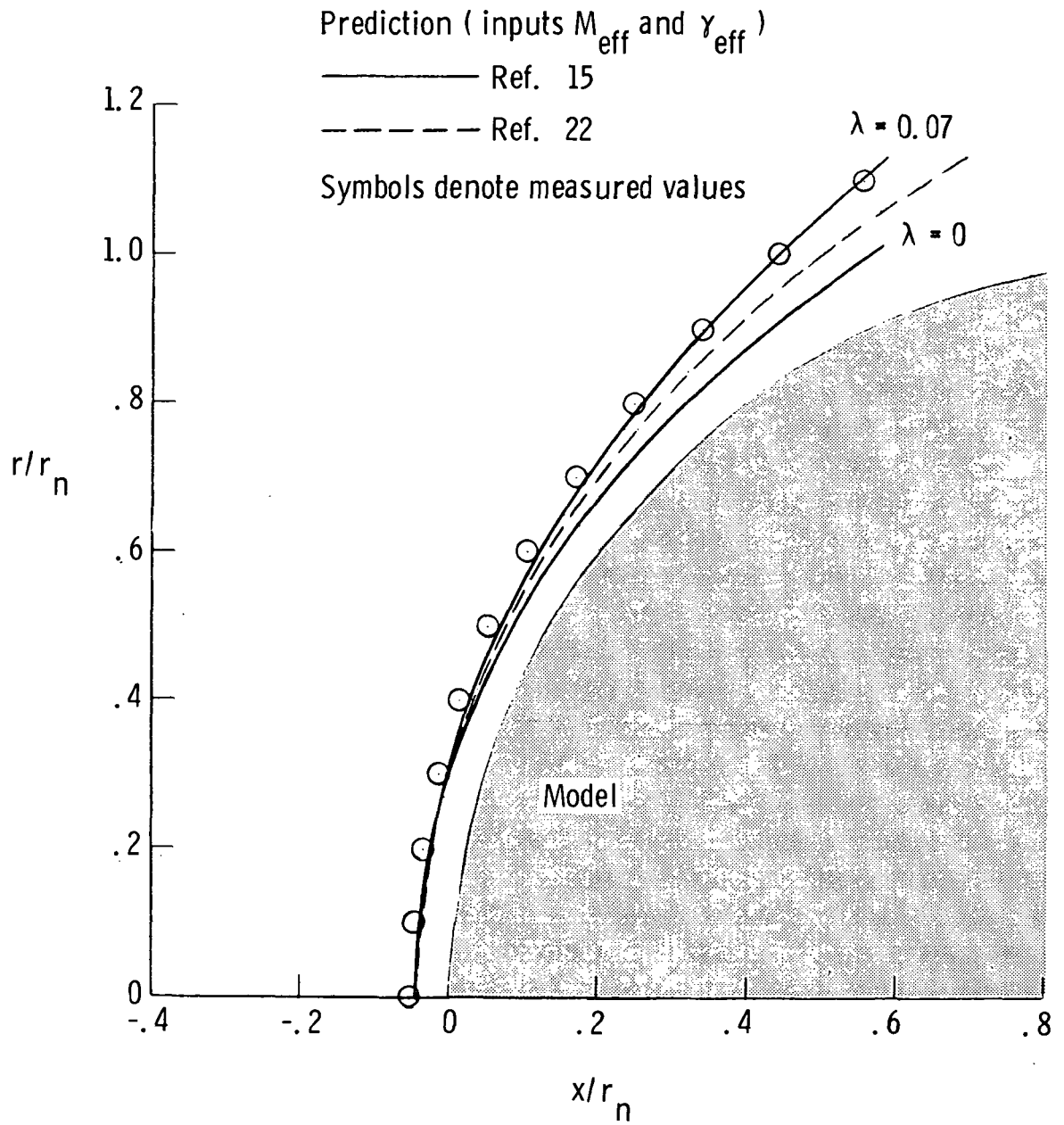


(c) $CO_2$. $M_5 = 9.2$; $\epsilon = 18.8$.

Figure 20.- Concluded.

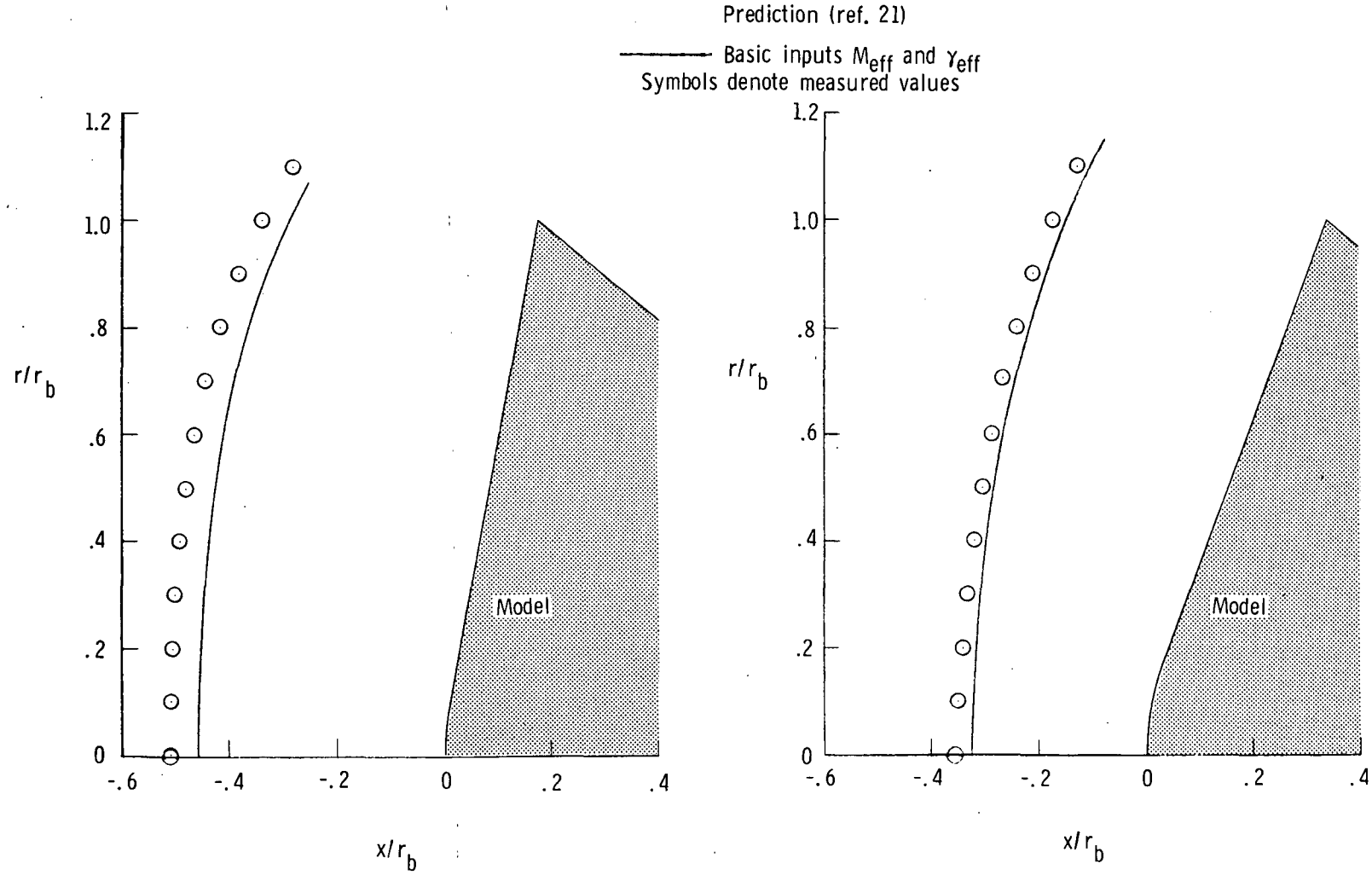


Figure 21.- Measured and predicted shock shapes for spherically blunted cone models in helium test gas. $r_n/r_b = 0.5$; $r_b = 2.54$ cm; $M_5 = 6.0$; $\epsilon = 3.7$.

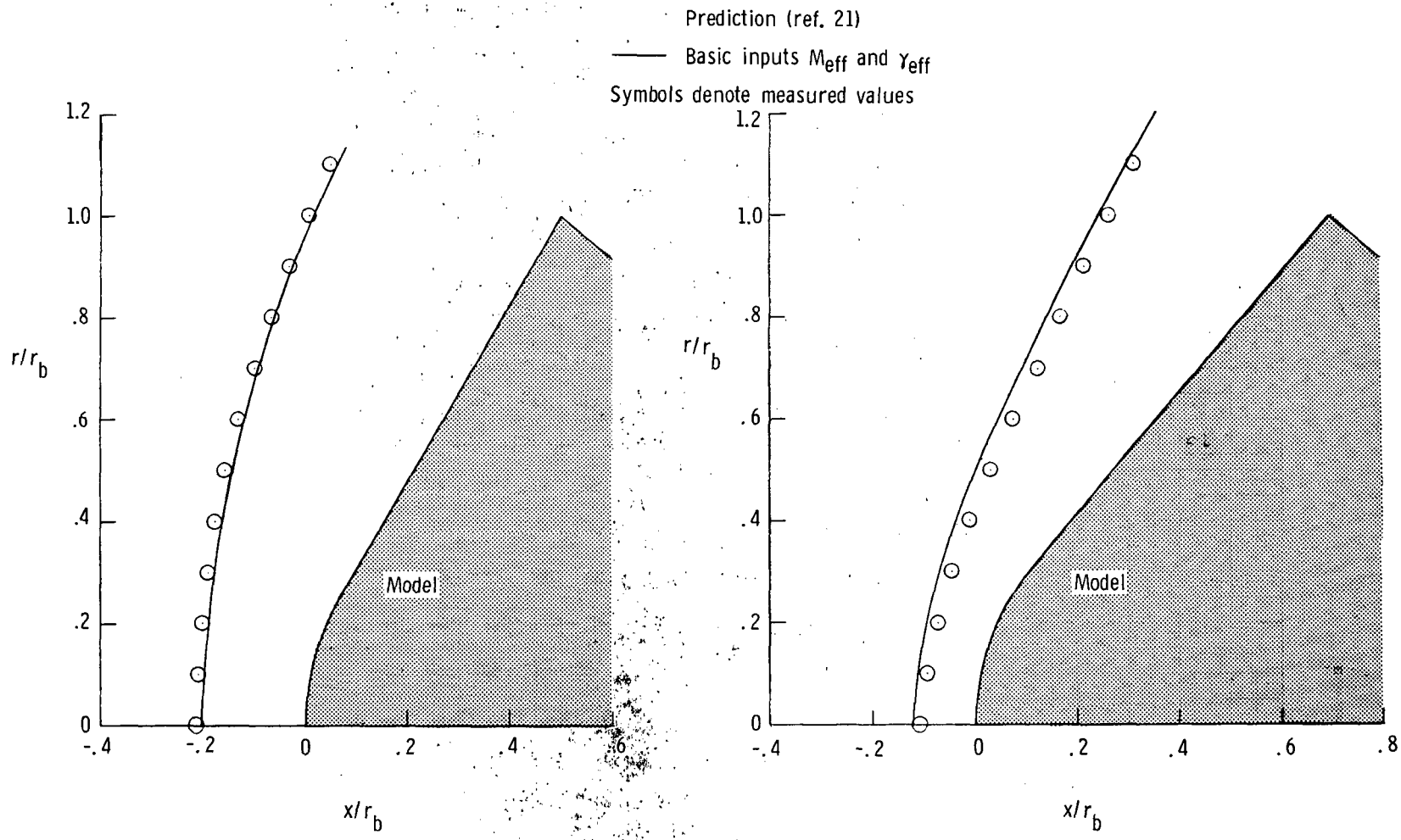


(c) $\theta = 60^{o}$.

(d) $\theta = 50^{o}$.

Figure 21.- Concluded.

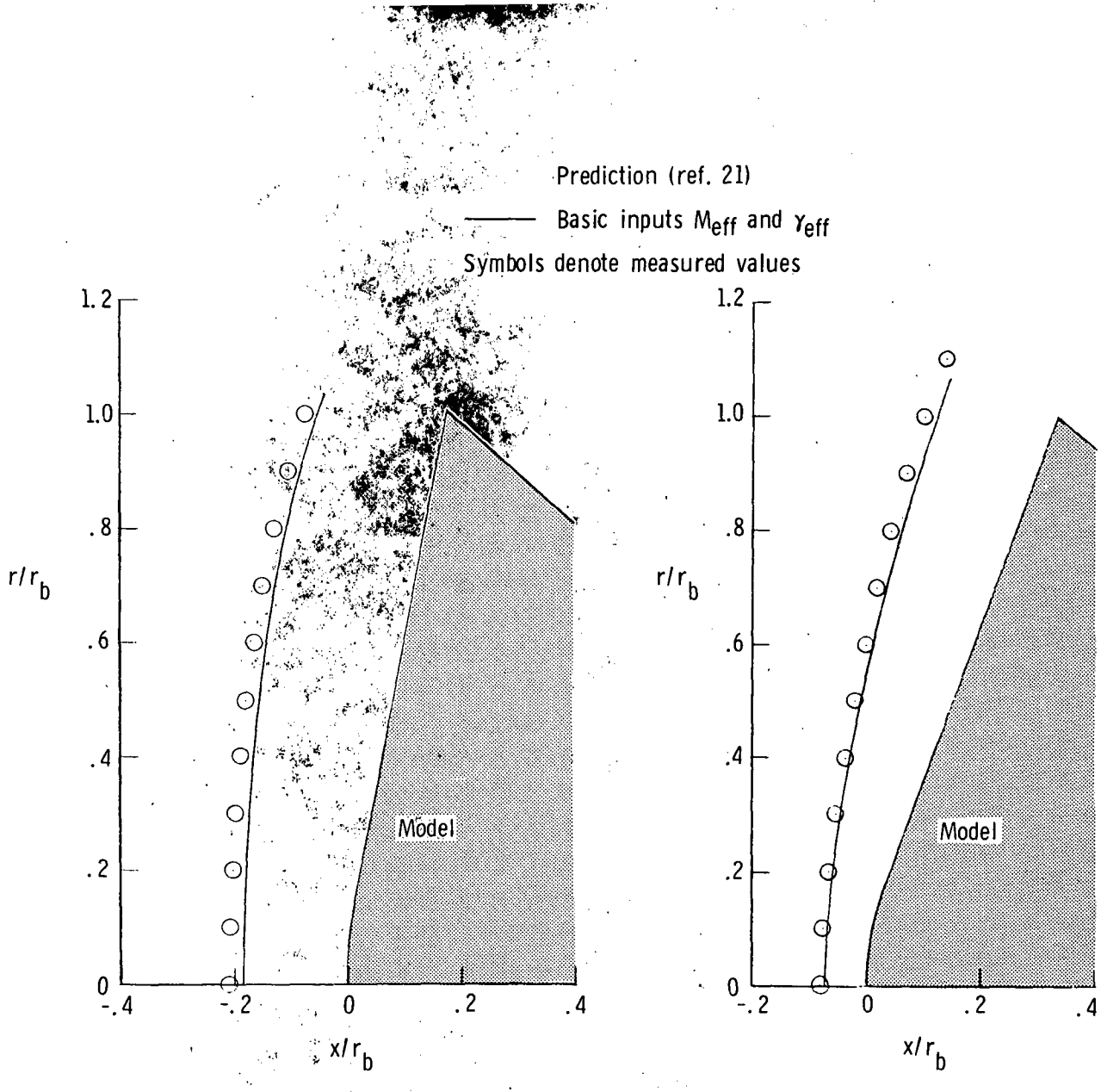


Figure 22.- Measured and predicted shock shapes for spherically blunted cone models in air test gas. $r_n/r_b = 0.5$; $r_b = 2.54$ cm; $M_5 = 7.7$; $\epsilon = 11.1$.

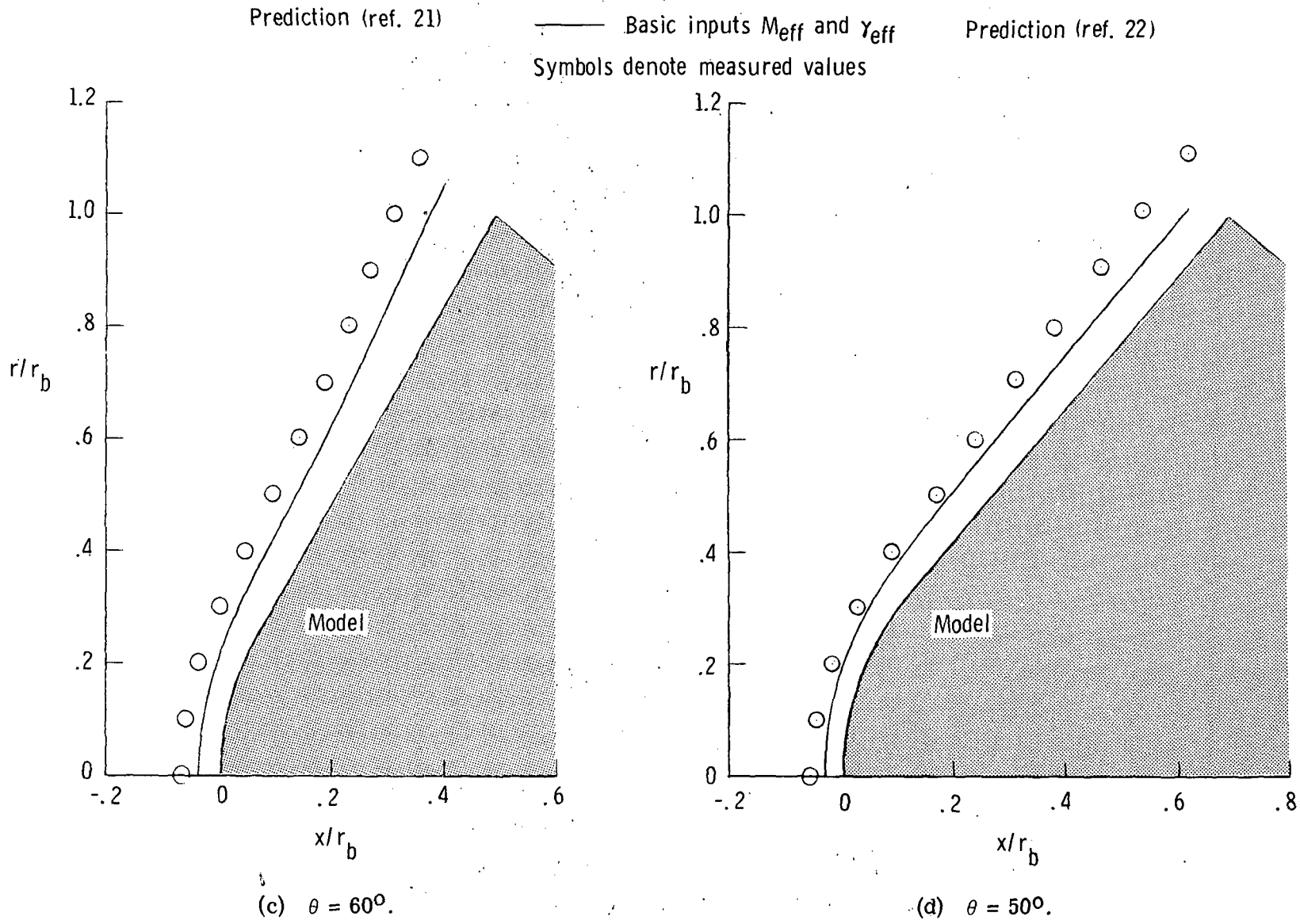


(c) $\theta = 60^{o}$.

(d) $\theta = 50^{o}$.

Figure 22.- Concluded.

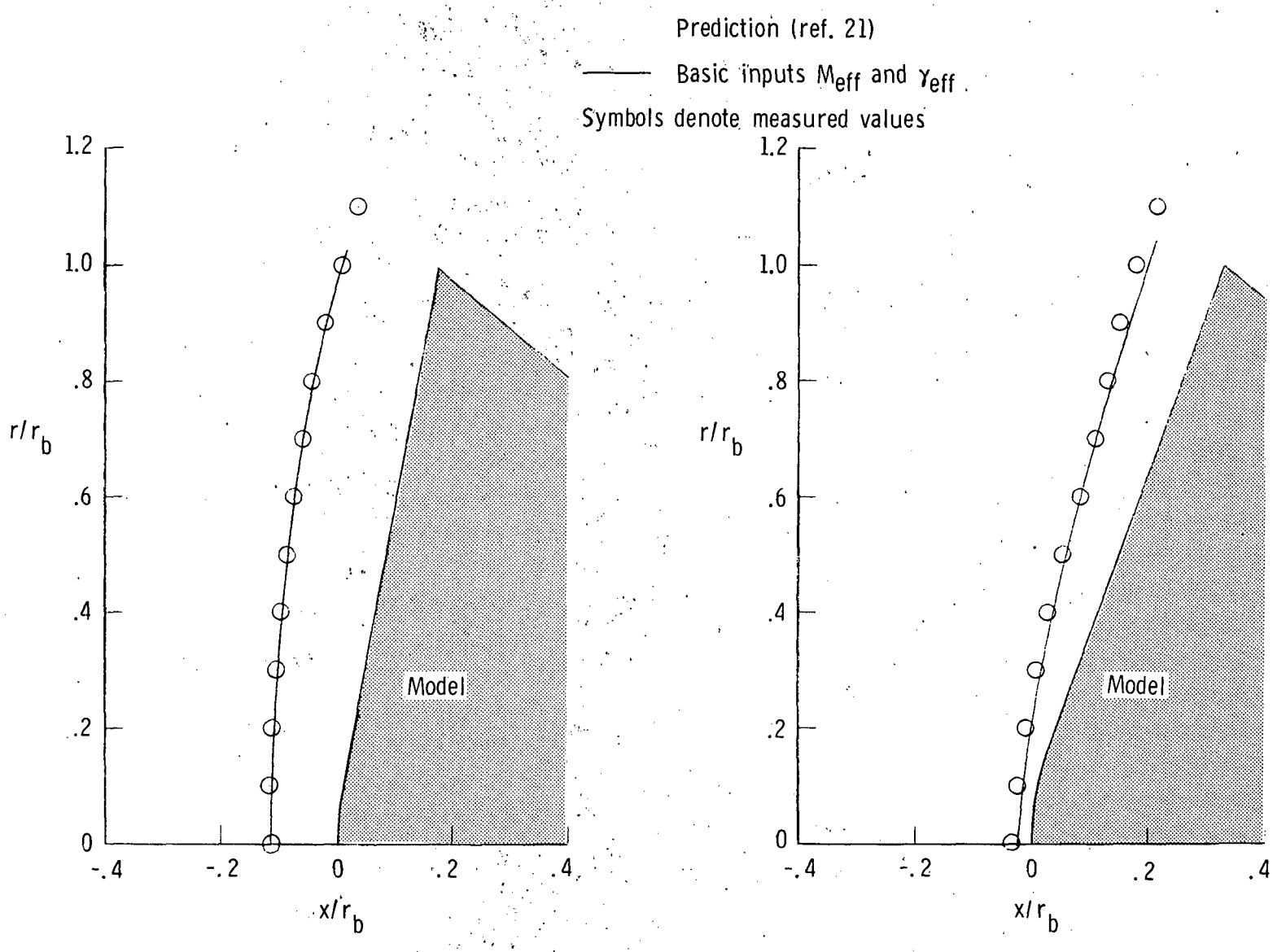


Figure 23.- Measured and predicted shock shapes for spherically blunted cone models in $CO_2$ test gas. $r_n/r_b = 0.5$; $r_b = 2.54$ cm; $M_5 = 9.2$; $\epsilon = 18.8$.

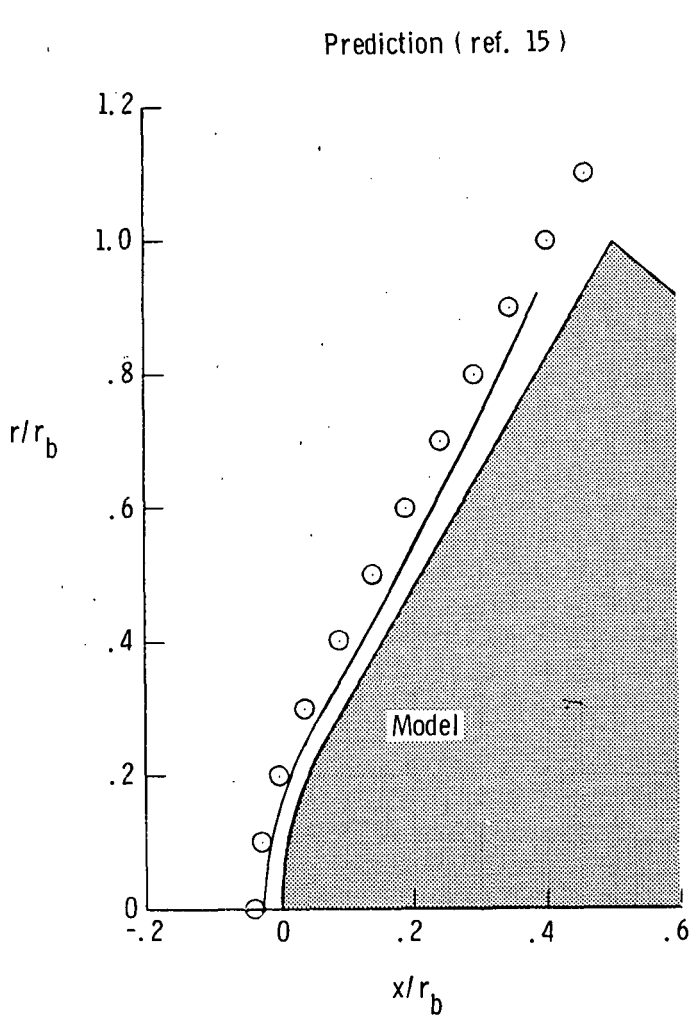


(c) $\theta = 60^{o}$.

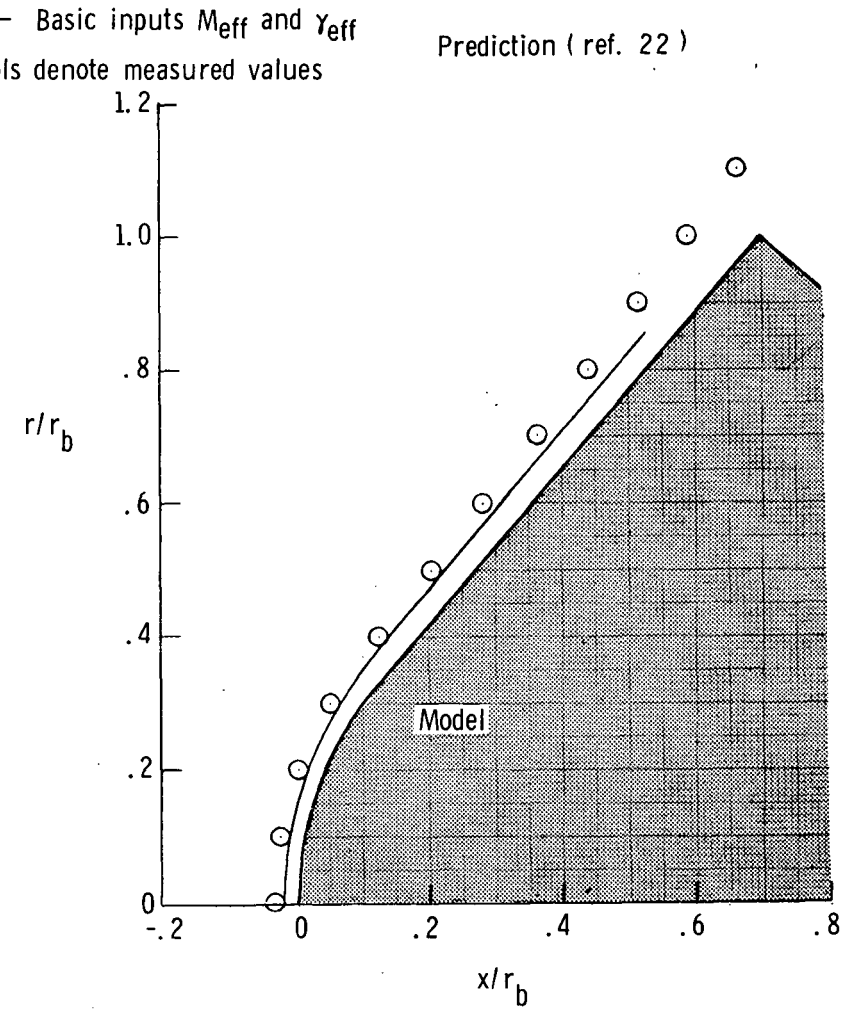


(d) $\theta = 50^{o}$.

Figure 23.- Concluded.

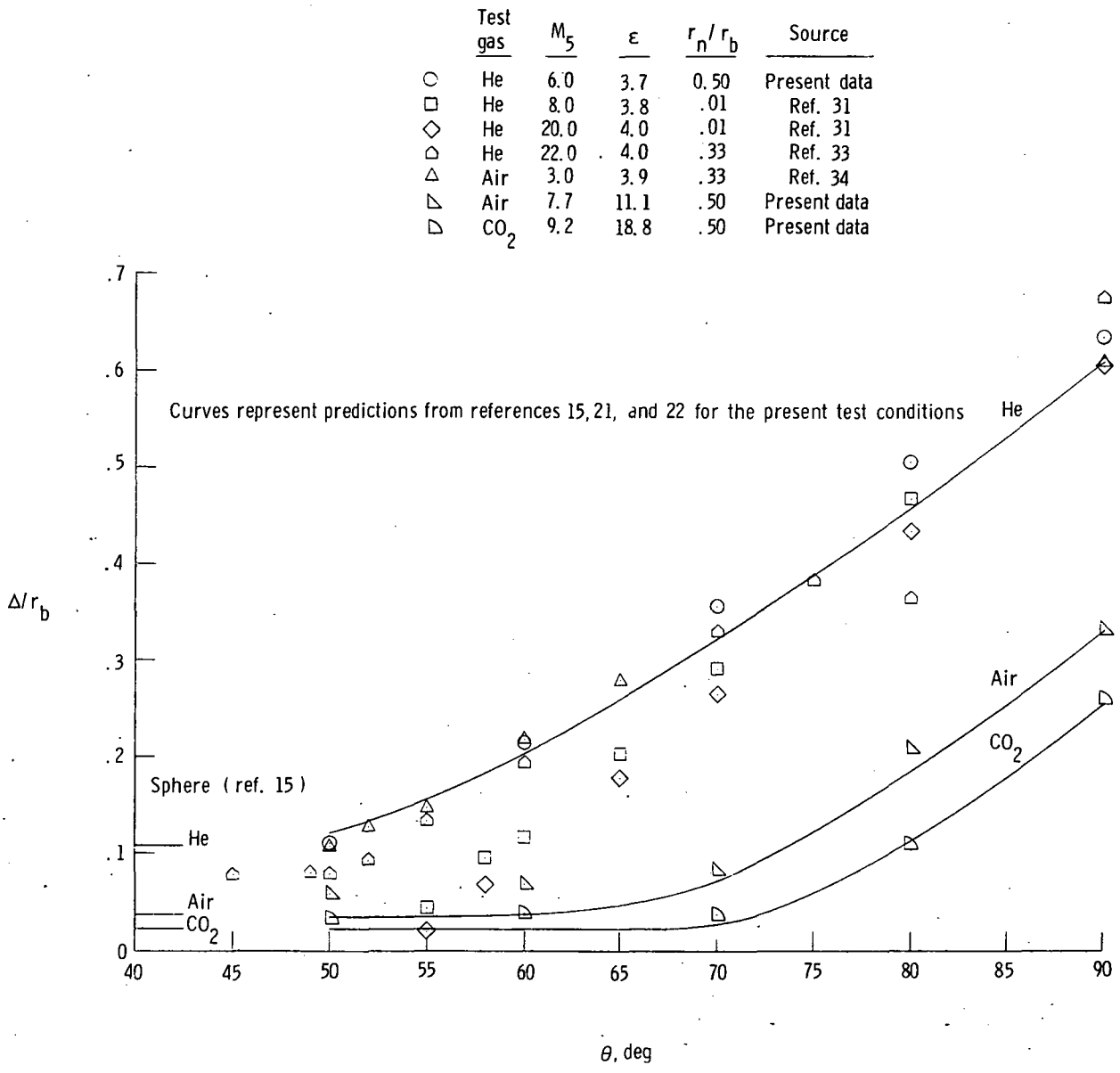


Figure 24.- Variation of shock standoff distance with cone semiapex angle.

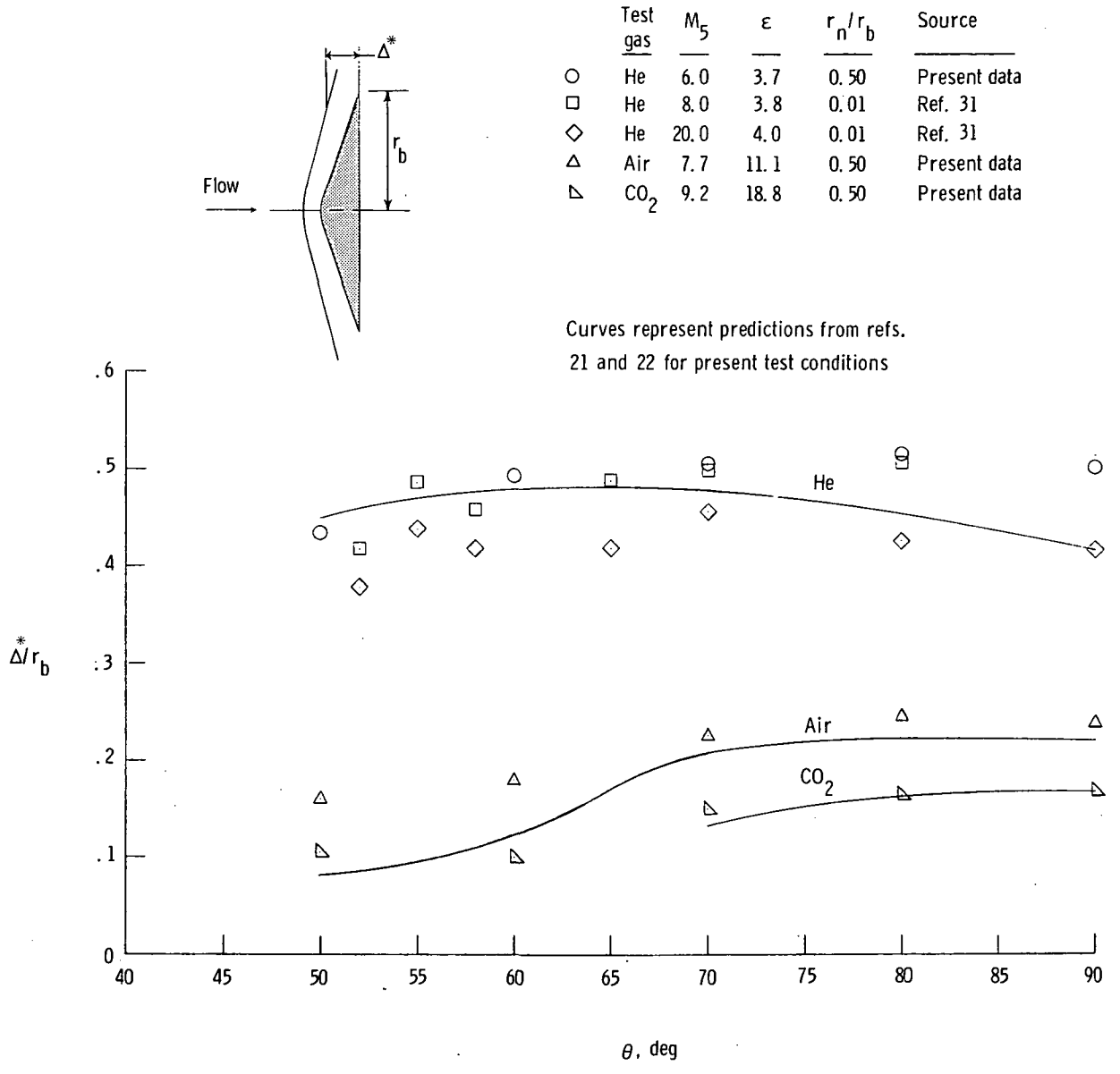


Figure 25.- Variation of shock standoff distance at model corner with cone semiapex angle.

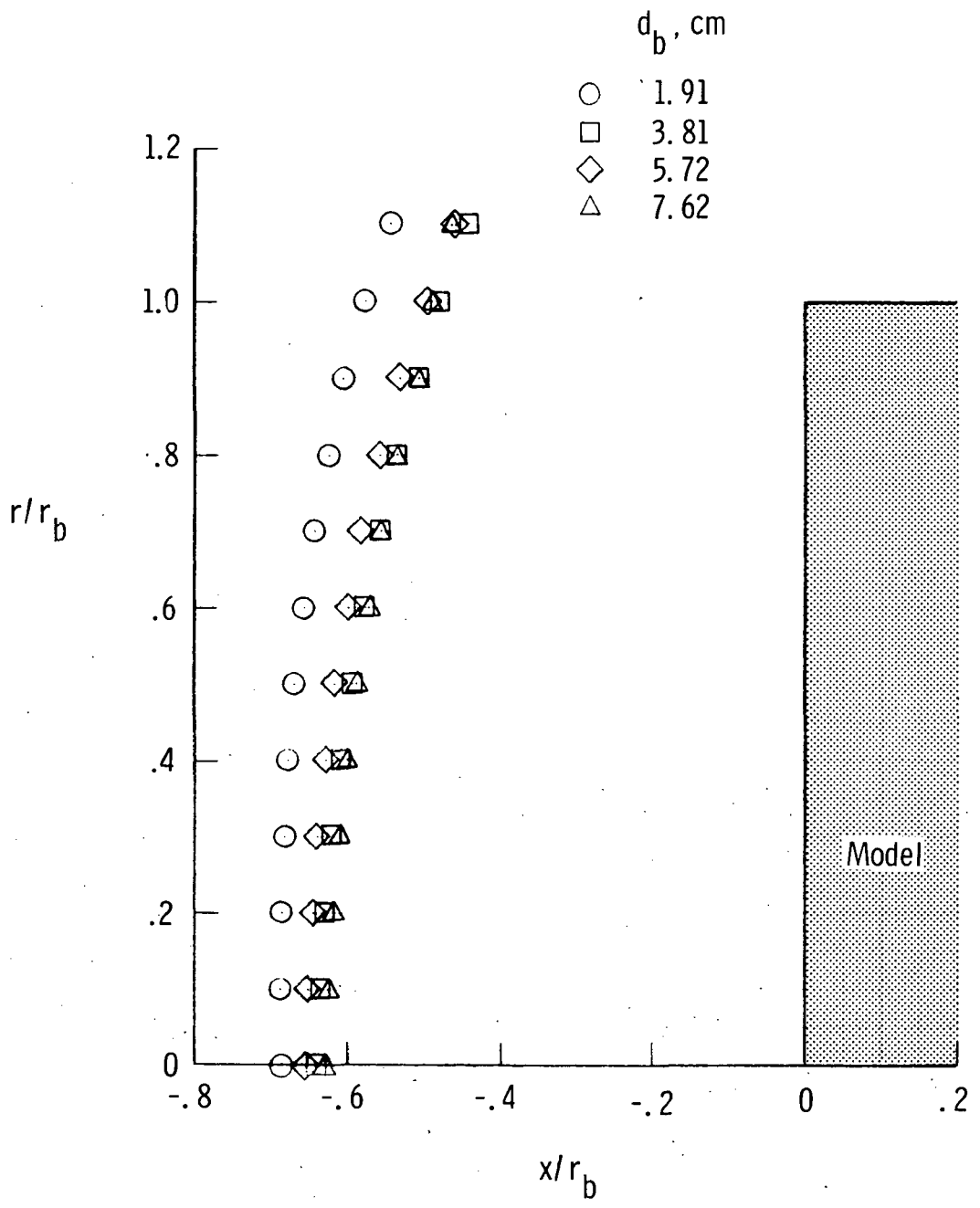


(a) Helium. $M_5 = 6.0$; $\epsilon = 3.7$.

Figure 26.- Measured shock shapes for flat-faced cylinder models of various diameters for helium, air, and $CO_2$ test gases.

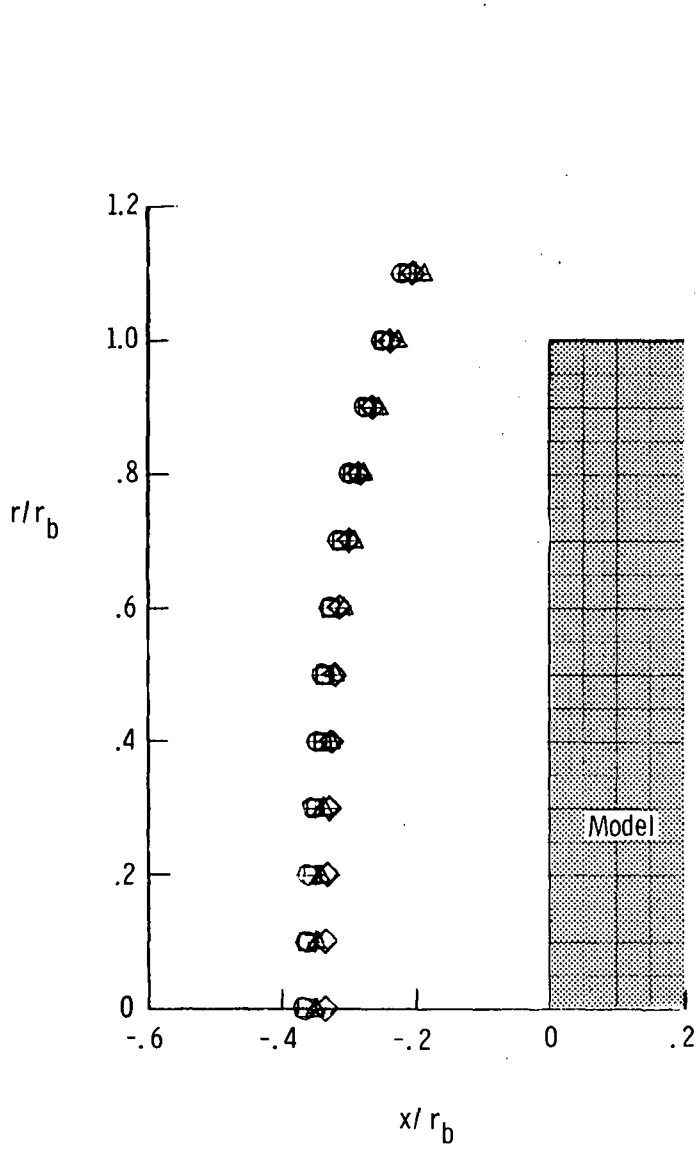


(b) Air. $M_5 = 7.7$; $\epsilon = 11.1$.

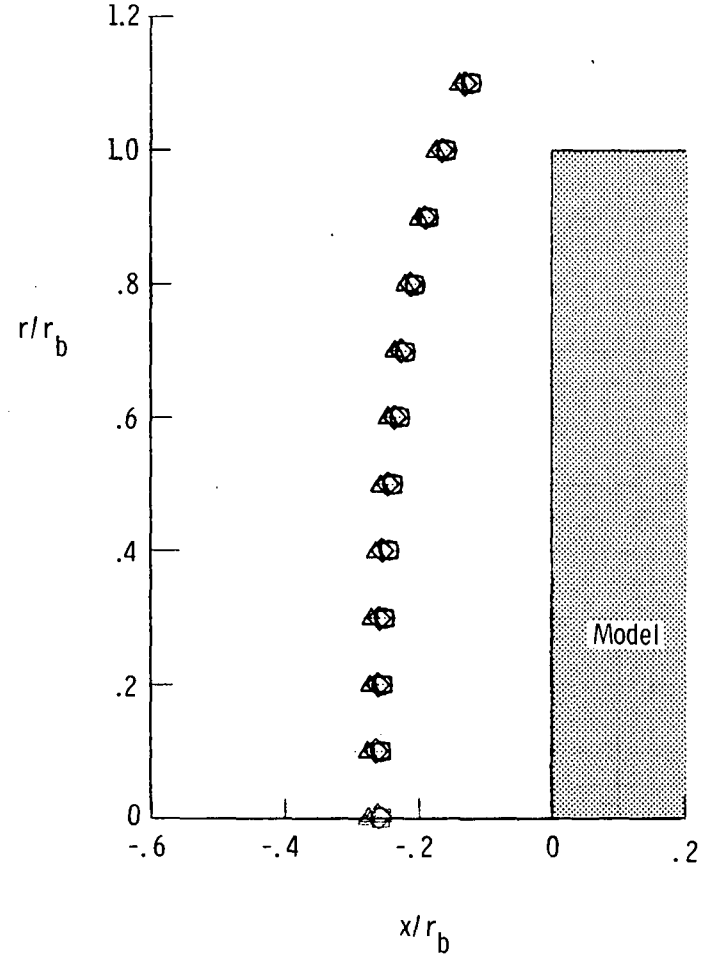


(c) $CO_2$. $M_5 = 9.2$; $\epsilon = 18.8$.

Figure 26.- Concluded.

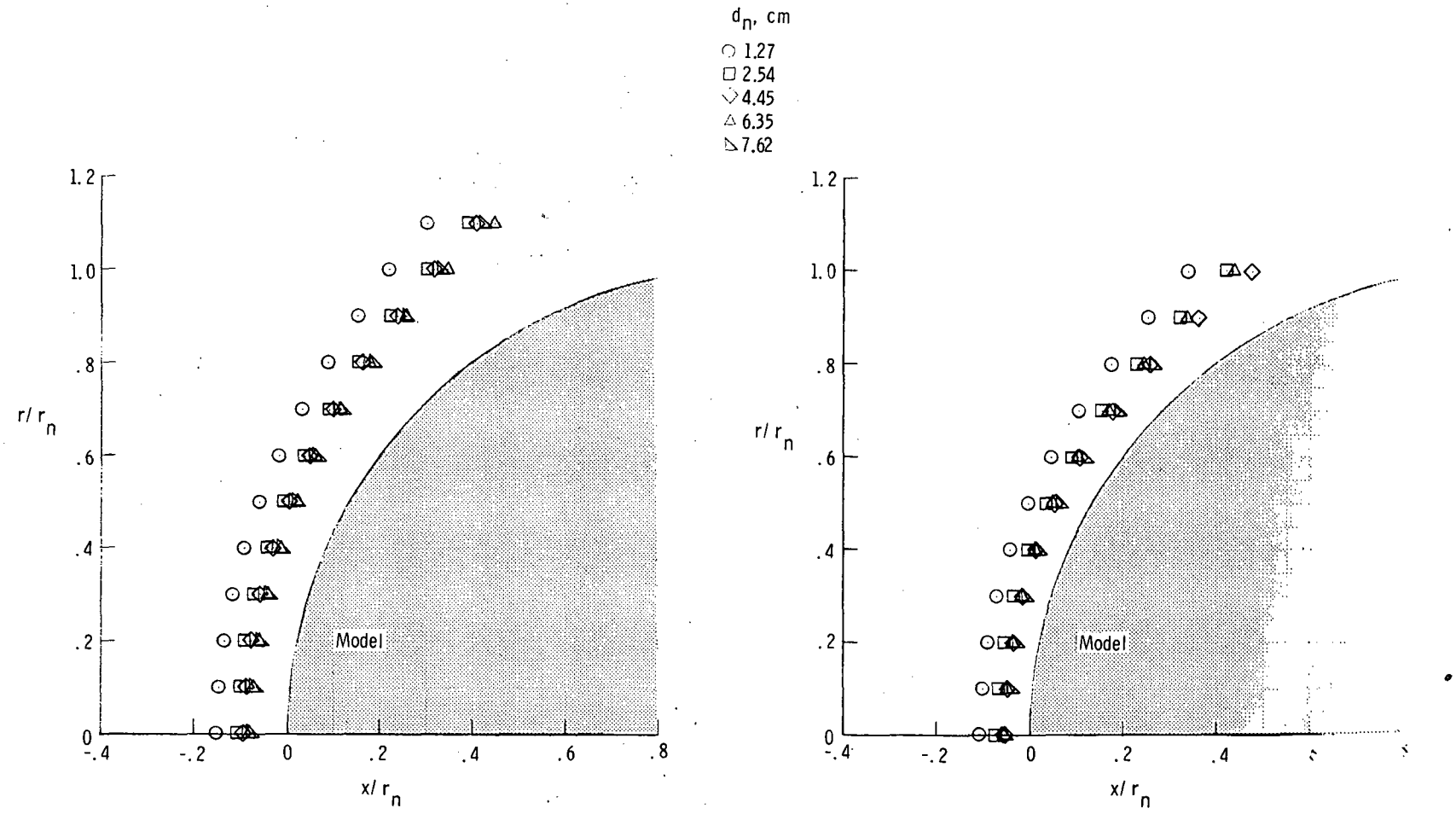


(a) Air. $M_5 = 7.7$; $\epsilon = 11.1$.

(b) $CO_2$. $M_5 = 9.2$; $\epsilon = 18.8$.

Figure 27.- Measured shock shapes for sphere models of various diameters for air and $CO_2$ test gases.

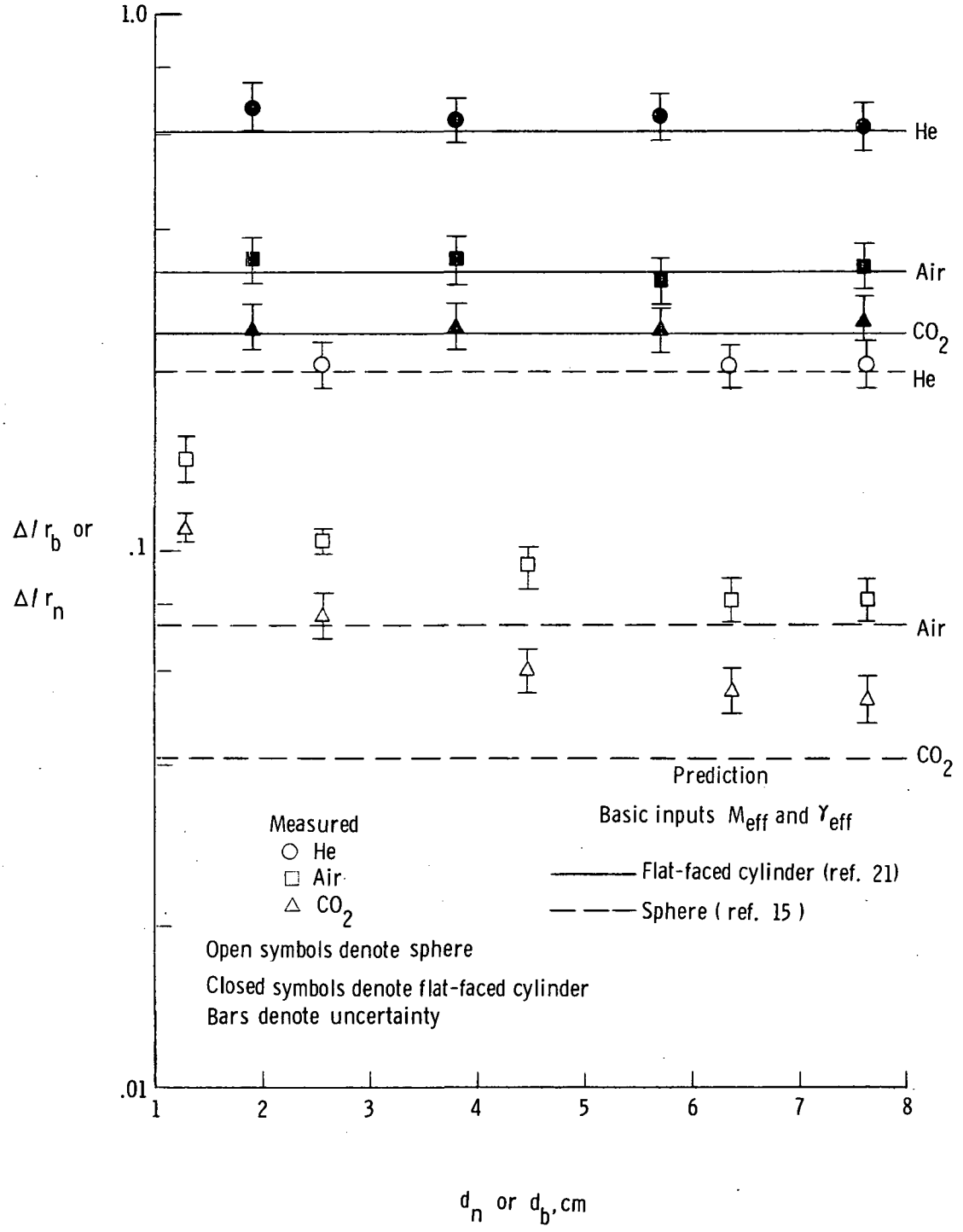


Figure 28.- Shock standoff distance for flat-faced cylinder and sphere as a function of model diameter.

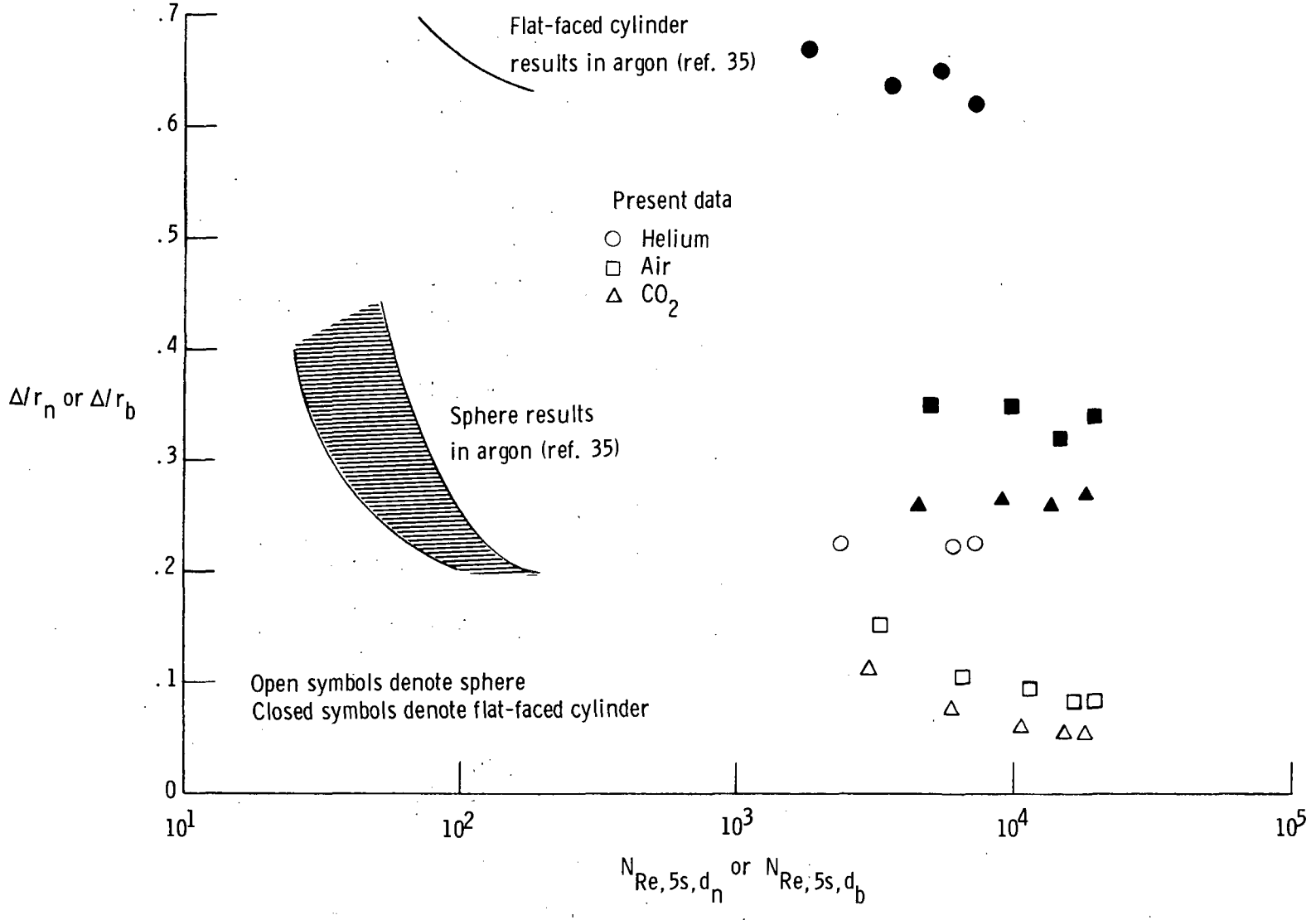


Figure 29.- Shock standoff distance for sphere and flat-faced cylinder as a function of Reynolds number based on postshock flow conditions.

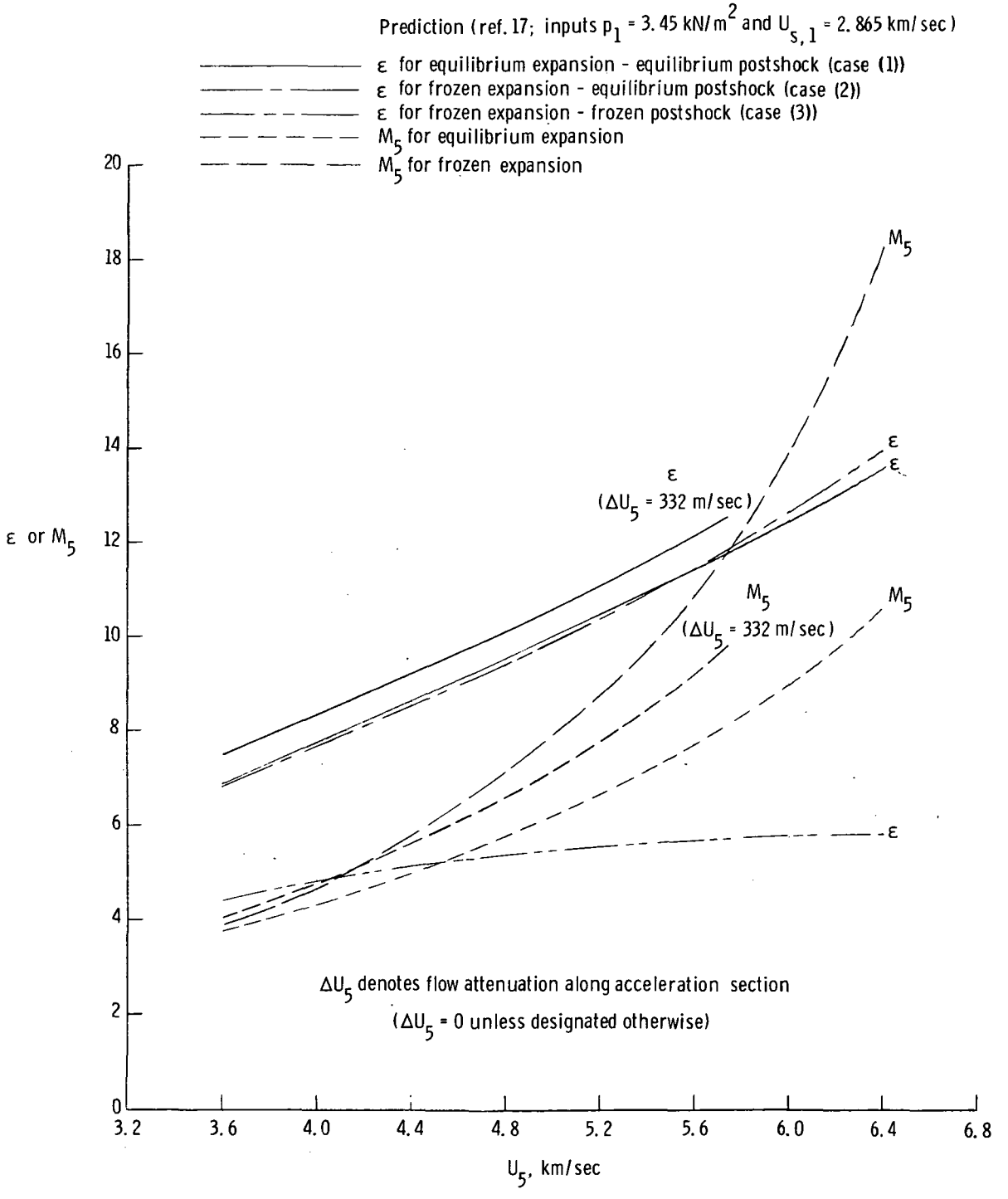


(a) No shock reflection at secondary diaphragm.

Figure 30.- Normal shock density ratio and free-stream Mach number as a function of free-stream velocity for air test gas.

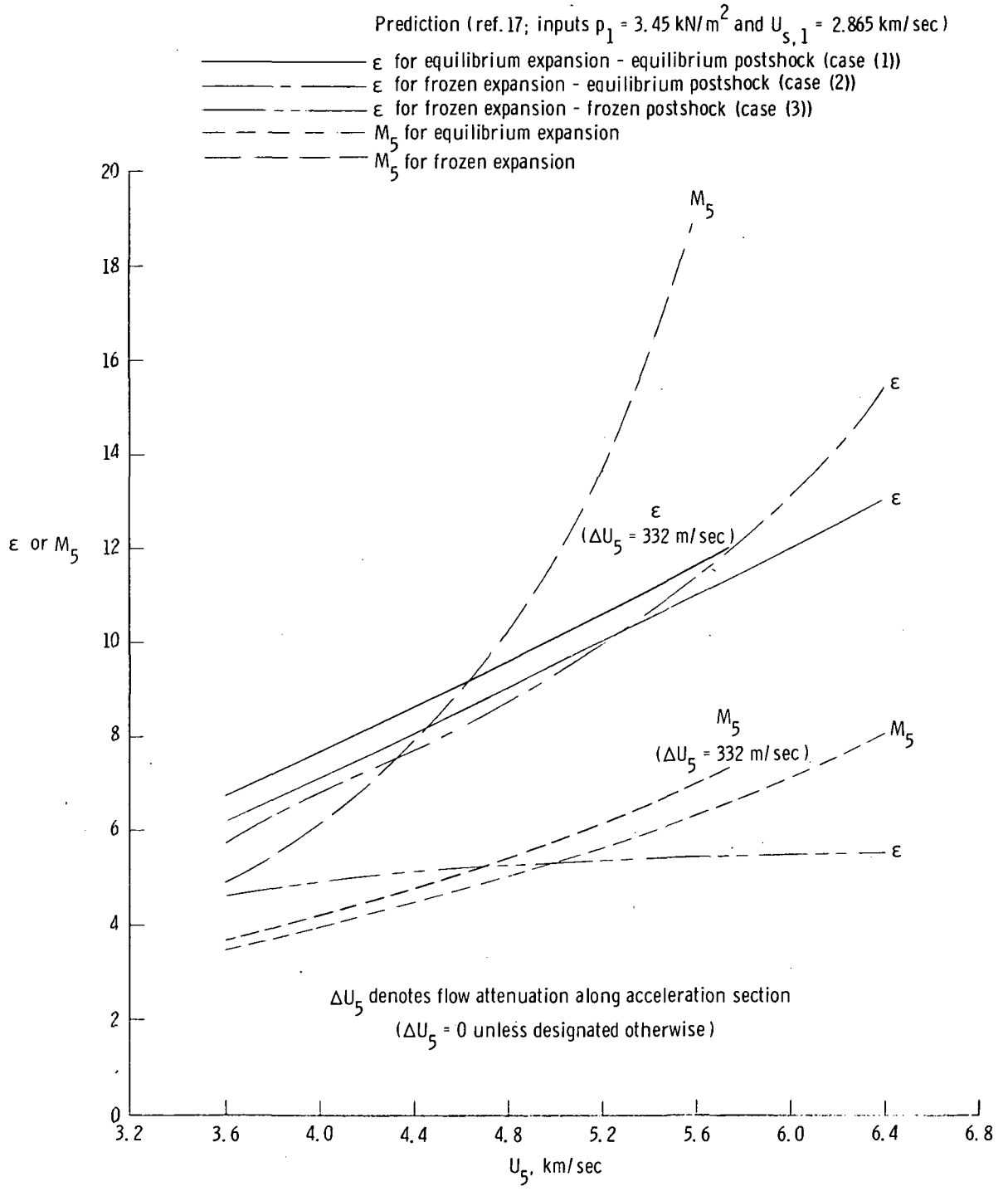


(b) Totally reflected shock at secondary diaphragm.

Figure 30.- Concluded.

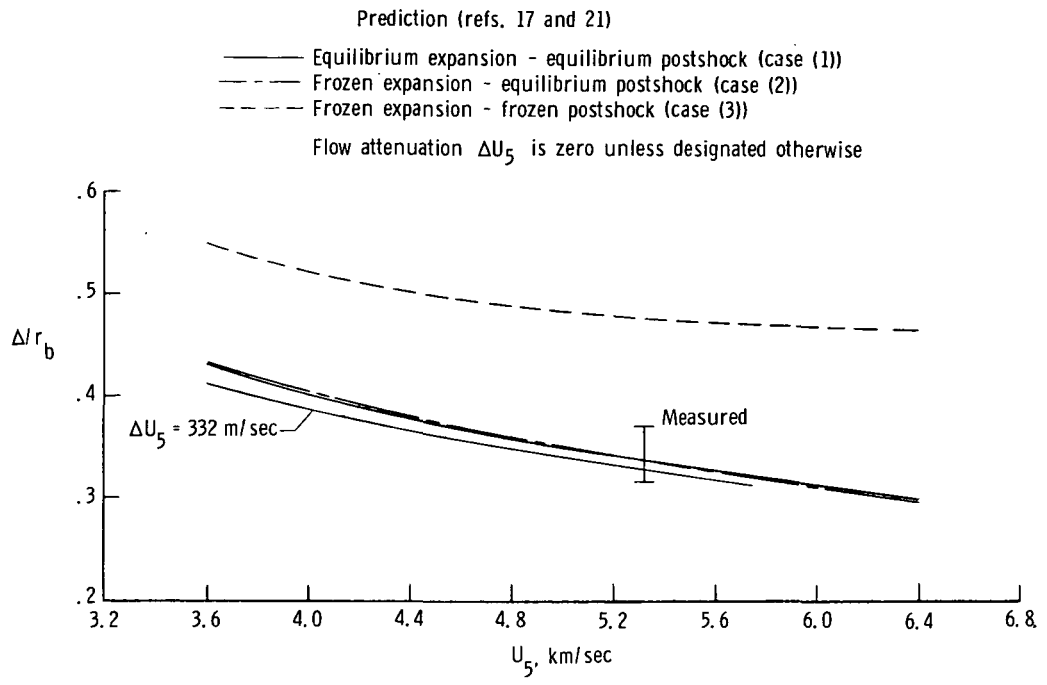


(a) No shock reflection at secondary diaphragm.

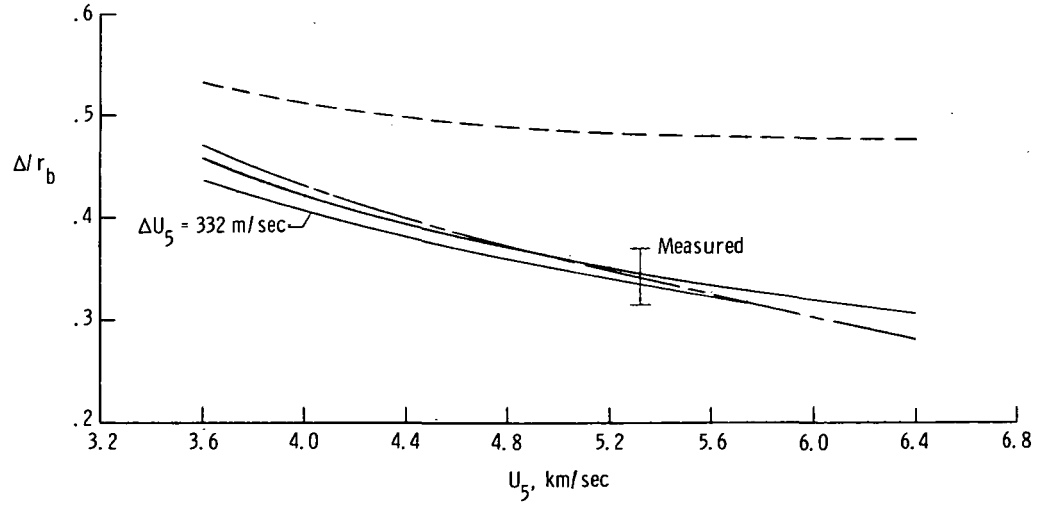


(b) Totally reflected shock at secondary diaphragm.

Figure 31.- Shock standoff distance for flat-faced cylinder as a function of free-stream velocity for air test gas.

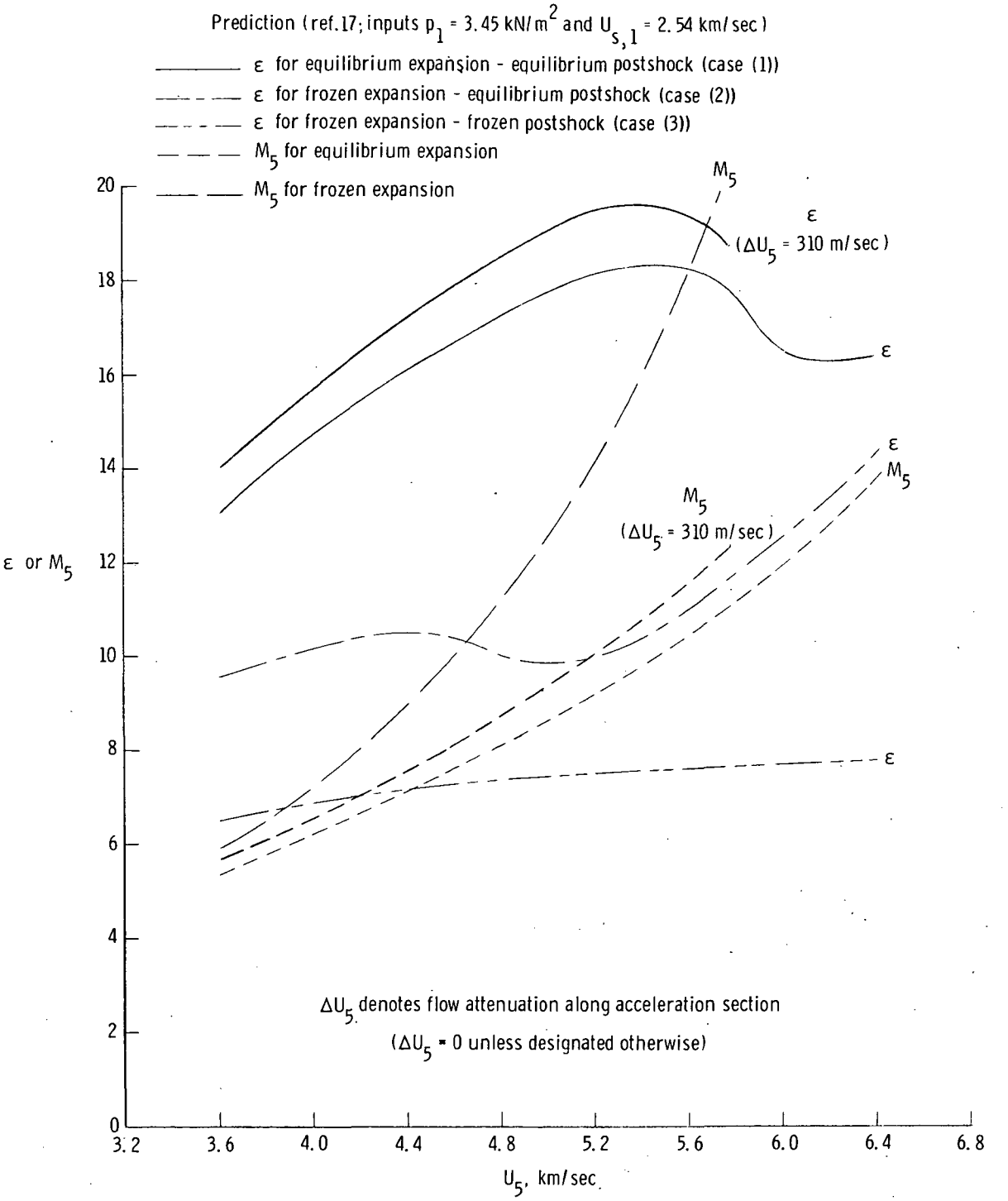


(a) No shock reflection at secondary diaphragm.

Figure 32.- Normal shock density ratio and free-stream Mach number as a function of free-stream velocity for $CO_2$ test gas.

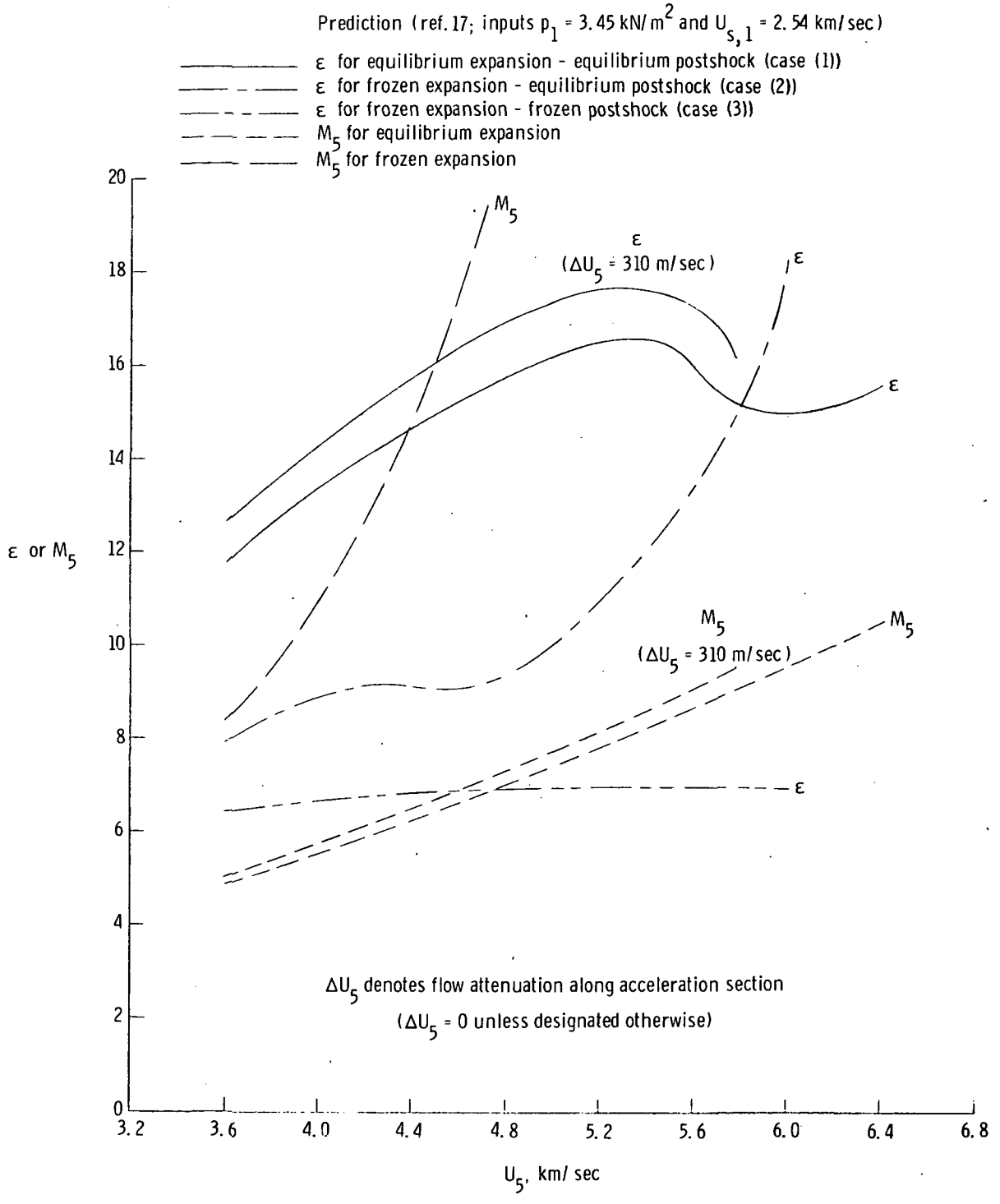


(b) Totally reflected shock at secondary diaphragm.

Figure 32.- Concluded.

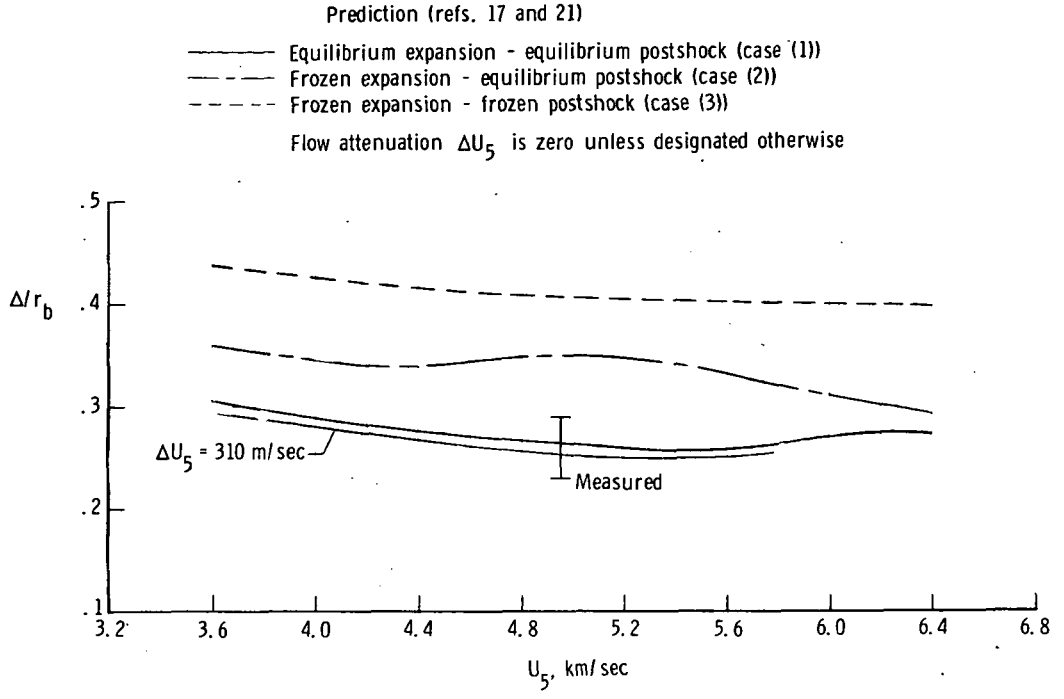


(a) No shock reflection at secondary diaphragm.

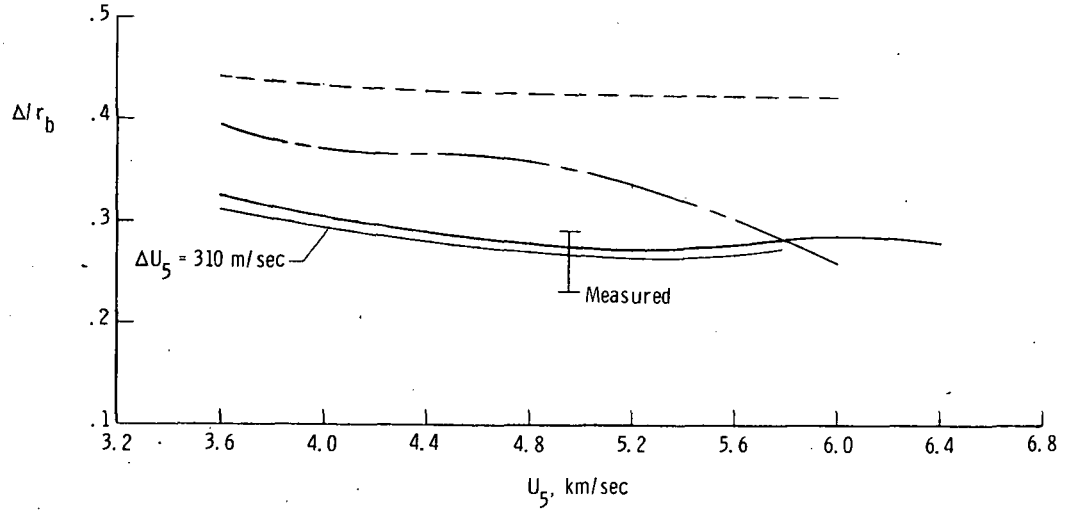


(b) Totally reflected shock at secondary diaphragm.

Figure 33.- Shock standoff distance for flat-faced cylinder as a function of free-stream velocity for $CO_2$ test gas.

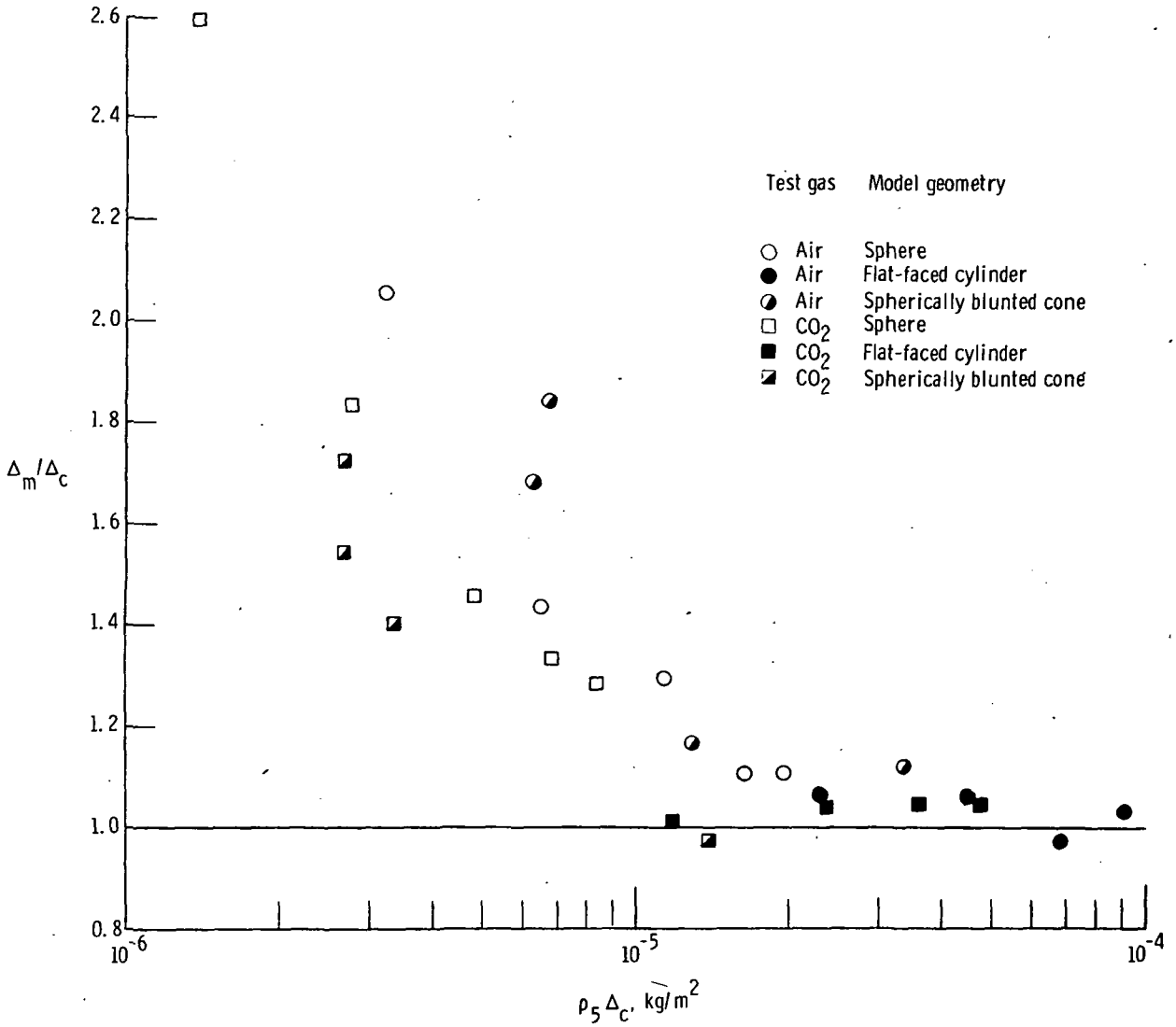


Figure 34.- Ratio of measured to predicted shock standoff distance as a function of scaling law parameter.

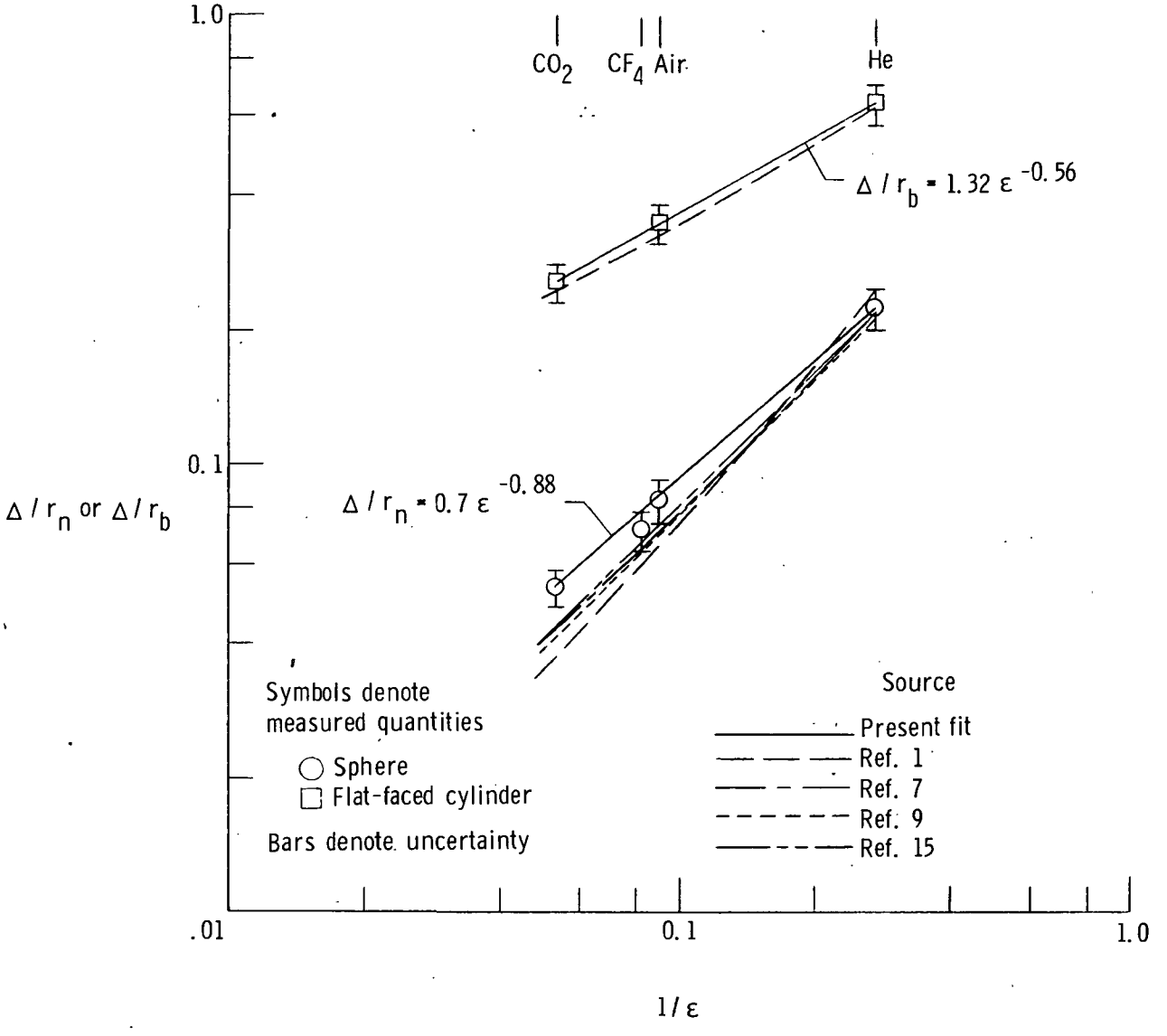


Figure 35.- Shock standoff distance as a function of inverse normal shock density ratio for flat-faced cylinder and sphere.



NASA-Langley, 1975 L-9775

*"The aeronautical and space activities of the United States shall be conducted so as to contribute . . . to the expansion of human knowledge of phenomena in the atmosphere and space. The Administration shall provide for the widest practicable and appropriate dissemination of information concerning its activities and the results thereof."*

—NATIONAL AERONAUTICS AND SPACE ACT OF 1958

# NASA SCIENTIFIC AND TECHNICAL PUBLICATIONS

TECHNICAL REPORTS: Scientific and technical information considered important, complete, and a lasting contribution to existing knowledge.

TECHNICAL NOTES: Information less broad in scope but nevertheless of importance as a contribution to existing knowledge.

TECHNICAL MEMORANDUMS: Information receiving limited distribution because of preliminary data, security classification, or other reasons. Also includes conference proceedings with either limited or unlimited distribution.

CONTRACTOR REPORTS: Scientific and technical information generated under a NASA contract or grant and considered an important contribution to existing knowledge.

TECHNICAL TRANSLATIONS: Information published in a foreign language considered to merit NASA distribution in English.

SPECIAL PUBLICATIONS: Information derived from or of value to NASA activities. Publications include final reports of major projects, monographs, data compilations, handbooks, sourcebooks, and special bibliographies.

TECHNOLOGY UTILIZATION PUBLICATIONS: Information on technology used by NASA that may be of particular interest in commercial and other non-aerospace applications. Publications include Tech Briefs, Technology Utilization Reports and Technology Surveys.

***Details on the availability of these publications may be obtained from:***

**SCIENTIFIC AND TECHNICAL INFORMATION OFFICE**

**NATIONAL AERONAUTICS AND SPACE ADMINISTRATION**

**Washington, D.C. 20546**